Doctoral Dissertation

Controlling Oxidation Reactivity of Osmium Complexes

Tomohiro Fujimoto

January 2022

Department of Material and Life Science
Division of Advanced Science and Biotechnology
Graduate School of Engineering
Osaka University

Contents

General Introduction

Selective oxidation of hydrocarbons to valuable organic compounds is a key process in synthetic and industrial chemistry. For hydrocarbon oxidation reactions, transition metal oxides (M_xO_y) such as $FeCrO_4$, Fe_2O_3, and MnO_2 had been used as an oxidant, since they are abundant in mineral and sea water.[1-10] For example, chromium oxide (CrO_3) is well known to oxidize alcohols to the corresponding aldehydes and carboxylic acids (Jones oxidation).[11, 12] Potassium permanganate ($KMnO_4$) is also used in oxidative cleavage of alkenes.[13]

Osmium tetroxide (OsO_4) adopts the highest oxidation number of +VIII having a monomeric tetrahedron structure, which has been frequently employed for *cis*-dihydroxylation and *cis*-aminohydroxylation of alkenes.[14-20] The reaction mechanism for alkene the *cis*-dihydroxylation has been investigated in detail with various approaches such as kinetic analysis and theoretical calculations to demonstrate that an OsO_4 adduct of alkene is involved as a key reaction intermediate. Then, the OsO_4 adduct intermediate is hydrolyzed to give diol products and $Os^{VI}O_2(OH)_2$, the latter of which is reoxidized by an oxidant [O] such as *N*-methylmorpholine *N*-oxide (NMO) to regenerate OsO_4, completing the catalytic cycle (Scheme 1).[21-23] On the other hand, the reaction mechanism for the *cis*-aminohydroxylation of alkene was not fully elucidated, because complicated mixture of osmium complexes are formed in the reaction of OsO_4 with nitrogen containing oxidants such as chloramine-T (TsNClNa) (Scheme 2).[24-26] In such a case, adoption of nitrogen chelating ligands will provide us an opportunity to control the structure and reactivity of osmium derived reactive intermediates to enhance reaction selectivity and to explore the detailed reaction mechanism.

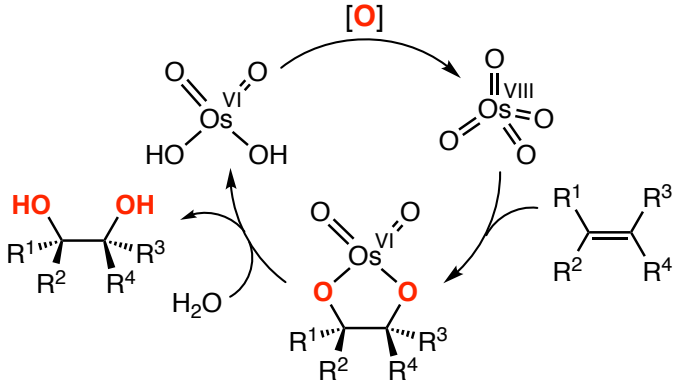

Scheme 1. Proposed reaction mechanism for *cis*-dihydroxylation of alkene by OsO_4.

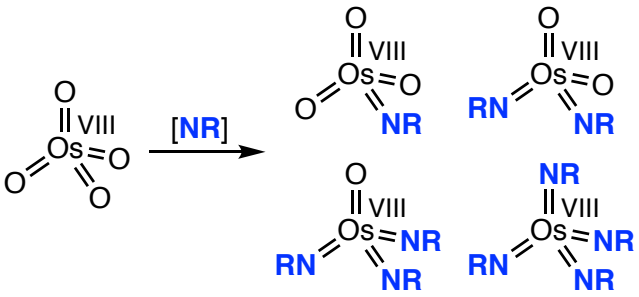

Scheme 2. Reaction of OsO_4 with nitrogen containing oxidants (R = Ts, ^{t}Bu, and Ad).

In recent years, OsO_4 has been reported to oxidize alkane with $NaIO_4$ as a re-oxidant under alkaline aqueous conditions, where coordination of hydroxide anion to the osmium center is proposed to enhance the oxidation reactivity.[27, 28] Such an enhancement of OsO_4 reactivity by the addition of a base has also been reported in the alkene *cis*-dihydroxylation.[29-33] However, the structure and reactivity of the hydroxide adduct of OsO_4 has not been explored yet. Furthermore, the overoxidation proceeded exclusively to yield the corresponding aldehyde, carboxylic acid, and CO_2 (Scheme 3). Thus, elucidation of factors controlling reactivity of OsO_4 and selectivity of the products is essential to develop efficient catalysts for the practical use of OsO_4 in direct hydroxylation of alkanes to alcohols. To this end, detail characterization of the anion adducts of OsO_4 and elucidation of the reaction mechanisms are essential.

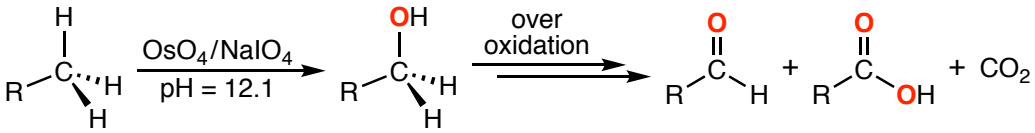

Scheme 3. Alkane oxidation with $NaIO_4$ catalyzed by OsO_4 under alkaline aqueous conditions.

In this study, the author conducted detailed reactivity and mechanistic studies on the oxidation reactions with osmium complexes to provide important information for the development of efficient catalytic oxidation systems based on osmium complexes.

This thesis entitled "Controlling Oxidation Reactivity of Osmium Complexes" consists of four chapters.

In Chapter 1, osmium(III) complexes coordinated by a cyclohexanediamine-based N4-tetradentate ligand (*trans*-*N*,*N*'-dimethyl-*N*,*N*'-bis(2-pyridylmethyl)-1,2-cyclohexanediamine: BPMCN) are synthesized. The $[Os^{III}(OH)(H_2O)(BPMCN)]^{2+}$ complex catalyzes *cis*-dihydroxylation and *cis*-aminohydroxylation of styrene to yield the corresponding diol and aminoalcohol products, respectively. The oxido-hydroxido-osmium(V) complex $[Os^{V}(O)(OH)(BPMCN)]^{2+}$ as the active oxidants for the *cis*-dihydroxylation is isolated by the reaction of the osmium(III) complex with H_2O_2 (Scheme 4). The oxidation of the osmium(III) with chloramine-T (TsNClNa) yields oxido-aminato-osmium(V) complex, $[Os^{V}(O)(NHTs)(BPMCN)]^{2+}$ (Scheme 4). The X-ray crystallographic analysis indicates that the –NHTs group works as a monoanionic aminate group and the Os^{V}–NHTs bond has a single bond character. The synthesized oxido-aminato-osmium(V) complex is also revealed as the active oxidant for the *cis*-aminohydroxylation by the direct reaction of the complex with styrene.

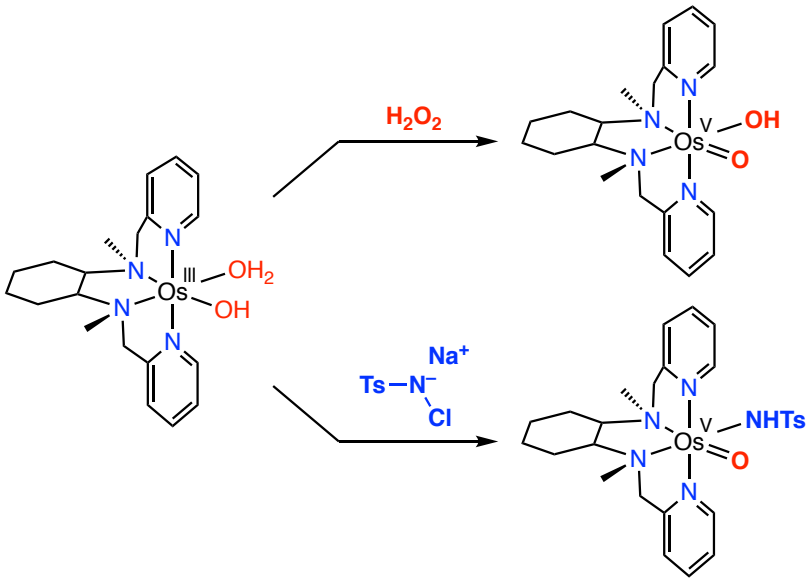

Scheme 4. Generation of osmium(V) complexes from osmium(III) complex.

In Chapter 2, interaction of OsO_4 with a series of halide ions ($X^- = I^-$, Br^-, Cl^-, and F^-) is examined. Stable 1 : 1 adducts, $[OsO_4(X)]^-$ (**1**^{X}), are formed in the case of Br^-, Cl^-, and F^-, whereas redox reaction takes place with I^- to give $[Os^{VII}O_4]^-$ and I•. The X-ray crystallographic analyses of the halide adducts indicate that the structural distortion of the osmium center from tetrahedron to trigonal bipyramid is observed as the halide ion

goes from Br^-, Cl^-, and to F^-. Among the adducts, $\mathbf{1}^{\mathbf{F}}$ shows much higher reactivity compared to OsO_4 itself in the oxidation of benzyl alcohol to benzaldehyde, even though $\mathbf{1}^{\mathbf{F}}$ has a lower reduction potential compared to OsO_4. Mechanistic details of the alcohol oxidation reaction are evaluated by kinetic studies including Hammett analysis and kinetic deuterium isotope effects as well as by DFT calculations (Scheme 5).

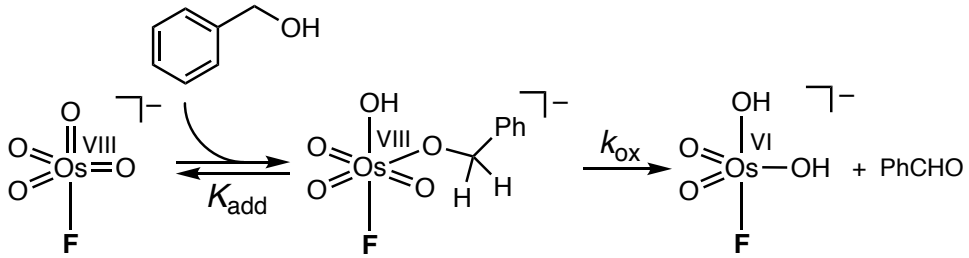

Scheme 5. Oxidation of benzyl alcohol by osmium fluoride adduct ($\mathbf{1}^{\mathbf{F}}$, $[OsO_4(F)]^-$).

In Chapter 3, carboxylate-adducts of OsO_4 ($\mathbf{1}^{\mathbf{X}}$, $[OsO_4(X)]^-$) are synthesized by the reaction of OsO_4 with carboxylate anions (X = OAc: acetate and OBz: benzoate), the structures of which are determined by X-ray crystallographic analysis. The adduct complexes $\mathbf{1}^{\mathbf{X}}$ are found to show higher reactivity in the benzylic $C(sp^3)$–H bond oxidation compared to OsO_4 itself. On the basis of kinetic investigation together with the DFT calculation, the author proposes a *stepwise* mechanism, where oxido group at the axial position of the carboxylate-adducts of OsO_4 works as a hydrogen atom accepter and the oxido group at the equatorial position acts as an oxygen atom donor (Figure 1).

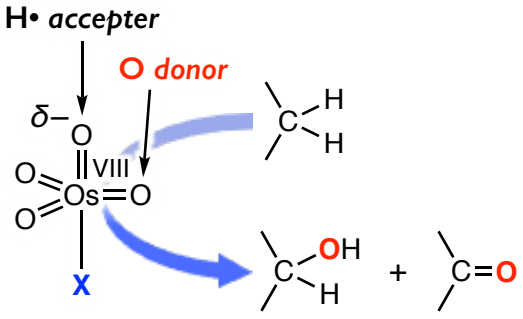

Figure 1. $C(sp^3)$–H bond oxidation by carboxylate-adduct of OsO_4 ($[OsO_4(X)]^-$, X = OAc and OBz).

Finally, in Chapter 4, oxidation of cyclohexane with hydrogen peroxide (H_2O_2) catalyzed by OsO_4 is examined (Scheme 6). Cyclohexane is oxidized to cyclohexyl

hydroperoxide (**P**) selectively, which is converted to cyclohexanol (**A**) by the treatment with triphenylphosphine (PPh_3). The catalytic activity of OsO_4 is also enhanced by the addition of carboxylate anion. Encouraged by this result, the author develops an OsO_4-immobilized mesoporous silica (SBA-15) containing carboxylate groups on the surface.

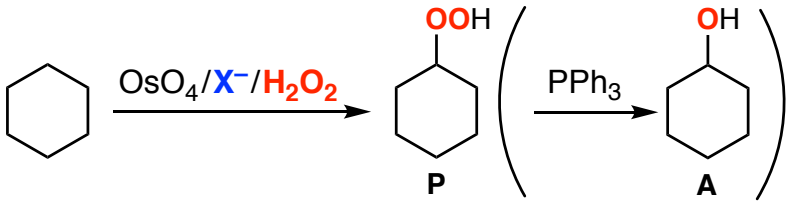

Scheme 6. Oxidation of cyclohexane with H_2O_2 catalyzed by carboxylate adduct of OsO_4 (X = OBz).

References

1. F. H. Westheimer, A. Novick, *J. Chem. Phys*. **1943**, *11*, 506-512.
2. K. Bowden, I. M. Heilbron, E. R. H. Jones, B. C. L. Weedon, *J. Chem. Soc*. **1946**, 39-45.
3. G. I. Poos, G. E. Arth, R. E. Beyler, L. H. Sarett, *J. Am. Chem. Soc*. **1953**, *75*, 422-429.
4. K. B. Wiberg, K. A. Saegebarth, *J. Am. Chem. Soc*. **1957**, *79*, 2822-2824.
5. E. Klein, W. Rojahn, *Tetrahedron* **1965**, *21*, 2353-2358.
6. J. C. Collins, W. W. Hess, F. J. Frank, *Tetrahedron Lett*. **1968**, *9*, 3363-3366.
7. D. M. Walba, M. D. Wand, M. C. Wilkes, *J. Am. Chem. Soc*. **1979**, *101*, 4396-4397.
8. V. Duma, D. Hönicke, *J. Catal*. **2000**, *191*, 93-104.
9. F. Shi, M. K. Tse, M.-M. Pohl, A. Brückner, S. Zhang, M. Beller, *Angew. Chem., Int. Ed*. **2007**, *46*, 8866-8868.
10. V. Polshettiwar, R. S. Varma, *Org. Biomol. Chem*. **2009**, *7*, 37-40.
11. B. Anders, W. Karl-Axel, *Acta Chem. Scand*. **1950**, 1131-1141.
12. J. S. Stephens, D. W. J. Cruickshank, *Acta Cryst. B* **1970**, *26*, 222-226.
13. R. U. Lemieuxan, D. V. Rudloff, *Can. J. Chem*. **1955**, *33*, 1701-1809.
14. N. A. Milas, S. Sussman, *J. Am. Chem. Soc*. **1936**, *58*, 1302-1304.

15. K. B. Sharpless, D. W. Patrick, L. K. Truesdale, S. A. Biller, *J. Am. Chem. Soc.* **1975**, *97*, 2305-2307.
16. K. B. Sharpless, A. O. Chong, K. Oshima, *J. Org. Chem.* **1976**, *41*, 177-179.
17. K. Akashi, R. E. Palermo, K. B. Sharpless, *J. Org. Chem.* **1978**, *43*, 2063-2066.
18. E. Herranz, S. A. Biller, K. B. Sharpless, *J. Am. Chem. Soc.* **1978**, *100*, 3596-3598.
19. R. Ray, D. S. Matteson, *Tetrahedron Lett.* **1980**, *21*, 449-450.
20. S. G. Hentges, K. B. Sharpless, *J. Org. Chem.* **1980**, *45*, 2257-2259.
21. K. B. Sharpless, K. Akashi, *J. Am. Chem. Soc.* **1976**, *98*, 1986-1987.
22. V. VanRheenen, R. C. Kelly, D. Y. Cha, *Tetrahedron Lett.* **1976**, *17*, 1973-1976.
23. B. B. Lohray, V. Bhushan, R. K. Kumar, *J. Org. Chem.* **1994**, *59*, 1375-1380.
24. A. O. Chong, K. Oshima, K. B. Sharpless, *J. Am. Chem. Soc.* **1977**, *99*, 3420-3426.
25. K. Muñiz, *Chem. Soc. Rev.* **2004**, *33*, 166-174.
26. S. Devari, R. Deshidi, M. Kumar, A. Kumar, S. Sharma, M. Rizvi, M. Kushwaha, A. P. Gupta, B. A. Shah, *Tetrahedron Lett.* **2013**, *54*, 6407- 6410.
27. B. C. Bales, P. Brown, A. Dehestani, J. M. Mayer, *J. Am. Chem. Soc.* **2005**, *127*, 2832-2833.
28. T. Osako, E. J. Watson, A. Dehestani, B. C. Bales, J. M. Mayer, *Angew. Chem., Int. Ed.* **2006**, *45*, 7433-7436.
29. M. J. Cleare, P. C. Hydes, W. P. Griffith, M. J. Wright, *J. Chem. Soc., Dalton Trans.* **1977**, 941-944.
30. K. B. Sharpless, A. Y. Teranishi, J. E. Backvall, *J. Am. Chem. Soc.* **1977**, *99*, 3120-3128.
31. S. G. Hentges, K. B. Sharpless, *J. Am. Chem. Soc.* **1980**, *102*, 4263-4265.
32. E. N. Jacobsen, I. Marko, M. B. France, J. S. Svendsen, K. B. Sharpless, *J. Am. Chem. Soc.* **1989**, *111*, 737-739.
33. H. C. Kolb, P. G. Andersson, Y. L. Bennani, G. A. Crispino, K. S. Jeong, H. L. Kwong, K. B. Sharpless, *J. Am. Chem. Soc.* **1993**, *115*, 12226-12227.

Chapter 1

Isolation and Characterization of Active Oxidants for Dihydroxylation and Aminohydroxylation of Alkenes Catalyzed by Osmium Complexes with a Linear N4-Tetradentate Ligand

Introduction

High valent metal-oxido (M=O) species have been proposed as key reactive intermediates in the oxidation reactions of various substrates not only in synthetic organic chemistry but also in metalloenzyme systems.[1-10] Oxidation of organic substrates includes hydroxylation, dehydrogenation, epoxidation, and electron transfer.[1-5] M=O species also induce the oxidation reactions of inorganic substrates such as water (H_2O) to dioxygen (O_2) and sulfite (SO_3^{2-}) to sulfate (SO_4^{2-}) in the enzymatic systems.[6-10] Extensive studies have been done to characterize such M=O species by several spectroscopic methods and crystal structure analyses. On the other hand, M=O species can catalyze *cis*-selective dihydroxylation of alkenes or arenes, halogenation of a C–H bond, and *cis*-selective aminohydroxylation of alkenes, when the metal centers have an additional oxide, hydroxide, or halide ligand X (Scheme 1-1).

Osmium tetroxide and its monodentate ligand adducts (Scheme 1-1(a), X = O, $Os^{VIII}O_4$) are the first examples of such species, which induce *cis*-dihydroxylation of alkenes.[11-14] An oxido-hydroxido-iron(V) species [Fe^{V}(O)OH] is found as the second

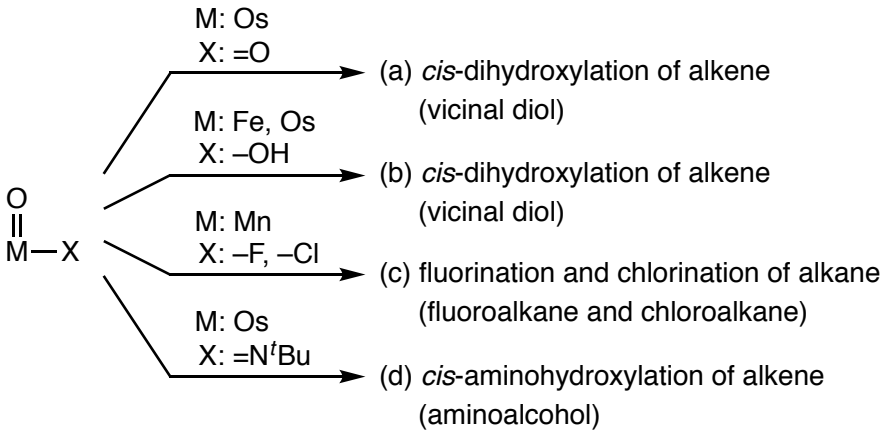

Scheme 1-1. Schematic classification of oxidation reactions by ligand-bound metal-oxido species [M(O)X].

example in the reaction center of Rieske dioxygenase that catalyzes arene dihydroxylation (Scheme 1-1(b); M = Fe^{V}). Several model complexes of the enzymatic reaction center have been prepared and their reactivity has been explored in detail. However, crystallographic characterization of Fe^{V}(O)OH species has yet to be performed. On the other hand, our group has developed oxido-hydroxido-osmium(V) complexes supported by a tripodal tetradentate ligand tris(2-pyridylmethyl)amine (TPA) and a macrocyclic tetradentate ligand *N*,*N*'-dimethyl-2,11-diaza-[3.3](2,6)pyridinophane (L-N_4Me_2) as new members of M(O)OH species (Scheme 1-1(b), M = Os^{V}), which catalyze very efficient *cis*-selective dihydroxylation of alkenes using H_2O_2 as the terminal oxidant.[15, 16] In the *cis*-dihydroxylation, the osmium complex catalysts employ an Os^{V}/Os^{III} redox cycle, where the oxido-hydroxido-osmium(V) active species is regenerated by the reaction of the reduced hydroxido-aquo-osmium(III) complex with H_2O_2. Furthermore, our group has succeeded to determine the crystal structures of the oxido-hydroxido-osmium(V) complexes of TPA and L-N_4Me_2.[15, 16] The third examples are halide bound Mn=O complexes [Mn(O)X] that can catalyze C–H fluorination and C–H chlorination (Scheme 1-1(c)).

The forth examples of M=O(X) species are oxido-imido-osmium(VIII) compounds, OsO_3(NR), that can insert its oxygen and nitrogen groups into C=C double bond of alkenes in a *syn* manner to yield 1,2-aminoalcohols (Scheme 1-1(d)).[17, 18] No such unit has been found in other metal complexes beside osmium. However, no crystal structure was reported for the catalytically active species in such 1,2-aminohydroxylation of alkenes probably due to substitution labile nature of the Os=NR bond toward hydrolysis, going back to more stable OsO_4. To prohibit such hydrolytic degradation, $Os^{VIII}O_3(N^{t}Bu)$ having sterically demanding *tert*-butyl group was synthesized from OsO_4 and $^{t}BuNH_2$ and its crystal structure was determined.[19] However, the complex was catalytically inactive in the aminohydroxylation reaction.

Recently, our group found that the hydroxido-aquo-osmium(III) complex with L-N_4Me_2 can be a pre-catalyst for the *cis*-selective aminohydroxylation of alkenes with chloramine-T (TsNClNa) as an oxidant and a nitrogen donor (Scheme 1-2).[20] However, detailed characterization of the active species has yet to be accomplished. Here, the author finds that a cyclohexanediamine-based tetradentate ligand, *trans*-*N*,*N*'-dimethyl-*N*,*N*'-bis(2-pyridylmethyl)-1,2-cyclohexanediamine (BPMCN), can stabilize a variety

type of osmium complexes including $Os^{V}(O)(OH)$ complex. The author has also succeeded to determine the first crystal structure of oxido-aminato-osmium(V) complex as an active oxidant for alkene aminohydroxylation, which is a new member of M=O(X) species.

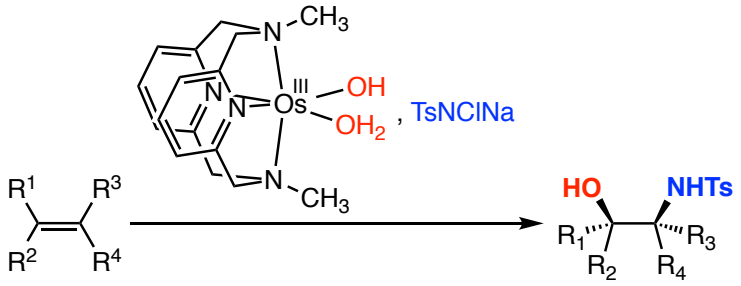

Scheme 1-2. *cis*-Aminohydroxylation of alkene with chloramine-T (TsNClNa) in the presence of an osmium(III) complex with L-N_4Me_2.

Experimental Section

General. The reagents and solvents used in this study except for the ligand and the osmium complexes were commercially available products. ^{1}H NMR spectra were recorded at 400 MHz on a JEOL-ECP400 or a JEOL-ECS400. FT-IR spectra were recorded with a Jasco FT/IR-4100. Elemental analysis was carried out with a Yanaco CHN-Corder MT-5. ESI-MS (electrospray ionization mass spectra) measurements were performed on a BRUKER cryospray microTOFII. The diol and aminoalcohol products were characterized by a HPLC system of a Shimadzu LC-10AD series and an EXTREMA series (JASCO Co.) equipped with a reverse phase column (Nacalai tesque, COSMOCIL, 5C18-AR-II). The ligand BPMCN and $(NH_4)_2[Os^{IV}Cl_6]$ were prepared according to the reported procedures.[21, 22]

Synthesis of *cis*-*α*-[$Os^{III}Cl_2$(BPMCN)](PF_6) (1). $(NH_4)_2[Os^{IV}Cl_6]$ (100.0 mg, 230 μmol) and BPMCN (70 mg, 230 μmol) were added to 5 mL of ethylene glycol. The suspension was heated at 145 °C for 15 min, during which the suspension changed to a dark brown solution. Ammonium hexafluorophosphate (75.0 mg, 460 μmol) in 0.5 mL of water was added to the solution to yield brown precipitate, which was isolated by filtration. The obtained brown solid was dissolved in 10 mL of acetone and was purified on alumina column (Alumina, Activated about 75 μL: Wako) with acetone as an eluent. The yellow band was collected and evaporated to give an orange oil, which was dissolved

in a mixed solvent of water and acetone (1 : 2). By slow evaporation of the acetone over a few days, red crystals were obtained. Yield: 30.0 mg (18%). Anal. Calcd. for **1** ($C_{20}H_{28}F_6N_4Cl_2OsP$): C, 32.88; H, 3.86; N. 7.67%. Found: C, 33.03; H, 4.06; N, 7.72%. ESI-MS: m/z = 586.13 ($[M]^+$). UV-vis (acetonitrile): λ_{max} = 248 nm (ε = 8600 M^{-1} cm^{-1}), 318 (7030). CV (acetonitrile): $E_{1/2}$ = –0.94 V vs. Fc/Fc^+ (100 mV/s).

Synthesis of *cis*-*β*-[$Os^{III}Cl_2$(BPMCN)](PF_6) (2). $(NH_4)_2[Os^{IV}Cl_6]$ (100.0 mg, 230 μmol) and BPMCN (70.0 mg, 230 μmol) were added to 5 mL of ethylene glycol. The suspension was heated at 198 °C for 3 min, during which the suspension changed to a dark brown solution. Ammonium hexafluorophosphate (75.0 mg, 460 μmol) in 0.5 mL of water was added to the solution to give brown precipitates, which was collected by filtration and dissolved in 10 mL of acetone. The compound was purified on an alumina column (Alumina, Activated about 75 μL: Wako) with acetone as an eluent. The yellow band was collected and evaporated to give an orange oil. The oily material was dissolved in a mixed solvent comprising water and acetone (1 : 2). By slow evaporation of acetone over a few days, red crystals precipitated out of the solution. Yield: 18.7 mg (11%). Anal. Calcd. for **2** ($C_{20}H_{28}F_6N_4Cl_2OsP$): C, 32.88; H, 3.86; N. 7.67%. Found: C, 32.96; H, 3.86; N, 7.69%. ESI-MS: m/z = 586.11 ($[M]^+$). UV-vis (acetonitrile): λ_{max} = 247 nm (ε = 10000 M^{-1} cm^{-1}), 320 (7590). CV (acetonitrile): $E_{1/2}$ = –0.91 V vs. Fc/Fc^+ (100 mV/s).

Synthesis of *cis*-*α*-[$Os^{III}(OTf)_2$(BPMCN)](OTf) (3). Complex **1** (30 mg, 70 μmol) in TfOH (0.5 mL) was heated at 115 °C under N_2 for 5 h. The flask was cooled to room temperature and further cooled to ca. 5 °C in an ice bath. Diethyl ether (20 mL) was added dropwise to the stirred solution cautiously to yield an orange microcrystalline powder, which was collected by filtration, washed with diethyl ether, and dried in vacuo. The single crystals were obtained by recrystallization from acetone/diethyl ether. Yield: 10.1 mg (15%). Anal. Calcd. for **3**·0.5$(CH_3)_2CO$ ($C_{24.5}H_{31}F_9N_4O_{9.5}OsS_3$): C, 29.70; H, 3.15; N. 5.65%. Found: C, 29.67; H, 3.37; N, 5.54%. FT-IR (KBr): 1348 and 1160-1270 cm^{-1} ($\nu_{(S=O)}$). ESI-MS: m/z = 814.12 ($[M]^+$). UV-vis (acetonitrile): λ_{max} = 224 nm (ε = 8800 M^{-1} cm^{-1}), 237 (8600), 276 (8460).

Synthesis of *cis*-*α*-[$Os^{III}(OH)(OH_2)$(BPMCN)](PF_6)$_2$ (4). Complex **3** (50 mg, 52 μmol) was dissolved in water (2.5 mL), and the solution was heated at 70 °C for 2 h.

After the solution was cooled to room temperature, 4 mL of CH_3COOH/CH_3COONa buffer solution (pH 3.8) containing an excess amount of NH_4PF_6 (200 mg, 1.23 mmol) was added to the solution. The concentration of the solution under reduced pressure to ca. 0.5 mL gave orange microcrystals. The microcrystals were collected by filtration and dried in vacuo. Yield: 28.2 mg (64%). Anal. Calcd. for **4**·0.6$(CH_3)_2CO$ ($C_{21.8}H_{34.6}F_{12}N_4O_{2.6}OsP_2$): C, 29.94; H, 3.99; N. 6.41%. Found: C, 30.02; H, 4.17; N, 6.55%. FT-IR (KBr): 3637 ($\nu_{(O–H)}$) and 3407 ($\nu_{(OH2)}$) cm^{-1}. ESI-MS: m/z = 550.20 ($[M–H]^+$). UV-vis (acetate buffer pH 4.0): λ_{max} = 239 nm (ε = 10160 M^{-1} cm^{-1}), 276 (6230), 310 (7600), and 379 (2000).

Synthesis of *cis*-*α*-[Os^V(O)(OH)(BPMCN)]$(ClO_4)_2$ (5). Complex **3** (50 mg, 52 μmol) in H_2O (2.0 mL) was heated at 70 °C for 2 h to generate complex **4** in situ. The solution was then cooled to ca. 5 °C with an ice bath, whereupon 2 equiv. of cerium(IV) ammonium nitrate (56.9 mg, 103.8 μmol) dissolved in a small amount of water was added dropwise to the solution of **4**. The color of the solution immediately changed from yellow to purple. An excess amount of $NaClO_4$ (61 mg, 520 μmol) dissolved in a minimum amount of water was added to the solution, and the resultant solution was kept standing in a refrigerator overnight. Purple crystals precipitated from the solution, which were collected by filtration and washed with cold water, and dried in vacuo. Yield: 11.0 mg (28%). Anal. Calcd. for **5** ($C_{20}H_{33}Cl_2N_4O_{12}Os$): C, 30.69; H, 3.86; N, 7.67%. Found: C, 32.96; H, 4.03; N, 7.67%. FT-IR (KBr): 3568 ($\nu_{(O–H)}$), 885 ($\nu_{(Os=O)}$), and 677 ($\nu_{(Os–OH)}$) cm^{-1}. ESI-MS: m/z = 274.60 ($[M]^{2+}$).

Synthesis of *cis*-*α*-[Os^V(O)(NHTs)(BPMCN)]$(BF_4)_2$ (6). Complex **3** (19.7 mg, 20.5 μmol) in H_2O (1.0 mL) was heated at 70 °C for 2 h to generate complex **4** in situ. Chloramine-T·$3H_2O$ (5.8 mg, 20.6 μmol) dissolved in H_2O (0.25 mL) was added dropwise to the solution of **4**. Color of the solution immediately changed from orange to pale green. $NaBF_4$ (22.9 mg, 0.21 mmol) dissolved in H_2O (0.25 mL) was added to the solution, and the resultant solution kept standing in a refrigerator overnight. Powder precipitated from the solution, which was collected by filtration and dried in vacuo. Purification of **6** was very difficult because of instability of **6** in H_2O to generate **5**. Yield: 4.2 mg (23%). FT-IR (KBr): 862 ($\nu_{(Os=O)}$) and 1230-1300 ($\nu_{(S=O)}$).

Procedures for Catalytic *cis*-1,2-Dihydroxylation and *cis*-1,2-Aminohydroxylation of Styrene. Complex **3** (2.40 mg, 2.5 μmol) in H_2O/^{t}BuOH (1 : 1 *v*/*v*, 3.0 mL) was heated to generate complex **4** in situ. The solution was bubbled with N_2 for 30 min. Styrene (26.0 mg, 250 μmol) and 30% H_2O_2 aq. (24.9 μL, 250 μmol) in 1.0 mL of H_2O/^{t}BuOH (1 : 1 *v*/*v*) were added to the solution, and resulting mixture was stirred at 50 °C for 5 h (Table 1-2, entry 1). In the case of *cis*-aminohydroxylation, chloramine-T (70.4 mg, 250 μmol) was used as an oxidant instead of H_2O_2. Amount of the catalyst and reaction temperature were changed from 1 mol% to 10 mol% and from 50 °C to 30 °C, respectively (Table 1-2, entry 2). After the reaction, a portion of the reaction solution (100 μL) was taken by a microsyringe and diluted with 900 μL of acetonitrile containing anisole (50 μmol) as an internal standard, which was used for the HPLC analysis. The yields of products were determined by comparing the integrated peak areas of the products with that of the internal standard using calibration lines.

X-ray Crystallography. Single crystals were mounted on a loop with a mineral oil, and all X-ray date were collected at –165 °C on a Rigaku R-AXIS RAPID diffractometer using filtered Mo-Kα radiation. The structures were solved by direct method (SIR 2016) and expanded using Fourier techniques. The single crystal of **6** was a co-crystal that comprised of $[Os(O)(NHTs)(BPMCN)](BF_4)_2$ and $[OsCl(NHTs)(BPMCN)](BF_4)_2$ complexes in a 7 : 3 ratio. Parameters of the refinement were minimized by putting this ratio. The non-hydrogen atoms were refined anisotropically by full-matrix least-squares on F^2. The hydrogen atoms were attached at idealized positions on carbon atoms and were not refined. All structures in the final stage of refinement showed no movement in the atom position. The calculations for **1**-**4** were performed using Single-Crystal Structure Analysis Software version 3.8. Those for **5** and **6** were performed using Olex2 program. Crystallographic parameters are summarized in Table 1-1.

Table 1-1. Crystallographic data for *cis*-*α*-[$Os^{III}Cl_2$(BPMCN)]PF_6 (**1**), cis-*β*-[$Os^{III}Cl_2$(BPMCN)]PF_6 (**2**), *cis*-*α*-[$Os^{III}(OTf)_2$(BPMCN)](OTf) (**3**·acetone), *cis*-*α*-[$Os^{III}(OH)(OH_2)$(BPMCN)]$(PF_6)_2$ (**4**·2acetone), *cis*-*α*-[$Os^{V}(O)(OH)$(BPMCN)]$(ClO_4)_2$ (**5**), and *cis*-*α*-[$Os^{V}(O)(NHTs)$(BPMCN)]$(BF_4)_2$ (**6**).

	1	**2**
Formula	$C_{20}H_{28}Cl_2F_6N_4OsP$	$C_{20}H_{28}Cl_2F_6N_4OsP$
Formula weight	730.53	730.53
Crystal system	Orthorhombic	Orthorhombic
Space group	*I*bca (#73)	$P2_12_12_1$ (#19)
a, Å	13.6052(6)	11.5662(7)
b, Å	15.9620(9)	12.9354(8)
c, Å	22.1031(10)	15.9995(9)
α, deg	90.000	90.000
β, deg	90.000	90.000
γ, deg	90.000	90.000
V, Å^3	4800.0(4)	2393.7(2)
Z	8	4
D_{calcd}, g/cm^{-3}	2.022	2.027
F(000)	2840.00	1420.00
μ(Mo-Kα), cm^{-1}	56.67	56.82
Crystal size, mm	0.15 × 0.13 × 0.05	0.18 × 0.10 × 0.10
T, K	103	110
$2\theta_{max}$, deg	54.9	54.9
No. of reflns obsd	2750	5435
No. of params	156	309
R_1[a]	0.0507	0.0217
wR_2[b]	0.1254	0.0404
GOF	1.212	1.087

[a] $R_1 = \Sigma(|F_o| - |F_c|)/\Sigma|F_o|$

[b] $wR_2 = [\Sigma(w(F_o^2 - F_c^2)^2)/\Sigma w(F_o^2)^2]^{1/2}$

Table 1-1. Crystallographic data for *cis*-*α*-[$Os^{III}Cl_2$(BPMCN)]PF_6 (**1**), cis-*β*-[$Os^{III}Cl_2$(BPMCN)]PF_6 (**2**), *cis*-*α*-[$Os^{III}(OTf)_2$(BPMCN)](OTf) (**3**·acetone), *cis*-*α*-[Os^{III}(OH)(OH_2)(BPMCN)]$(PF_6)_2$ (**4**·2acetone), *cis*-*α*-[Os^{V}(O)(OH)(BPMCN)]$(ClO_4)_2$ (**5**), and *cis*-*α*-[Os^{V}(O)(NHTs)(BPMCN)]$(BF_4)_2$ (**6**) (continued).

	3·acetone	**4**·2acetone
Formula	$C_{26}H_{34}F_9N_4O_{10}OsS_3$	$C_{26}H_{43}F_{12}N_4O_4OsP_2$
Formula weight	1019.95	955.78
Crystal system	Monoclinic	Monoclinic
Space group	$P2_1/c$ (#14)	$C2/c$ (#15)
a, Å	10.9603(7)	15.2378(6)
b, Å	12.4093(8)	18.2572(8)
c, Å	25.8422(16)	25.4750(11)
α, deg	90.000	90
β, deg	92.279(6)	90.009(6)
γ, deg	90.000	90.000
V, Å^3	3512.0(4)	7087.1(5)
Z	4	8
D_{calcd}, g/cm^{-3}	1.929	1.792
F(000)	2012.00	3784.00
μ(Mo-Kα), cm^{-1}	39.16	37.90
Crystal size, mm	0.50 × 0.30 × 0.20	0.35 × 0.20 × 0.20
T, K	110	103
$2\theta_{max}$, deg	55.1	54.9
No. of reflns obsd	8056	8108
No. of params	482	487
R_1[a]	0.0797	0.457
wR_2[b]	0.1958	0.1084
GOF	1.059	1.092

[a] $R_1 = \Sigma(|F_o| - |F_c|)/\Sigma|F_o|$

[b] $wR_2 = [\Sigma(w(F_o^2 - F_c^2)^2)/\Sigma w(F_o^2)^2]^{1/2}$

Table 1-1. Crystallographic data for *cis*-*α*-[$Os^{III}Cl_2$(BPMCN)]PF_6 (**1**), cis-*β*-[$Os^{III}Cl_2$(BPMCN)]PF_6 (**2**), *cis*-*α*-[$Os^{III}(OTf)_2$(BPMCN)](OTf) (**3**·acetone), *cis*-*α*-[$Os^{III}(OH)(OH_2)$(BPMCN)]$(PF_6)_2$ (**4**·2acetone), *cis*-*α*-[$Os^{V}(O)(OH)$(BPMCN)]$(ClO_4)_2$ (**5**), and *cis*-*α*-[$Os^{V}(O)(NHTs)$(BPMCN)]$(BF_4)_2$ (**6**) (continued).

	5	**6**
Formula	$C_{20}H_{28}Cl_2N_4O_{10}Os$	$C_{27}H_{37}B_2Cl_{0.3}F_8N_5O_{3.7}OsS$
Formula weight	745.57	897.33
Crystal system	Monoclinic	Triclinic
Space group	*C*2/*c* (#15)	$P\bar{1}$ (#2)
a, Å	20.222(2)	10.7487(7)
b, Å	9.6151(11)	12.7285(8)
c, Å	16.2829(19)	13.4861(9)
α, deg	90.000	63.166(4)
β, deg	127.025(2)	83.645(6)
γ, deg	90.000	89.857(6)
V, Å^3	2527.6(5)	1633.95(19)
Z	4	2
D_{calcd}, g/cm^3	1.959	1.824
F(000)	1464.00	885.00
μ(Mo-K*α*), cm^{-1}	53.15	40.78
Crystal size, mm	0.15 × 0.15 × 0.10	0.40 × 0.40 × 0.20
T, K	103	100
$2\theta_{max}$, deg	55.1	55.0
No. of reflns obsd	2890	7477
No. of params	186	471
R_1[a]	0.0452	0.0303
wR_2[b]	0.1176	0.0813
GOF	1.191	1.164

[a] $R_1 = \Sigma(|F_o| - |F_c|)/\Sigma|F_o|$

[b] $wR_2 = [\Sigma(w(F_o^2 - F_c^2)^2)/\Sigma w(F_o^2)^2]^{1/2}$

Results and Discussion

Preparation, Characterization, and Crystal Structures of Osmium(III) Complexes Supported by a Cyclohexanediamine-Based Tetradentate Ligand (BPMCN)

The synthetic procedures of the osmium complexes supported by BPMCN are outlined in Scheme 1-3. BPMCN can adopt three conformations, *cis*-α, *cis*-β, and planar, in an octahedral metal complex. Among the three conformations, the *cis*-α one is the most energetically stable, so that most of complexes with BPMCN so far been reported take the *cis*-α structure.[23] In Chapter 1, the author obtained both *cis*-α and *cis*-β isomers of the dichloro-osmium(III) complexes, **1** and **2**, by the treatment of $(NH_4)_2[Os^{IV}Cl_6]$ with BPMCN. When the reaction was carried out in ethylene glycol at 145 °C for 15 min, **1** having a *cis*-α structure was isolated as a PF_6 salt. On the other hand, when the ethylene glycol solution was refluxed for 3 min, **2** adopting a *cis*-β form was obtained as a PF_6 salt. Since **1** and **2** were purified by column chromatography and the yields were low (**1**: 18%, **2**: 11%), their formation mechanisms from $(NH_4)_2[Os^{IV}Cl_6]$ are unclear.

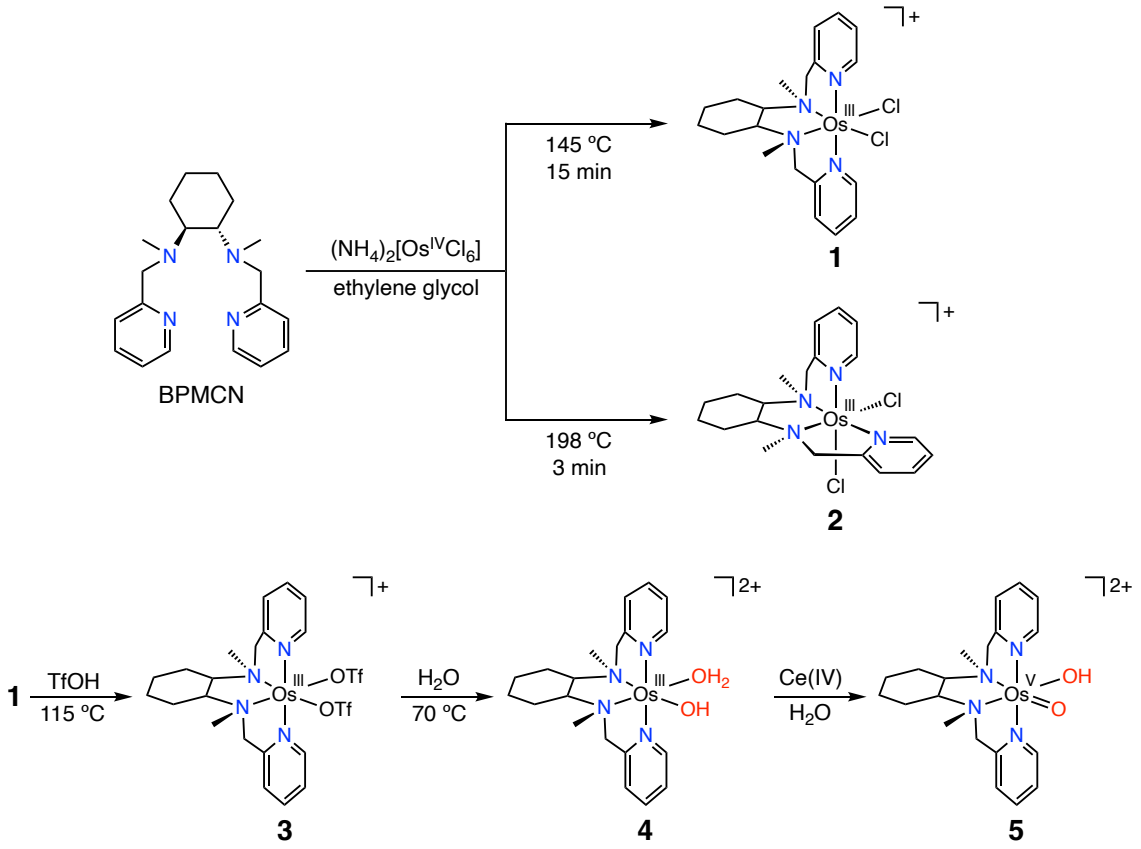

Scheme 1-3. Synthetic procedures of osmium complexes **1**-**5**.

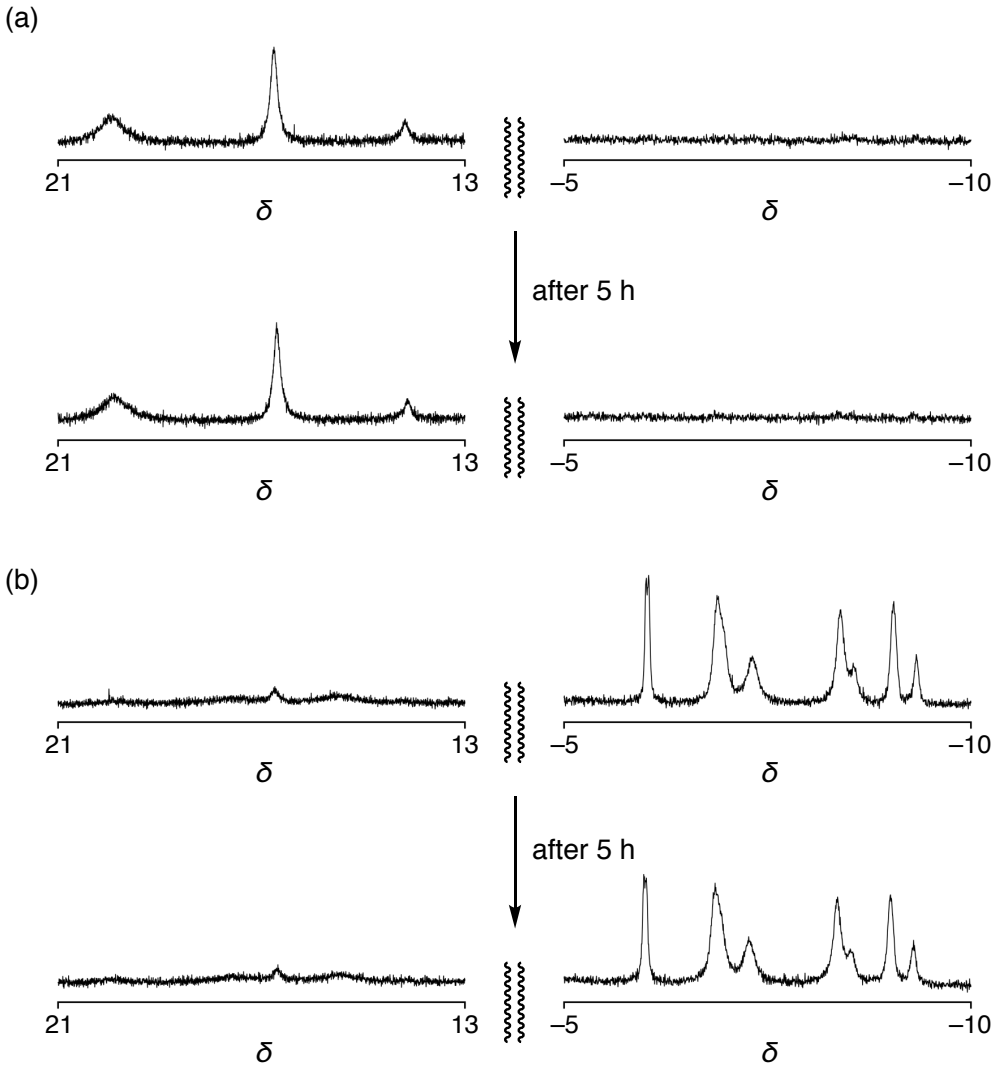

Figure 1-1. ^{1}H NMR spectra of (a) complex **1** and (b) complex **2** in acetone-d_6 at ambient temperature.

^{1}H NMR spectra of **1** and **2** were measured in acetone-d_6 to see whether isomerization between the two isomers occurs. As shown in Figure 1-1, the spectra of both **1** and **2** were kept unchanged at all after standing 5 h at ambient temperature, indicating that no interconversion took place between them (^{1}H NMR spectra in a wide range are given in Figure 1-S1).

cis-*α*-Dichloro-osmium(III) complex **1** was then converted into the ditriflato-osmium(III) complex **3** by treating **1** with neat HOTf at 115 °C. Under the same conditions, the ditriflate derivative of **2** was not formed. In the preparation of the ditriflato-osmium(III) complex with a tetradentate TPA [tris(2-pyridylmethyl)amine] ligand, the dichloro-derivative was spontaneously converted into the oxido-acetato-

bridged diosmium(III) complex under basic conditions using CH_3COONa because of the quite strong osmium(III)-chloride coordination bonds under acidic conditions.[15] Presence of the two tertiary amine nitrogen atoms situated at the *trans* positions of the chloride ligands in **3** can enable direct replacement of the chloride ligands with triflate anions, using the stronger trans effect of the amine nitrogen atom as compared to that of the pyridinyl nitrogen atom of the TPA complex. Then, complex **3** was converted into the hydroxido-aquo-osmium(III) complex **4** by hydrolysis in H_2O at 70 °C, which was isolated as pale yellow crystals with two PF_6^- counter anions. Appearance of bands at 3637 and 3407 cm^{-1} in the IR spectrum of **4** is consistent with the presence of hydroxide and aqua ligands.

Crystal Structure Description

The crystal structures of complexes **1** and **2** are shown in Figure 1-2(a) and Figure 1-2(b), respectively. Both osmium atoms are coordinated by the four nitrogen atoms of the ligand and two chlorine atoms to adopt distorted octahedrons. The octahedral structure of **2** is more distorted when compare with that of **1** in that the bond angles of N(2)–Os(1)–N(4) of **2** [166.04(18)°] is significantly smaller than that of **1** [174.8(3)°]. With respect to the orientation of the two *N*-methyl groups of BPMCN, the methyl groups

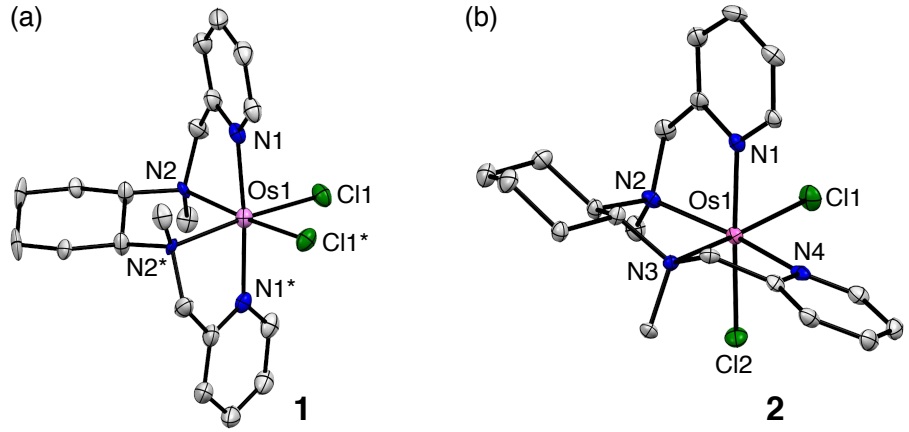

Figure 1-2. ORTEP drawings of (a) complex **1** and (b) **2** showing 50% probability thermal ellipsoids. Hydrogen atoms and counter anion are omitted for clarity. Selected bond lengths (Å) and angles (°): (a) Os(1)–Cl(1), 2.366(2); Os(1)–N(1), 2.082(7); Os(1)–N(2), 2.137(6); N(1)–Os(1)–N(1*), 174.8(3). (b) Os(1)–Cl(1), 2.3493(14); Os(1)–Cl(2), 2.3840(15); Os(1)–N(1), 2.070(5); Os(1)–N(2), 2.132(5); Os(1)–N(3), 2.116(4); Os(1)–N(4), 2.066(5); N(2)–Os(1)–N(4), 166.04(18).

of **1** take the *trans*-configuration with respect to the equatorial plane consisting with the tertiary amine nitrogen atoms N(2) and N(2*) and two chlorine atoms Cl(1) and Cl(1*), while those of **2** are situated at the *cis* position with respect to the plane consisting with the two amine nitrogen atoms N(2) and N(3), pyridine nitrogen N(4), and one chlorine atom Cl(1). In complex **2**, the two amine nitrogen atoms N(2) and N(3) are inequivalent in that the one nitrogen N(1) is located *trans* at the chlorine atom Cl(2), while another nitrogen N(4) is *trans* to the nitrogen N(2). The structural stability of the isomers, as confirmed in the ^{1}H NMR spectra of **1** and **2** (Figure 1-1), is ascribed to the fact that the *anti*-orientation favors the *cis*-*α* form while the *syn*-configuration favors the *cis*-*β* structure. If isomerization between the two isomers occurred, one N_{py} and one N_{amine} atoms should be dissociated from the osmium(III) center to rotate the attached *N*-methyl group.

The crystal structure of *cis*-*α*-ditriflato-osmium(III) complex **3** is shown in Figure 1-3(a). The overall structure is similar to that of **1** except that two chloride ligands in **1** are replaced with two triflate ligands in **3**. In this case as well, the two *N*-methyl groups [N(2) and N(3)] of BPMCN have *anti*-configuration with respect to the equatorial plane.

The crystal structure of *cis*-*α*-hydroxido-aquo-osmium(III) complex **4** is shown in

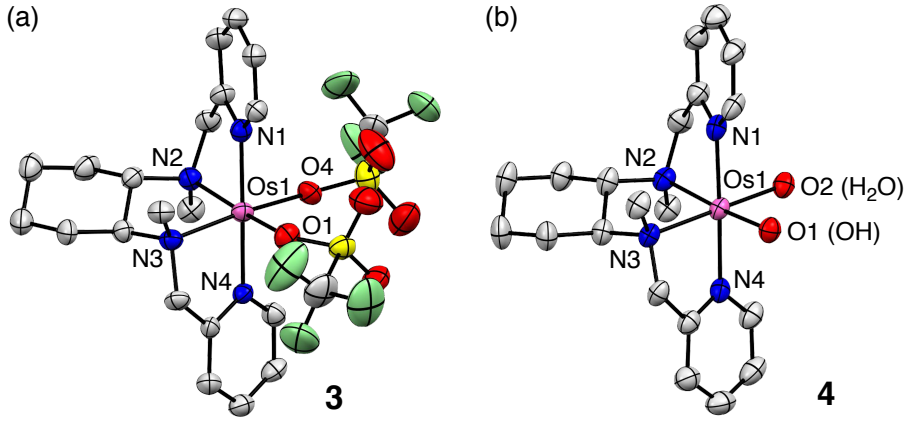

Figure 1-3. ORTEP drawings of (a) complex **3** and (b) **4** showing 50% probability thermal ellipsoids. Hydrogen atoms and counter anion are omitted for clarity. Selected bond lengths (Å) and angles (°): (a) Os(1)–O(1), 2.107(6); Os(1)–O(4), 2.111(5); Os(1)–N(1), 2.070(6); Os(1)–N(2), 2.079(7); Os(1)–N(3), 2.077(6); Os(1)–N(4), 2.075(7); N(1)–Os(1)–N(4), 179.3(2). (b) Os(1)–O(1), 2.035(5); Os(1)–O(2), 2.054(5); Os(1)–N(1), 2.072(6); Os(1)–N(2), 2.121(6); Os(1)–N(3), 2.102(6); Os(1)–N(4), 2.075(6); N(1)–Os(1)–N(4), 177.7(2).

Figure 1-3(b). The overall structure of **4** is close to those of **1** and **3**, but having two oxygen atoms O(1) and O(2) instead of two chlorine atoms in **1** and two triflate anions in **3**. As found in the crystal structures of **1** and **3**, the two methyl groups of **4** are *trans* to each other. Although both oxygen atoms O(1) and O(2) are located *trans* to the tertiary amine nitrogen atoms, the bond lengths between the Os(1) and oxygen atoms are different. Thus, the O(1) atom giving a shorter Os–O distance of 2.035(5) Å is assigned to a hydroxide ligand oxygen, whereas O(2) atom showing a longer Os–O distance of 2.054(5) Å is assigned to the aqua ligand oxygen.

Catalytic *cis*-Dihydroxylation and *cis*-Aminohydroxylation of Styrene and Characterization of the Active Oxidants

Catalytic activity of *cis*-*α*-hydroxido-aquo-osmium(III) complex **4** was examined in the dihydroxylation and aminohydroxylation of styrene. The results are summarized in Table 1-2. Styrene was converted into the corresponding diol and aminoalcohol in moderate yields by the reactions with H_2O_2 and chloramine-T, respectively, in the presence of a catalytic amount of **4**. The diol product was also obtained as a by-product in the aminohydroxylation with chloramine-T. Such diol formation was also found in our previous aminohydroxylation reaction of alkenes with chloramine-T in aqueous media catalyzed by the osmium(III) complex with a macrocyclic tetradentate ligand L-N_4Me_2.[20] The product characterization in entry 2 also revealed that 170 μmol of styrene (68%) remained and 158 mmol of chloramine-T (63%) was converted to *para*-

Table 1-2. *cis*-Dihydroxylation and *cis*-aminohydroxylation reactions of styrene catalyzed by $Os^{III}(OH)(H_2O)$ complex **4**.[a]

Entry	Oxidant	Product yield, %[b]
1[c]	H_2O_2	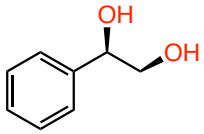 47
2[d]	Chloramine-T	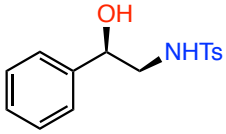 4 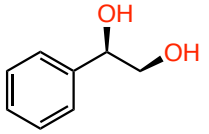 18

[a] Conditions: [styrene] = 62.5 mM, [H_2O_2] = 62.5 mM of [chloramine-T] = 62.5 mM in H_2O/^{t}BuOH (v : v = 1 : 1, 4.0 mL) under N_2. [b] HPLC yield based on the substrate. [c] [**4**] = 0.63 mM, 50 °C. [d] [**4**] = 6.25 mM, 30 °C.

toluenesulfoneamide ($TsNH_2$). Thus, the reaction was terminated by consumption of chloramine-T. The product yield of the aminoalcohol was not changed by prolonging the reaction time (from 5 to 10 h) and increasing the reaction temperature (from 30 to 50 °C). The catalytic efficiency of **4** for *cis*-aminohydroxylation was significantly lower than those of the L-N_4Me_2 derivative and OsO_4 for the reaction.[17, 18, 20]

Our group has already reported that oxido-hydroxido-osmium(V) complexes coordinated with tetradentate ligands work as the active oxidant for *cis*-dihydroxylation of alkenes.[15, 16] The active oxidants can be generated electrochemically from the hydroxido-aquo-osmium(III) complexes and also by the oxidation with H_2O_2 or cerium(IV) ammonium nitrate (CAN). In this study, the oxido-hydroxido-osmium(V) complex, *cis*-*α*-[Os^V(O)(OH)(BPMCN)]$(ClO_4)_2$ (**5**), was obtained as pale blue crystals by oxidizing **4** with CAN (see Experimental Section). The crystal structure of **5** is shown in Figure 1-4. BPMCN coordinates to Os center in a manner similar to those in **1**, **3**, and **4** to adopt a *cis*-*α* structure. The Os atom is on a two-fold axis of the cationic part. The bond length of Os(1)–O(1) of 1.769(5) Å, that is an average of Os=O and Os–OH bond lengths, is shorter than the average of Os–OH and Os–OH_2 bond lengths of hydroxido-aquo-osmium(III) complex **4** [2.040(4) and 2.071(4) Å], reflecting the higher oxidation number of the osmium center of **5** as compared with that in **4**. Due to the repulsion between the two short Os(1)–O(1) and Os(1)–O(1*) bonds, the angle of O(1)–Os(1)–O(1*) becomes more obtuse as 114.9(2)°. By comparing the dimension of

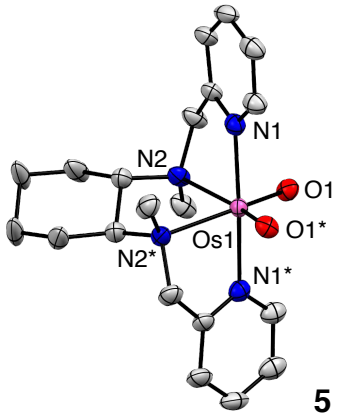

Figure 1-4. ORTEP drawing of complex **5** showing 50% probability thermal ellipsoids. Hydrogen atoms and counter anion are omitted for clarity. Selected bond lengths (Å) and angles (°): Os(1)–O(1), 1.769(5); Os(1)–N(1), 2.100(5); Os(1)–N(2), 2.208(6); O(1)–Os(1)–O(1*), 114.9(2); N(1)–Os(1)–N(1*), 177.79(16).

the O(1)–Os(1)–O(1*) core of **5** with those of the oxido-hydroxido-osmium(V) analogues coordinated with tripodal TPA and macrocyclic L-N_4Me_2 ligands,[15, 16] it is revealed that the Os–O(1) bond length of **5** is longer than the osmium(V)-oxo bond lengths in the analogues [1.726(8) Å for TPA, 1.753(5) Å for L-N_4Me_2] but shorter than osmium(V)-hydroxido bond lengths in the two complexes [1.902(7) Å for TPA and 1.921(4) Å for L-N_4Me_2]. The Os(1)–O(1) bond length is also longer than that of seven coordinate $[Os^{V}(O)Cl(4\text{-picoline})\text{-}(2,2':6',2'':6'',2'''\text{-quaterpyridine})](PF_6)_2$ [1.7375(32) Å].[24]

Next, the author tried to identify an active oxidant in the styrene aminohydroxylation. Figure 1-5(a) shows UV-vis spectral changes of the hydoxido-aquo-osmium(III) complex **4** by adding 1 equiv. of chloramine-T in H_2O. The spectral changes consisted of two phases. In the first phase, the spectrum of complex **4** (blue line) immediately changed to the one having an absorption band at 310 nm (black line). Then, the black lined spectrum gradually changed to a new one having an absorption band at 260 nm (red line) with isosbestic points at 227, 249, and 272 nm. The final spectrum (red line) was fairly similar to that of **5**, indicating formation of an osmium(V) complex **6**. As shown in Figure 1-5(b), an ESI-MS (electro-spray-ionization mass spectrum) of the final solution exhibited a peak cluster at m/z = 351.15, the isotope distribution pattern of which matched well with that of $[Os(O)(NHTs)(BPMCN)]^{2+}$ or $[Os(OH)(NTs)(BPMCN)]^{2+}$ (ESI-MS in a wide range is given in Figure 1-S2). Formation of such osmium(V) species was also

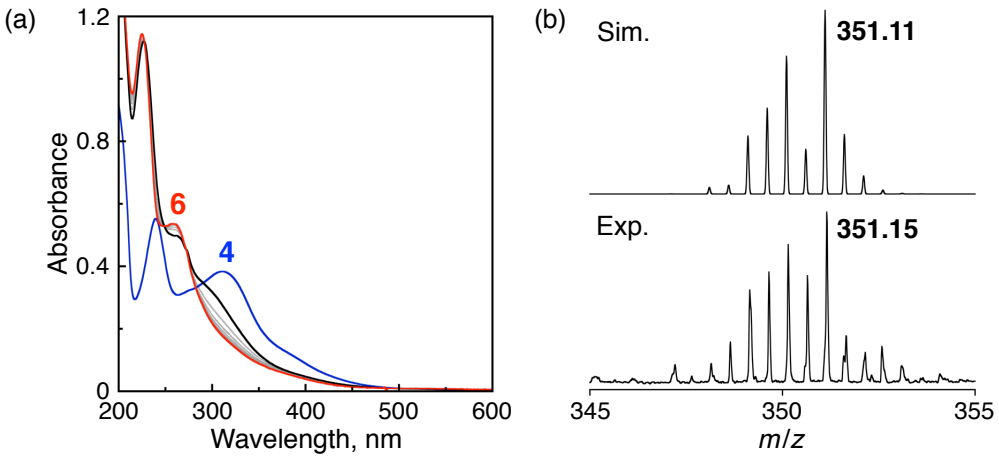

Figure 1-5. (a) UV-vis spectral changes measured every 450 s upon an addition of 1 equiv. of chloramine-T to $[Os^{III}(OH)(H_2O)(BPMCN)]^{2+}$ (**4**) in H_2O (blue → black → red). (b) ESI-mass spectrum of the final reaction mixture of **4** and chloramine-T.

observed in the oxidation of hydoxido-aquo-osmium(III) complex having L-N_4Me_2 with chloramine-T.[16] Other peak cluster was observed at m/z = 275.14, which corresponded to a mixture of $[Os^{V}(O)(OH)(BPMCN)]^{2+}$ and $[Os^{IV}(O)(H_2O)(BPMCN)]^{2+}$ (Figure 1-S2). These species might be generated by hydrolysis of **6**. Complex **6** was successfully isolated as a red powder in H_2O after a counter anion exchange of PF_6^- with BF_4^- though the powder contained the oxido-hydroxido-osmium(V) complex **5**. Figure 1-6 shows an IR spectrum of **6** (red line) together with that of *cis*-*α*-$[Os^{V}(O)(OH)(BPMCN)](ClO_4)_2$ (**5**) (black line). The spectrum of **6** exhibited a peak at 862 cm^{-1}, which is shifted to lower energy direction when compared with that of complex **5** (885 cm^{-1}) by 23 cm^{-1}. The peak at 885 cm^{-1} of complex **5** was confirmed to be an Os^{V}=O stretching vibration by isotope labeling experiments using $H_2{}^{18}O$ (see Figure 1-S3). From these results, the author assigned the peak at 862 cm^{-1} of complex **6** as Os^{V}=O stretching vibration. If so, the structure of **6** can be drawn as $[Os^{V}(O)(NHTs)(BPMCN)]^{2+}$ {oxido-aminato-osmium(V)} rather than $[Os^{V}(OH)(NTs)(BPMCN)]^{2+}$ {hydroxido-imido-osmium(V)}. The lower energy shift of the $\nu(Os^{V}=O)$ stretch of **6** (862 cm^{-1}) as compared to that of **5** (885 cm^{-1}) may be due to the larger degree of delocalization of the lone pair electrons from the amido group (Os^{V}–NHTs) to the *anti*-bonding orbital of the Os^{V}=O bond in **6** as compared to that from the hydroxido group (Os^{V}–OH) to the oxido group (Os^{V}=O) in **5**, making the double bond character in **6** slightly weaker than that in **5**. The IR spectrum of **6** also had peaks in a range from 1230 to 1300 cm^{-1}, that can be assigned to the stretching vibrations of –SO_2– group of the tosyl moiety.

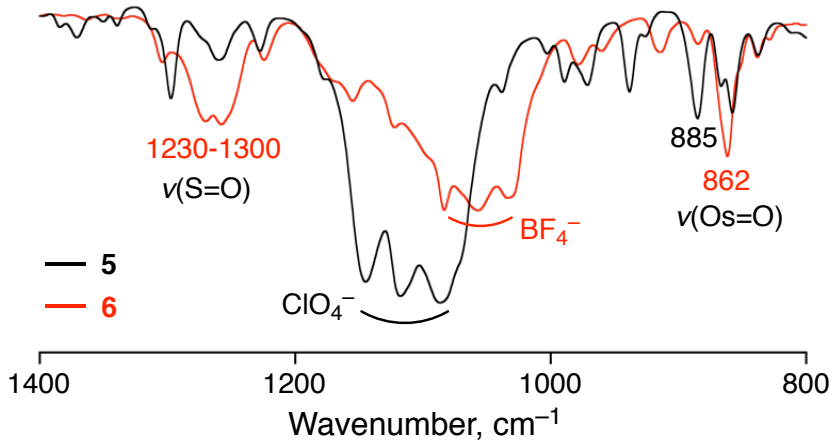

Figure 1-6. FT-IR spectra of $[Os^{V}(O)(OH)(BPMCN)](ClO_4)_2$ (**5**, black line) and $[Os^{V}(O)(NHTs)(BPMCN)](BF_4)_2$ (**6**, red line).

As noted above, complex **6** is easily converted to *cis*-*α*-Os^{V}(O)(OH) complex **5** in H_2O. Nonetheless, the author succeeded to isolate single crystals of complex **6** as a BF_4^- salt, and determined its crystal structure by X-ray crystallography, where the crystals were analyzed as a co-crystal of $[Os^{V}(O)(NHTs)(BPMCN)](BF_4)_2$ and $[OsCl(NHTs)(BPMCN)](BF_4)_2$ complexes in a 7 : 3 ratio. The chloride ligand in the minor component is derived from chloramine-T (TsNClNa). The crystal structure of **6** is shown in Figure 1-7. The Os(1) atom is coordinated with the four nitrogen atoms N(1), N(2), N(3), and N(4) of BPMCN, and the remaining two coordination sites are occupied by oxygen atom O(1) of the oxido group and nitrogen atom N(5) of the –NHTs group. The aromatic ring of the tosyl group and a pyridine ring of the tetradentate ligand overlapped each other with a distance of 3.5 Å, indicating the existence of a *π*-*π* stacking interaction. Such a *π*-*π* stacking interaction may stabilize the core structure making it possible to crystallize **6**. The Os(1)–O(1) bond length of 1.784(4) Å is comparable to the bond lengths of Os^{V}=O in our previously reported oxido-hydroxido-osmium(V) complexes supported by other tetradentate ligands L-N_4Me_2 and TPA [1.753(5) Å and 1.726(8) Å], which supports assignment of the O(1) atom as a dianionic oxide ligand.[15, 16] Dimension around the Os–NTs moiety is also compared to those of the related Os=NR and Os–NR_2 complexes so far been reported (Table 1-3).

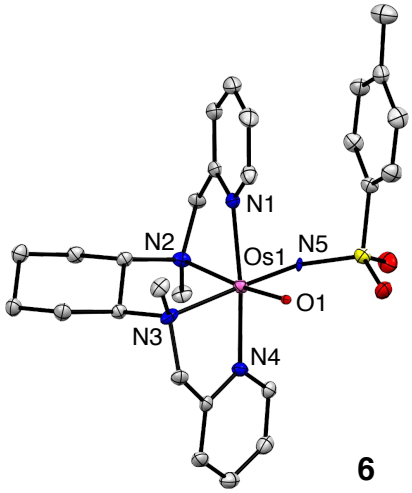

Figure 1-7. ORTEP drawing of complex **6** showing 50% probability thermal ellipsoids. Hydrogen atoms, counter anions, and chloride ion of a minor component, $[OsCl(NHTs)(BPMCN)](PF_6)_2$, are omitted for clarity. Selected bond lengths (Å) and angles (°): Os(1)–O(1), 1.784(4); Os(1)–N(1), 2.095(5); Os(1)–N(2), 2.127(3); Os(1)–N(3), 2.110(3); Os(1)–N(4), 2.082(5); Os(1)–N(5), 2.058(5); O(1)–Os(1)–N(5), 99.1(1); Os(1)–N(5)–S, 128.8(2).

Table 1-3. Selected bond length [Å] and angles [°] of complexes **6**, **A**, **B**, and **C**.

	Os–NR_2, Å	Os=NR, Å	Os-N-S, °	Ref.
$[Os^{V}(O)(NHTs)(BPMCN)]^{2+}$ (**6**)	2.058(4)		128.0(2)	[d]
$[Os^{VI}(O)(N^{t}Bu)(TTP)]^{2+}$ (**A**)[a]		1.759(9)		25
$[Os^{IV}(tmen–H)_2(tmen)]^{2+}$ (**B**)[b]	2.146(6)	1.880(6)		26
$[Os^{II}(TsDPEN)(biphenyl)]$ (**C**)[c]	2.066(4)		128.1(3)	27

[a] TTP: *meso*-tetrakis(*p*-tolyl)porphyrin. [b] tmen: 1,1,2,2-tetramethylethylenediamine. [c] TsDPEN: *N*-(*p*-toluenesulfonyl)-1,2-diphenylethylenediamine. [d] This work.

The Os(1)–N(5) bond length of 2.058(4) Å in **6** is longer than the bond length of Os=NR double bonds in $[Os^{VI}(O)(N^{t}Bu)(TTP)]^{2+}$ (**A**) {Os^{VI}=NR; 1.759(9) Å} having a porphyrin ring {TTP: *meso*-tetrakis(*p*-tolyl)porphyrin}[25] and $[Os^{IV}(tmen–H)_2(tmen)]^{2+}$ (**B**) {Os^{IV}=NR; 1.880(6) Å} chelated by 1,1,2,2-tetramethylethylenediamine (tmen) and its deprotonated (amide) form (tmen–H).[26] On the other hand, this bond length is close to those of Os–NR_2 single bonds in complex **B** {2.146(6) Å} and $[Os^{II}(TsDPEN)(biphenyl)]$ (**C**) {TsDPEN; *N*-(*p*-toluenesulfonyl)-1,2-diphenylethylenediamine} {2.066(4) Å}.[27] The Os(1)–N(5)–S angle of 128.0(2)° in **6** is also comparable to the Os–N–S angle in complex **C** containing an anionic –NHTs group. The O(1)–Os(1)–N(5) angle {98.6(2)°} is more obtuse than the O(1)–Os(1)–O(2) angle {91.4(2)°} of the $Os^{III}(OH)(H_2O)$ complex **4**, due to the stronger electronic repulsion of the Os–NTs single bond and the Os=O double bond as compared to the repulsion between the Os–OH single bond and the Os–OH_2 single bond in **4**. On the other hand, this bond angle is more acute when compared with the O(1)–Os(1)–O(1*) angle (114.9°) of the $Os^{V}(O)(OH)$ complex **5**, which reflects decrease of the steric repulsion between the N(5) and O(1) atoms by the elongated Os(1)–N(5) bond length {2.058(4) Å} in **6** as compared to the Os(1)–O(1*) bond length {1.769(5) Å} in **5**.

An acetonitrile solution dissolving the isolated powder that contains **5** and **6** was treated with an excess amount of styrene to see whether **6** works as an active oxidant for the 1,2-aminohydroxylation of alkenes. HPLC analysis of the reaction solution revealed formation of the corresponding aminoalcohol and diol products (see Figure 1-S4). The UV-vis spectrum of the reaction solution was nearly identical to that of $Os^{III}(OH)(H_2O)$ complex **4**. These results demonstrate that complex **6** is an active oxidant for the 1,2-

aminohydroxylation of styrene. The diol product was derived from the oxido-hydroxido-osmium(V) complex **5** contained in the solution. Our group has reported that oxido-hydroxido-osmium(V) complexes with tetradentate ligands work as an active oxidant for the 1,2-dihydroxylation of alkenes, where a five-membered glycolate osmium(III) intermediate is formed by the reaction of the active oxidant and alkenes.[15, 16] Our group also reported that a five-membered Os(NHTs–C–C–O) species was involved in a catalytic cycle of *cis*-aminohydroxylation of alkenes by $Os^{III}(OH)(H_2O)$ complex with L-N_4Me_2. Though direct evidence for formation of such five-membered species was not obtained, in a similar manner to the dihydroxylation and aminohydroxylation reactions,[15, 16] the present aminohydroxylation may proceed *via* formation of a five-membered [3+2]-cycloadduct as shown in Scheme 1-4.

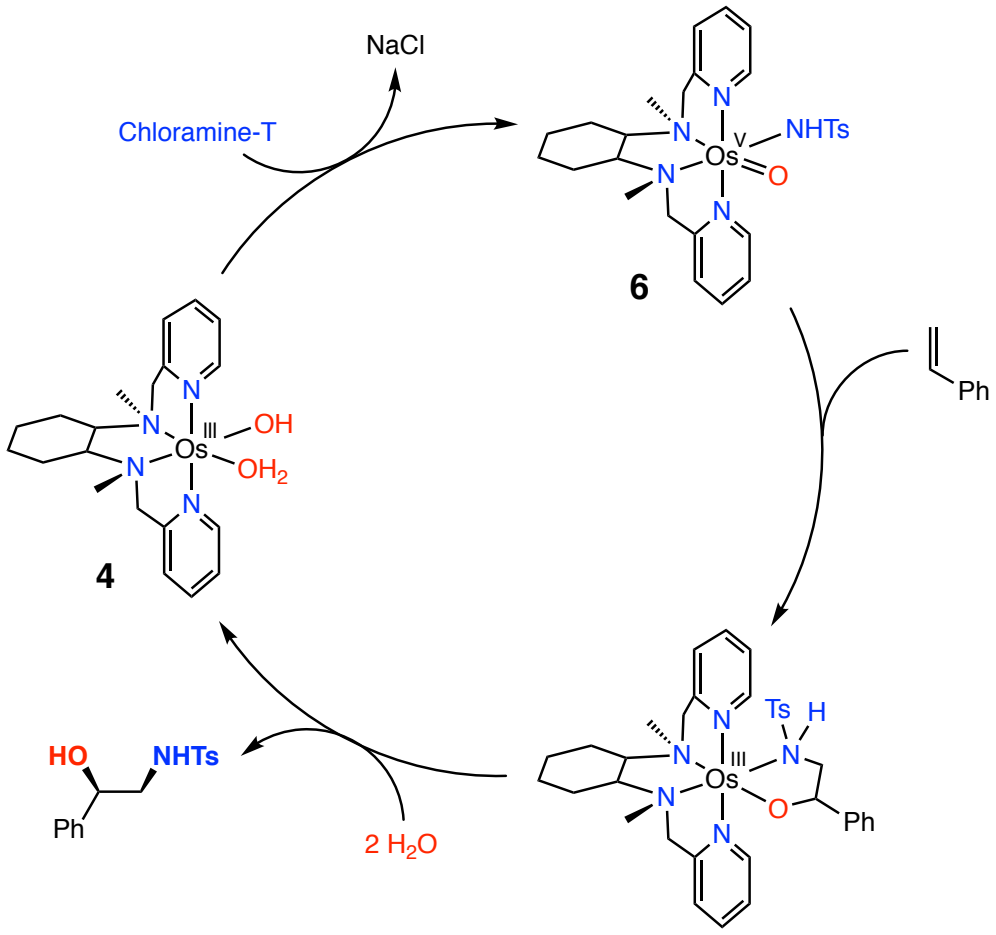

Scheme 1-4. Catalytic cycle of 1,2-aminohydroxylation reaction.

Conclusions

cis-*α*-Hydroxido-aquo-osmium(III) complex **4** coordinated with a cyclohexanediamine-based tetradentate ligand, BPMCN, was synthesized and characterized. In the synthesis of the complex, *cis*-*α*-dichlorido- (**1**) and *cis*-*α*-ditriflato-osmium(III) complexes (**3**) were synthesized as the precursors. The *cis*-*β* isomer of **1** was also prepared as **2**. The *cis*-*α*-hydroxido-aquo-osmium(III) complex (**4**) worked as a pre-catalyst for the *cis*-selective dihydroxylation and aminohydroxylation of styrene with H_2O_2 and TsNClNa, respectively. As an active oxidant for the dihydroxylation, *cis*-*α*-oxido-hydroxido-osmium(V) complex (**5**) was isolated and crystallographically characterized. Further, a product obtained by a reaction of complex **4** with TsNClNa was identified as a *cis*-*α*-oxido-aminato-osmium(V) complex (**6**) by ESI-mass, FT-IR, and UV-vis spectra as well as X-ray crystallographic technique. The structural analysis also indicated that the Os^{V}–NHTs bond has a single bond character. Formation of the aminoalcohol by the reaction of *cis*-*α*-oxido-aminato-osmium(V) complex with styrene revealed that the osmium(V) complex was the active oxidant for the aminohydroxylation. The generated oxido-aminato-osmium(V) complex **6** binds to styrene in a [3+2] cycloaddition manner similar to the dihydroxylation. Subsequent hydrolysis of the five membered intermediate produces the starting osmium(III) complex and the aminoalcohol product. The present study adds a new metal-oxide complex that have an additional functional group, OsO(NHTs), for alkene aminohydroxylation reaction.

References

1. K. B. Cho, H. Hirao, S. Shaik, W. Nam, *Chem*. *Soc*. *Rev*. **2016**, *45*, 1197-1210.
2. P. Pirovano, A. R. McDonald, *Eur*. *J*. *Inorg*. *Chem*. **2018**, *2018*, 547-560.
3. X. Huang, J. T. Groves, *Chem*. *Rev*. **2018**, *118*, 2491-2553.
4. Y. Liu, T. C. Lau, *J*. *Am*. *Chem*. *Soc*. **2019**, *141*, 3755-3766.
5. M. Guo, T. Corona, K. Ray, W. Nam, *ACS Cent*. *Sci*. **2019**, *5*, 13-28.
6. K. N. Ferreira, T. M. Iverson, K. Maghlaoui, J. Barber, S. Iwata, *Science* **2004**, *303*, 1831-1838.
7. H. L. Wilson, K. V. Rajagopalan, *J*. *Biol*. *Chem*. **2004**, *279*, 15105-15113.
8. T. L. Poulos, *Chem*. *Rev*. **2014**, *114*, 3919-3962.

9. M. C. Tang, Y. Zou, K. Watanabe, C. T. Walsh, Y. Tang, *Chem*. *Rev*. **2017**, *117*, 5226-5333
10. F. P. Guengerich, F. K. Yoshimoto, *Chem*. *Rev*. **2018**, *118*, 6573-6655.
11. H. C. Kolb, M. S. VanNieuwenhze, K. B. Sharpless, *Chem*. *Rev*. **1994**, *94*, 2483-2547.
12. E. J. Corey, S. Sarshar, M. D. Azimioara, R. C. Newbold, M. C. Noe, *J*. *Am*. *Chem*. *Soc*. **1996**, *118*, 7851-7852.
13. D. W. Nelson, A. Gypser, P. T. Ho, H. C. Kolb, T. Kondo, H.-L. Kwong, D. V. McGrath, A. E. Rubin, P.-O. Norrb, K. P. Gable, K. B. Sharpless, *J*. *Am*. *Chem*. *Soc*. **1997**, *119*, 1840-1858.
14. T. J. Donohoe, R. M. Harris, S. Butterworth, J. N. Bur- rows, A. Cowley, J. S. Parker, *J*. *Org*. *Chem*. **2006**, *71*, 4481-4489.
15. H. Sugimoto, K. Kitayama, S. Mori, S. Itoh, *J*. *Am*. *Chem*. *Soc*. **2012**, *134*, 19270-19280.
16. H. Sugimoto, K. Ashikari, S. Itoh, *Chem*. *Asian J*. **2013**, *8*, 2154-2160.
17. K. Muñiz, *Chem. Soc*. *Rev*. **2004**, *33*, 166-174.
18. K. B. Sharpless, T. Hori, *J*. *Org*. *Chem*. **1976**, *41*, 177-179.
19. B. S. McGilligan, J. Arnold, G. Wilkinson, B. Hussian-Bates, M. B. Hursthouse, *J*. *Chem*. *Soc*., *Dalton Trans*. **1990**, 2465-2475.
20. H. Sugimoto, A. Mikami, K. Kai, P. K. Sajith, Y. Shiota, K. Yoshizawa, K. Asano, T. Suzuki, S. Itoh, *Inorg*. *Chem*. **2015**, *54*, 7073-7082.
21. D. H. Jo, Y. M. Chiou, L. Que Jr., *Inorg*. *Chem*. **2001**, *40*, 3181-3190.
22. F. P. Dwyer, J. W. Hogarth, R. N. Rhoda, *Inorg*. *Synth*. **1957**, *5*, 206.
23. Z. Codolà, I. Gamba, F. A. Parés, C. Casadevall, M. Clémancey, J. M. Latour, J. M. Luis, J. L. Fillol, M. Costas, *J*. *Am*. *Chem*. *Soc*. **2019**, *141*, 323-333.
24. Y. Liu, S.-M. Ng, W. W. Y. Lam, S.-M. Yiu, T.-C. Lau, *Angew*. *Chem*. *Int*. *Ed*. **2016**, *55*, 288-291.
25. Z. Y. Li, J. S. Huang, M. C. W. Chan, K. K. Cheung, C. M. Che, *Inorg*. *Chem*. **1997**, *36*, 3064-3071.
26. A. Patel, A. Ludi, H. B. Bürgi, A. Raselli, P. Bigler, *Inorg*. *Chem*. **1992**, *31*, 3405-3410.
27. J. P. C. Coverdale, I. R. Canelon, C. S. Cano, G. J. Clarkson, A. Habtemariam, M. Wills, P. J. Sadler, *Nat*. *Chem*. **2018**, *10*, 347-354.

Supporting Information for Chapter 1

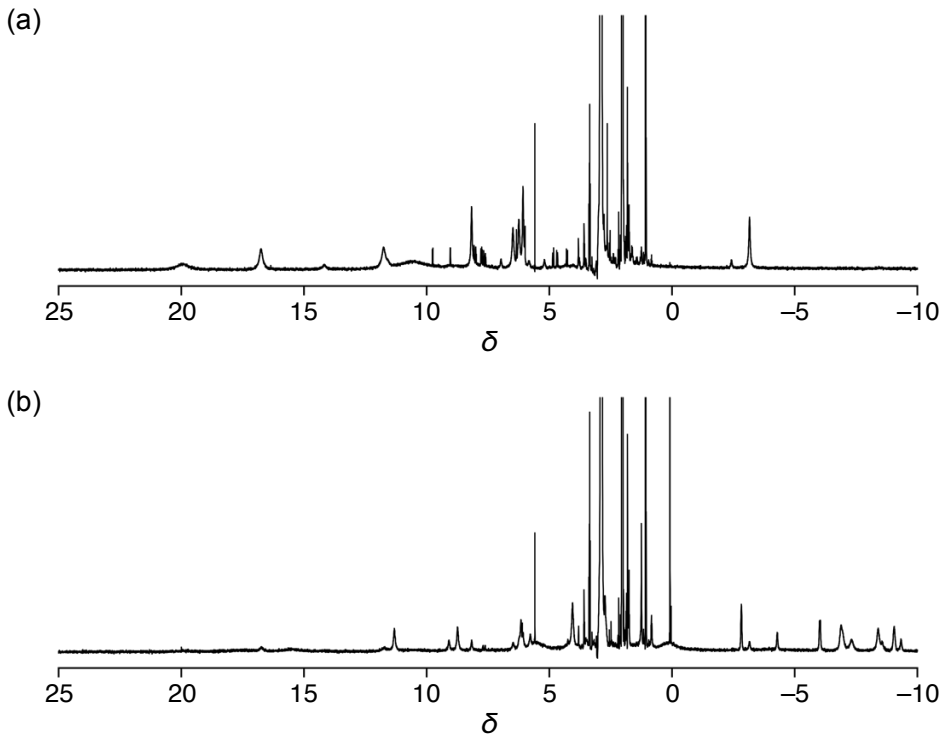

Figure 1-S1. ^{1}H NMR spectra of (a) **1** and (b) **2** in a range from –10 to 25 ppm.

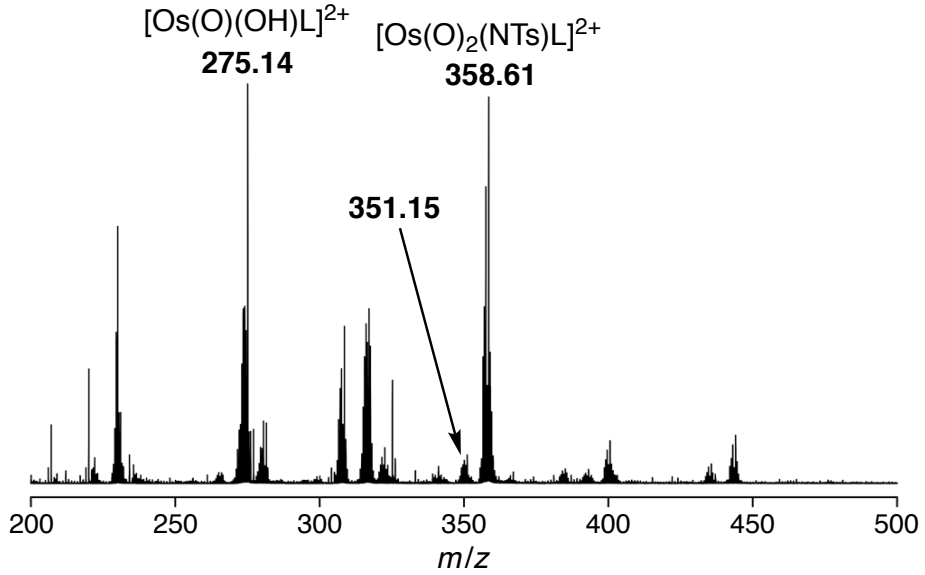

Figure 1-S2. ESI-mass spectrum of a reaction solution of **4** and chloramine-T in H_2O.

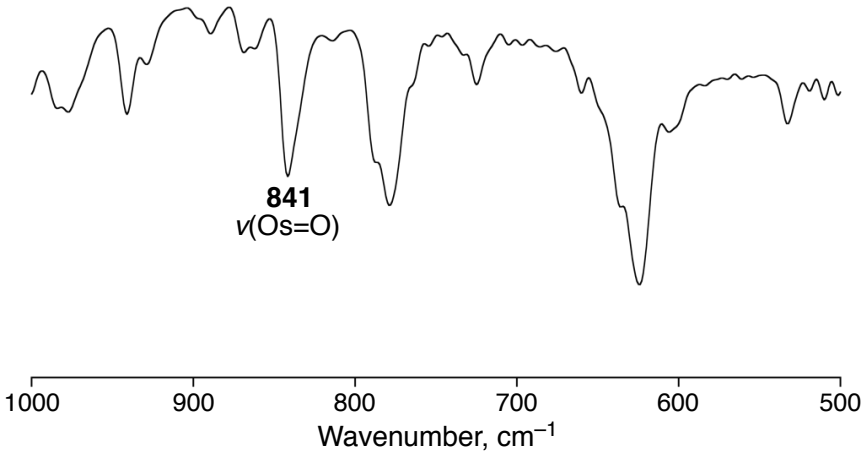

Figure 1-S3. FT-IR spectrum of an ^{18}O labeled **5**.

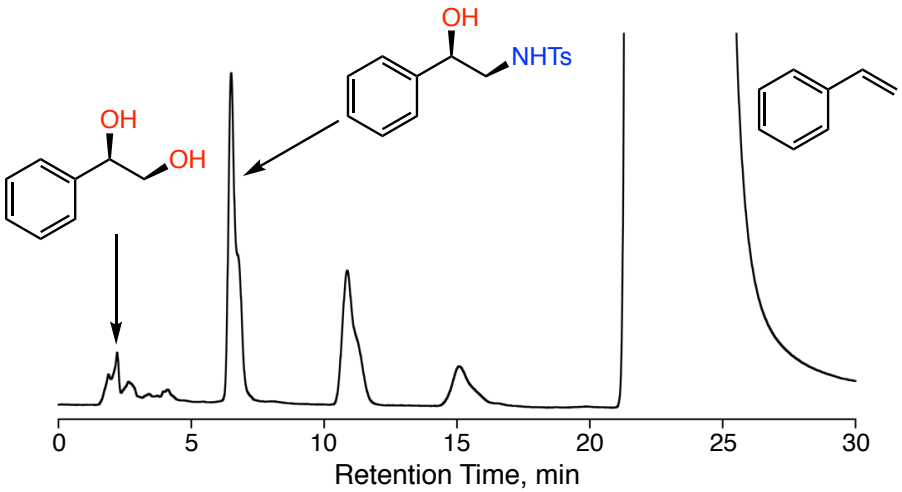

Figure 1-S4. HPLC chart after the reaction of complex **6** with styrene.

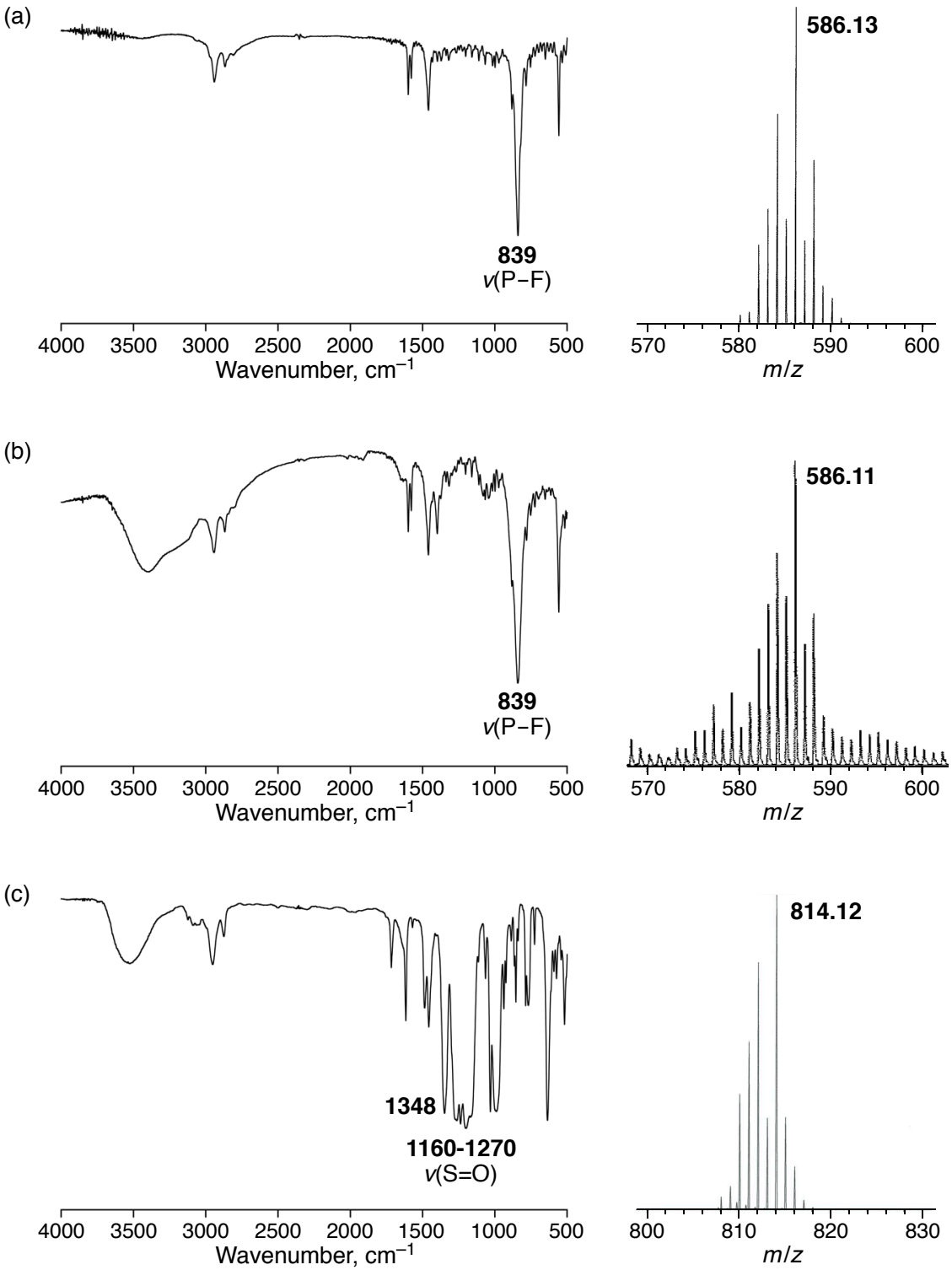

Figure 1-S5. FT-IR and ESI-mass spectra of (a) **1**, (b) **2**, (c) **3**, (d) **4**, and (e) **5**.

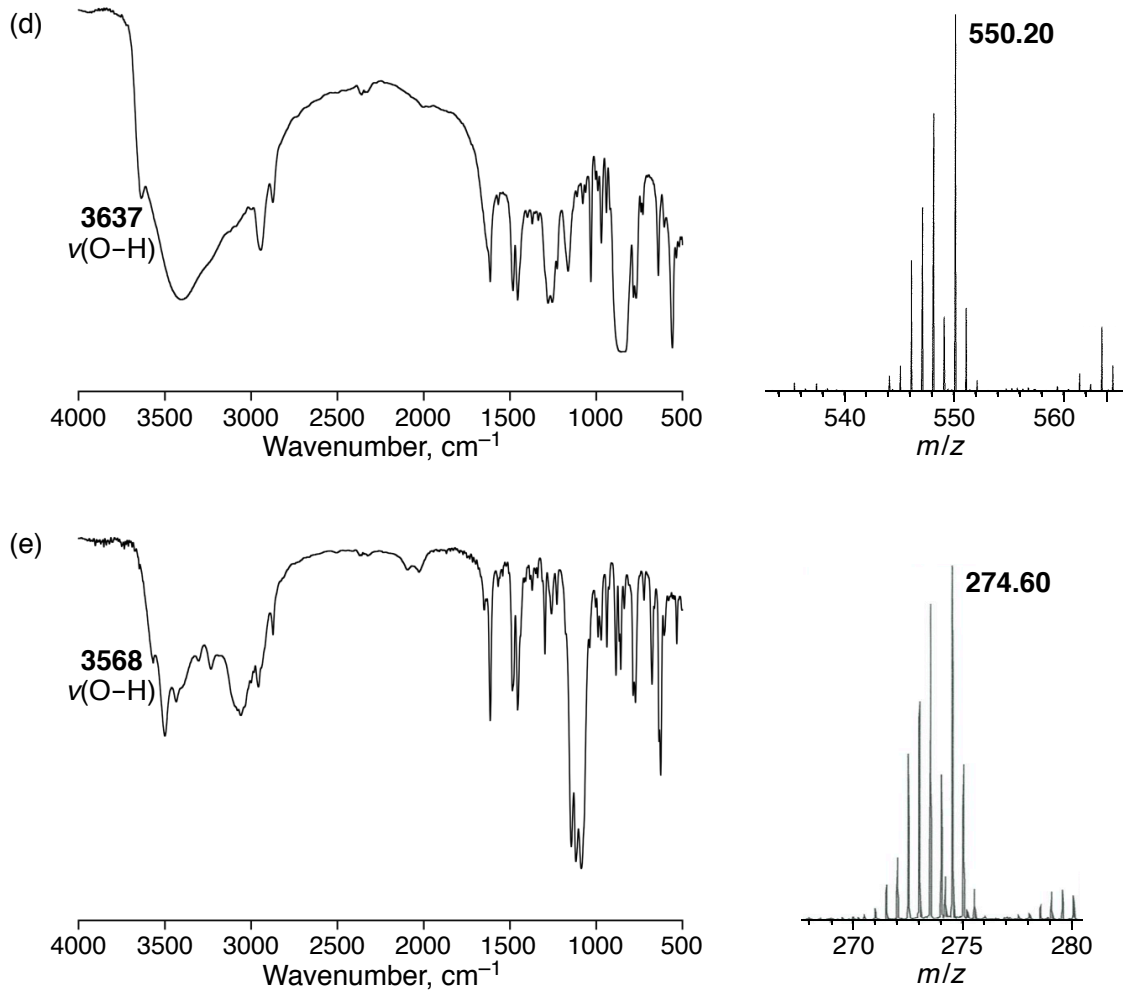

Figure 1-S5. FT-IR and ESI-mass spectra of (a) **1**, (b) **2**, (c) **3**, (d) **4**, and (e) **5** (continued).

Chapter 2

Alcohol-Oxidation by Halide-Adduct of OsO_4

Introduction

Osmium tetroxide (OsO_4) has long been known to catalyze the *cis*-dihydroxylation of alkenes, where addition of an amine or pyridine to the osmium center is demonstrated to enhance the reactivity of OsO_4 (Scheme 2-1(a)).[1-17] Mayer and co-workers also demonstrated that OsO_4 can oxidize simple alkanes including methane under aqueous alkaline conditions to give the corresponding alcohols together with the over-oxidation products such as the carboxylic acids and CO_2.[18, 19] In this case as well, coordination of an external ligand such as OH^- to the osmium center was proposed to enhance the oxidation reactivity (Scheme 2-1(b)). The osmium-hydroxide adduct has been also shown to oxidize H_2 molecule to generate $[Os^{VI}(O)_2(OH)_4]^{2-}$ (Scheme 2-1(c)).[20, 21] However, structural characterization of the hydroxide-adduct has yet to be accomplished.

Beside OsO_4, metal oxides (M_xO_y) of iron, manganese, and chromium have been employed in the oxidation of various organic substrates.[22-32] For instance, CrO_3 is used in alcohol-oxidation, known as Jones oxidation, which is insoluble in common organic solvents due to its polymeric chain structure.[33, 34] In this case, addition of coordinative chloride anion to CrO_3 giving chlorochromate ($[CrO_3(Cl)]^-$) enhances the reactivity in the alcohol oxidation (PCC oxidation) by improving the solubility of CrO_3.[35, 36] Thus, it is highly desired to investigate the effects of external ligands on the structure, physicochemical properties, and reactivity of the metal oxides to develop more efficient oxidation reagents.

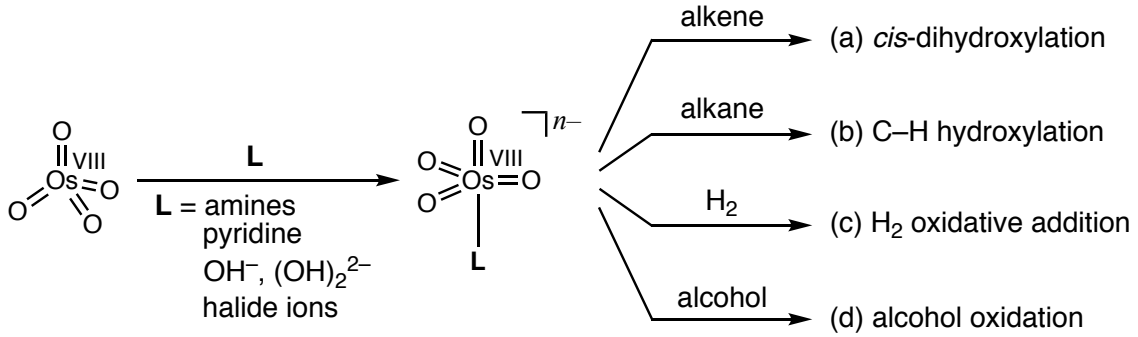

Scheme 2-1. Oxidation reaction with ligand-bound OsO_4 species ($[OsO_4(L)]^{n-}$) (n = 0, 1, 2).

In Chapter 2, the author examined the reactions of OsO_4 and the series of halide ions ($X^- = I^-$, Br^-, Cl^-, and F^-) and investigated the structure and physicochemical properties of the generated halide-adducts, $[OsO_4(X)]^-$ (**1**^{X}, X = Br^-, Cl^-, and F^-). Oxidation ability of **1**^{X} is also explored in detail in the alcohol-oxidation reaction (Scheme 2-1(d)).

Experimental Section

General. The reagents and the solvents used in this study were commercial products of the highest available purity and further purified by the standard methods, if necessary.[37] ^{1}H NMR spectra were recorded on a JEOL ECP400 or a JEOL ECS400 spectrometer. FT-IR spectra were recorded with a Jasco FT/IR-4100 spectrometer. Elemental analysis was carried out with a Yanaco CHN-Corder MT-5. UV-vis spectra were recorded on a Hewlett Packard 8453 photo diode array spectrometer or a Jasco V-650 spectrometer. Electrochemical measurements were performed with a Hokuto Denko HZ-7000. A set of carbon working electrode, an Ag/Ag^+ reference electrode, and a platinum counter electrode was employed in these experiments. After the CV measurements, ferrocene was added to the sample solution as an internal standard and the redox potential of Fc/Fc^+ was set as 0.0 V. A 0.1 M acetonitrile stock solution of OsO_4 was prepared by dissolving 1.0 g of OsO_4 (3.93 mmol) in 39.3 mL of acetonitrile and stored in a bottle with a screw cap. The reaction mixture after benzyl alcohol oxidation was analyzed with a HPLC system of an EXTREMA series (JASCO Co.) equipped with a reverse-phase column (column: Nacalai Co. COSMOSIL 5C18-AR-II, eluent: CH_3CN : H_2O = 4 : 6). Deuterated benzyl alcohol ($PhCD_2OH$) was synthesized by a reported method.[38]

Synthesis of $[Ph_4P][OsO_4(Br)]$ (1^{Br}). Ph_4PBr (83.8 mg, 0.20 mmol) was dissolved in a 2.0 mL of an acetonitrile stock solution containing 0.1 M OsO_4 (0.20 mmol), and the resultant solution was stirred for 15 min, during which color of the solution became violet. Diethyl ether was added to the resultant violet solution to give a violet powder, which was collected by filtration and dried in air. Yield: 83.6 mg (0.12 mmol, 62%). Single crystals suitable for X-ray crystallographic analysis were obtained by slow diffusion of diethyl ether into a dichloromethane solution containing the titled complex. UV-vis (acetonitrile): λ_{max} = 430 nm (ε = 960 M^{-1} cm^{-1}). FT-IR (KBr): 933 ($\nu_{(Os=O)asym}$) and 946 cm^{-1} ($\nu_{(Os=O)sym}$). Elemental analysis data do not match well with the calculated values due to gradual sublimination of OsO_4 from the solid sample of **1**^{Br}.

Synthesis of [Ph_4P][OsO_4(Cl)] ($\mathbf{1^{Cl}}$). This compound was prepared according to a similar procedure described above for the synthesis of $\mathbf{1^{Br}}$ by using Ph_4PCl (75.0 mg, 0.20 mmol) instead of Ph_4PBr. The generated orange powder was collected by filtration and dried in air. Yield: 88.0 mg (0.14 mmol, 71%). Single crystals suitable for X-ray crystallographic analysis were obtained by slow diffusion of diethyl ether into a dichloromethane solution containing the titled complex. Anal. Calcd. for $\mathbf{1^{Cl}}\cdot 0.2Et_2O$ ($C_{24.8}H_{22}ClO_{4.2}OsP$): C, 46.26; H, 3.44%. Found: C, 46.40; H, 3.44%. UV-vis (acetonitrile): λ_{max} = 385 nm (ε = 700 M^{-1} cm^{-1}). FT-IR (KBr): 882 ($\nu_{(Os=O)asym}$) and 909 cm^{-1} ($\nu_{(Os=O)sym}$).

Synthesis of [Ph_4P][OsO_4(F)] ($\mathbf{1^F}$). [Bu_4N][OsO_4(F)] was generated in situ by the reaction of OsO_4 stock solution (4.0 mL, 0.40 mmol) with 1.0 M THF solution of Bu_4NF (0.40 mL, 0.40 mmol). Ph_4PBr (167.6 mg, 0.40 mmol) was then added to the resulting solution to give yellow powder, which was collected by filtration and dried in air. Yield: 192.2 mg (0.31 mmol, 78%). Anal. Calcd. for $\mathbf{1^F}$ ($C_{24}H_{20}FPO_4Os$): C, 47.05; H, 3.29%. Found: C, 47.03; H, 3.22%. UV-vis (acetonitrile): λ_{max} = 320 nm (ε = 3300 M^{-1} cm^{-1}), 385 (680). FT-IR (KBr): 878 ($\nu_{(Os=O)asym}$) and 900 cm^{-1} ($\nu_{(Os=O)sym}$).

Synthesis of [Ph_4P][$Os^{VII}O_4$]. This compound was prepared according to the procedure described for the synthesis of [Ph_4As][$Os^{VII}O_4$].[39] OsO_4 (1.0 g, 3.93 mmol) was dissolved in 10 mL of CH_2Cl_2 at 0 °C, to which a CH_2Cl_2 solution (15 mL) of Ph_4PI (2.75 g, 5.90 mmol) was added. The color of the solution changed to blue at first and then gradually to greenish brown. Deep green powder was precipitated by the addition of 10 mL of CCl_4, which was collected by filtration and washed with CH_2Cl_2 and dried in vacuo. Yield; 1.43 g (2.41 mmol, 61%). Anal. Calcd. for [Ph_4P][$Os^{VII}O_4$] ($C_{24}H_{20}PO_4Os$): C, 48.56; H, 3.40%. Found: C, 48.29; H, 3.34%. UV-vis (acetonitrile): λ_{max} = 298 nm (ε = 1600 M^{-1} cm^{-1}), 478 (44), 575 (40), 663 (32), 694 (35). FT-IR (KBr): 838 ($\nu_{(Os=O)asym}$) and 855 cm^{-1} ($\nu_{(Os=O)sym}$).

Determination of Formation Constant (K_f^X) of $\mathbf{1^X}$. The titration of OsO_4 by $Bu_4N^+X^-$ (X = Br^-, Cl^-, and F^-) was carried out in acetonitrile at 30 °C using a 1.0 cm path length UV-vis cell closed with a septum cap. Concentrations of the reagents are described in the figure captions of Figure 2-1, 2-S1, and 2-S2. For $\mathbf{1^F}$, a commercially available 1.0 M THF solution of Bu_4NF was used. The formation constants (K_f^X) of $\mathbf{1^{Cl}}$ and $\mathbf{1^{Br}}$ were

calculated from a double-reciprocal plot of ΔAbs^{-1} against $[Bu_4NX]^{-1}$ following the Benesi-Hildebrand equation (eq. 1).[40, 41] The K_f^F value of **1^F** was too large to be determined accurately.

$$\frac{1}{\Delta A} = \frac{1}{[Os]_T \Delta\varepsilon K_f^X [Bu_4NX]} + \frac{1}{[Os]_T \Delta\varepsilon} \quad \text{— (1)}$$

Product Analysis of the Oxidation of Benzyl Alcohol by 1^F. The concentration of **1^F** was adjusted to 0.80 mM by adding 0.80 mM of Bu_4NF to 1.0 mM of OsO_4 in CH_3CN. Then, benzyl alcohol (1.0 mM) was added to the solution at –40 °C under N_2 atmosphere. After the reaction, anisole was added into the resulting solution as an internal standard. The reaction mixture was analyzed by HPLC to determine the products, and their yields are calculated by comparing the peak area of the products to those of the authentic samples using calibration curves.

Kinetic Studies on the Benzyl Alcohol Oxidation by 1^F. All the reactions of **1^F** (1.0 mM) with benzyl alcohol derivatives (25-300 mM) were carried out in a 1.0 cm path length UV-vis cell closed with a septum cap. After addition of Bu_4NF (1.0 mM) into an acetonitrile solution of OsO_4 (1.0 mM), reactions were started by adding benzyl alcohol into the solution through a septum cap with using a microsyringe at –40 °C under N_2 atmosphere. The reactions were followed by monitoring increase of the absorption band around 700 nm due to an Os^{VI} species.

X-ray Crystallographic Analysis. The single crystal was mounted on a loop with a mineral oil, and all X-ray data were collected at –170 °C on a Rigaku R-AXIS RAPID diffractometer using filtered Mo-Kα radiation. The structures were solved by direct method (SIR 2011) and expanded using Fourier techniques. The non-hydrogen atoms were refined anisotropically by full-matrix least-squares on F^2. The hydrogen atoms were attached at idealized positions on carbon atoms and were not refined. All of the crystallographic calculations were performed using the Crystal Structure software package of Molecular Structure Corp. [Crystal Structure, Crystal Structure Analysis Package, version 3.8.1, Molecular Structure Corp. and Rigaku Corp. (2005)]. Crystallographic parameters are summarized in Table 2-1.

Computational Details. The density-functional-theory (DFT) calculations were

performed with the Gaussian 16 program package (Rev. C01).[42] All geometry optimizations were carried out with the B3LYP functional.[43-45] The SDD (Stuttgart/Dresden pseudopotentials) basis set[46, 47] for Os and the 6-311G** basis set[48] for the other atoms were employed. After geometry optimizations, vibrational analyses were calculated for all reaction species to confirm stable and transition structures.

Table 2-1. Crystallographic data for $[Ph_4P][OsO_4(Br)]$ ($\mathbf{1^{Br}}$) and $[Ph_4P][OsO_4(Cl)]$ ($\mathbf{1^{Cl}}$).

	$\mathbf{1^{Br}}$	$\mathbf{1^{Cl}}$
Formula	$C_{24}H_{20}BrO_4OsP$	$C_{24}H_{20}ClO_4OsP$
Formula weight	673.50	629.02
Crystal system	Orthorhombic	Tetragonal
Space group	*P*bca (#61)	$P\bar{4}$ (#81)
a, Å	14.0185(9)	24.3328(19)
b, Å	17.5451(11)	24.3328(19)
c, Å	18.4734(11)	7.4845(3)
α, deg	90.000	90.000
β, deg	90.000	90.000
γ, deg	90.000	90.000
V, Å^3	4543.6(5)	4431.5(7)
Z	8	8
D_{calcd}, g/cm^{-3}	1.969	1.886
F(000)	2576.00	2432.00
μ(Mo-Kα), cm^{-1}	74.72	59.77
Crystal size, mm	0.30 × 0.10 × 0.10	0.20 × 0.10 × 0.10
T, K	103	115
$2\theta_{max}$, deg	54.9	55.0
No. of reflns obsd	5178	10075
No. of params	300	559
R_1[a]	0.0221	0.0357
wR_2[b]	0.0734	0.0843
GOF	0.914	1.047

[a] $R_1 = \Sigma(|F_o| - |F_c|)/\Sigma|F_o|$

[b] $wR_2 = [\Sigma(w(F_o^2 - F_c^2)^2)/\Sigma w(F_o^2)^2]^{1/2}$

Results and Discussion

Reaction of OsO_4 with Halide Ions.

The reactions of OsO_4 with the series of halide ions, I^-, Br^-, Cl^-, and F^-, were first examined. In Figure 2-1(a) is shown the UV-vis spectral changes observed upon addition of Bu_4NF to an acetonitrile solution of OsO_4 (0.5 mM) at 30 °C, where an intense absorption band at 320 nm and a shoulder band at 385 nm gradually appeared. The spectral change completed when a stoichiometric amount of Bu_4NF (0.5 mM) was added (Figure 2-1(a), inset), indicating that OsO_4 reacted with F^- in a 1 : 1 ratio to form $[Bu_4N][OsO_4(F)]$ (**1**^{F}). The formation constant K_f^F was too large to be determined accurately by the titration experiment. On the other hand, addition of Bu_4NCl to an

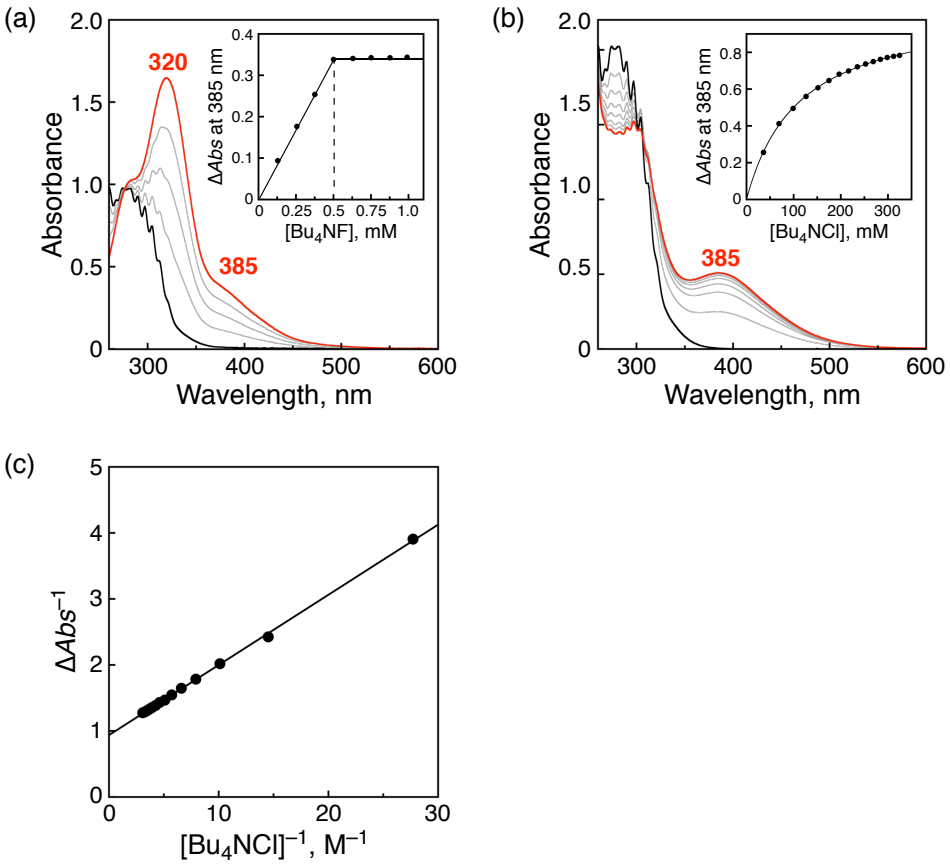

Figure 2-1. (a) UV-vis spectral changes observed in the titration of OsO_4 (0.5 mM) by Bu_4NF in acetonitrile at 30 °C. Inset: Plot of ΔAbs at 385 nm against $[Bu_4NF]$. (b) UV-vis spectral changes observed in the titration of OsO_4 (1.0 mM) by Bu_4NCl in acetonitrile at 30 °C. Inset: Plot of ΔAbs at 385 nm against $[Bu_4NCl]$. (c) Plot of ΔAbs^{-1} against $[Bu_4NCl]^{-1}$.

acetonitrile solution of OsO_4 (1.0 mM) gave a saturation curve (Figure 2-1(b), inset), which can be analyzed by the Benesi-Hildebrand equation (1) (see Experimental Section).[40, 41] Thus, the double reciprocal plot of ΔAbs^{-1} against $[Bu_4NCl]^{-1}$ gave a linear line as shown in Figure 2-1(c), from which the formation constant K_f^{Cl} of $\mathbf{1^{Cl}}$ was calculated to be 8.5 M^{-1}. The formation constant K_f^{Br} for $\mathbf{1^{Br}}$ was also determined as 0.69 M^{-1} by a similar manner (Figure 2-S1). The spectral changes for the reaction of OsO_4 with Bu_4NI at 30 °C is shown in Figure 2-S2(a). The intense absorption band at 361 nm is assignable to I_3^- and the characteristic absorption bands above 550 nm are similar to those of the authentic sample of $[Os^{VII}O_4]^-$ shown in Figure 2-S3.[39] These spectral data clearly indicated that electron transfer took place from I^- to OsO_4 to produce I• and $[Os^{VII}O_4]^-$, the former of which underwent radical coupling to yield I_2 that is further converted to I_3^- by the reaction with I^- existing in the solution. In fact, a transient spectrum exhibiting an absorption band at 560 nm probably due to a $[OsO_4(I)]^-$ species ($\mathbf{1^I}$) was observed when the reaction was carried out at –40 °C, which was afterwards converted to the spectrum of the mixture of $[Os^{VII}O_4]^-$ and I_3^- (Figure 2-S2(b)). The Os–I bond in $\mathbf{1^I}$ may be easily cleaved homolytically to give I• and $[Os^{VII}O_4]^-$. The yield of I_3^- was determined as 48% based on OsO_4 by using the ε value of I_3^-,[49] being consistent with the reaction consequence mentioned above (theoretical yield of I_3^- is 50%). Apparently, the formation constant K_f^X increases with increasing the pK_a value of the conjugate acid (HX), thus basicity of X^- controls the bond strength and stability of $\mathbf{1^X}$ (Table 2-S1).

Crystal Structures and Spectroscopic Characteristics of $[OsO_4(X)]^-$ ($\mathbf{1^X}$).

The halide adducts of Os^{VIII}, $[Ph_4P][OsO_4(Br)]$ ($\mathbf{1^{Br}}$), $[Ph_4P][OsO_4(Cl)]$ ($\mathbf{1^{Cl}}$), and $[Ph_4P][OsO_4(F)]$ ($\mathbf{1^F}$) were obtained as powder samples from the preparative scale reactions in acetonitrile (see Experimental Section). However, the iodide-adduct complex $[Bu_4N][OsO_4(I)]$ ($\mathbf{1^I}$) could not be isolated because of its instability even at –40 °C (Figure 2-S2).

The isolated halide-adducts exhibited two strong IR bands ascribable to asymmetric ($\nu_{(Os=O)asym}$) and symmetric ($\nu_{(Os=O)sym}$) Os=O stretching vibrations at 933 and 946 cm^{-1} for $\mathbf{1^{Br}}$, at 882 and 909 cm^{-1} for $\mathbf{1^{Cl}}$, and at 878 and 900 cm^{-1} for $\mathbf{1^F}$ in the solid state (KBr) (Figure 2-S4). These values are lower than those of OsO_4 itself (954 and 965 cm^{-1}),[50]

reflecting weakened Os=O bonds by electron donation by the halide anion and/or decrement of the coordination number from 4 to 5. Furthermore, the $\nu_{Os=O}$ values of $\mathbf{1}^{Br}$, $\mathbf{1}^{Cl}$, and $\mathbf{1}^{F}$ differ significantly due to different degree of Os–X bonding interaction as reflecting in the different Os–X bond lengths in the crystal structures as discussed below.

The crystal structures of $\mathbf{1}^{Br}$ and $\mathbf{1}^{Cl}$ determined in this study are shown in Figure 2-2. Despite our great efforts, single crystals of $\mathbf{1}^{F}$ suitable for X-ray crystallographic analysis could not be obtained. The crystal structures of Cl^- and F^- adduct complexes, $[Ph_4P][OsO_4(Cl)]\cdot CH_2Cl_2$ ($\mathbf{1}^{Cl'}$) and $[Me_4N][OsO_4(F)]$ ($\mathbf{1}^{F'}$) have already been reported in the literatures, which are shown in Figure 2-S5 and Figure 2-S6, respectively.[51, 52]

Interestingly, $\mathbf{1}^{Br}$ has an osmium center with a slightly distorted tetrahedral geometry with four oxido ligands, where the Br^- is weakly interacting with the osmium center mainly *via* electrostatic interaction. Namely, the Os(1)–Br(1) distance of 3.4653(3) Å is significantly longer than the sum of ionic radii of Os and Br atoms (2.35 Å),[53] where O(1), Os(1), and Br(1) are lined up in a straight line; O(1)–Os(1)–Br(1) angle is

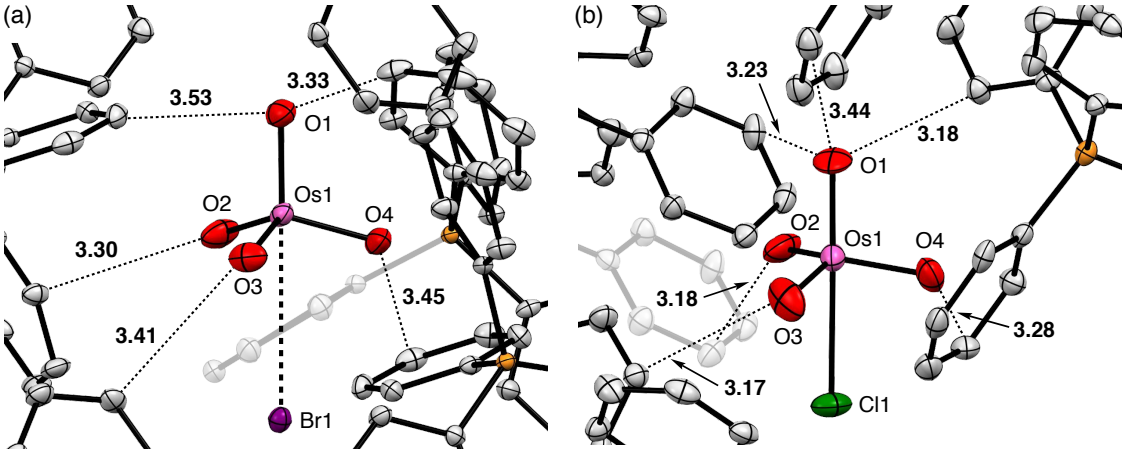

Figure 2-2. X-ray crystal structures of complex (a) $\mathbf{1}^{Br}$ and (b) $\mathbf{1}^{Cl}$. Hydrogen atoms have been omitted for clarity. The number between atoms represents the bond distances (Å). The Selected bond distances (Å) and angles (°): For $\mathbf{1}^{Br}$, Os(1)–Br(1), 3.4653(3); Os(1)–O(1), 1.713(2); Os(1)–O(2), 1.701(2); Os(1)–O(3), 1.707(2); Os(1)–O(4), 1.700(2); Os(1)–plane(O2O3O4), 0.50; O(1)–Os(1)–Br(1), 178.87; O(1)–Os(1)–O(2), 107.17(10); O(2)–Os(1)–O(3), 111.91(11); O(3)–Os(1)–O(4), 112.11(12). For $\mathbf{1}^{Cl}$, Os(1)–Cl(1), 2.644(2); Os(1)–O(1), 1.733(7); Os(1)–O(2), 1.717(5); Os(1)–O(3), 1.705(5); Os(1)–O(4), 1.713(5); Os(1)–plane (O2O3O4), 0.30; O(1)–Os(1)–Cl(1), 179.2(2); O(1)–Os(1)–O(2), 99.5(3); O(2)–Os(1)–O(3), 118.5(3); O(3)–Os(1)–O(4), 116.2(3).

178.87(7)°. As shown in Figure 2-2, the OsO_4 core is surrounded by the neighboring counter cations Ph_4P^+, where distances between the oxygen atoms of $\mathbf{1^{Br}}$ and the carbon atoms of the phenyl groups of Ph_4P^+ are 3.3-3.5 Å. With respect to the bond angles, the bond angles of O(2)–Os(1)–O(3), O(2)–Os(1)–O(4), and O(3)–Os(1)–O(4) are very close each other (111.9(1), 111.7(1), and 112.1(1)°, respectively) and the bond angles of O(1)–Os(1)–O(2), O(1)–Os(1)–O(3), and O(1)–Os(1)–O(4) are also very close each other (107.2(1), 106.7(1), and 106.9(1)°, respectively). Moreover, the Os(1)–O(1) bond length (1.713(2) Å) is close to that of OsO_4 itself (1.712 Å)[54] and the distance between Os(1) and a basal plane consisting of O(2), O(3), and (4) atoms is 0.50 Å, which is also close to that in OsO_4 itself (0.553 Å). Thus, the observed rather small red-shift of $\nu_{Os=O}$ in $\mathbf{1^{Br}}$ could be ascribed to the electronic structural perturbation of the Os=O bonds (making $Os^{\delta+}$–$O^{\delta-}$) by the electrostatic interaction with Br^-.

In the case of $\mathbf{1^{Cl}}$, interaction of Cl^- with Os center is stronger than that of Br^- with Os in $\mathbf{1^{Br}}$. In the packing diagram of $\mathbf{1^{Cl}}$, the same type of interaction exists between OsO_4 and Ph_4P^+ (interaction between the oxygen atoms and the carbon atoms of the counter cation) as shown in $\mathbf{1^{Br}}$ (Figure 2-2). Namely, $\mathbf{1^{Cl}}$ takes a slightly distorted trigonal bipyramid structure, where a Os(1)–Cl(1) bond length of 2.644(2) Å is slightly longer than the sum of ionic radii of Os and Cl atoms (2.20 Å).[53] The distance between Os(1) and a basal plane consisting of O(2), O(3), and O(4) atoms is 0.30 Å, which is smaller than that in $\mathbf{1^{Br}}$. The crystal structure of $\mathbf{1^{Cl'}}$ ($[Ph_4P][OsO_4(Cl)\cdot CH_2Cl_2]$) was reported by K. Dehnicke and co-workers as shown in Figure 2-S5,[51] where hydrogen bonding interaction between the Cl(1) and the two solvent molecules (CH_2Cl_2) makes the trigonal bipyramid geometry more distorted compared with that in $\mathbf{1^{Cl}}$ (Figure 2-2). The crystal structure of $\mathbf{1^{F'}}$ ($[Me_4N][OsO_4(F)]$) shown in Figure 2-S6, determined by J. Schrobilgen and co-workers,[52] also exhibits a distorted trigonal bipyramid geometry due to multiple hydrogen bonding interactions between both the fluorine atom and the oxido ligands with the counter cations $N(CH_3)_4^+$, Figure 2-S6). Even though $\mathbf{1^{F'}}$ has a distorted trigonal bipyramid structure, the distance between Os(1) and a basal plane consisting of O(2), O(3), and (4) atoms is the smallest as 0.28 Å among the three halide complexes, reflecting the strongest interaction between F^- and Os center. Although crystal structure of $\mathbf{1^F}$ has yet to be determined, the elemental analysis data indicated that $\mathbf{1^F}$ does not contain any solvent molecules in the sample (see Experimental Section).

Furthermore, the counter cation of $\mathbf{1^F}$ is Ph_4P^+, which is different from that in $\mathbf{1^{F'}}$ ($N(CH_3)_4^+$). Thus, there might be no interaction of the fluoride anion with solvent molecule and/or counter cation such as found in $\mathbf{1^{Cl'}}$ and $\mathbf{1^{F'}}$ (Figure 2-S5 and Figure 2-S6). If so, the structure of $\mathbf{1^F}$ might be a symmetric trigonal bipyramidal structure having C_{3v} axis (O–Os–F) like in $\mathbf{1^{Cl}}$ (Figure 2-2). Comparison of distances between Os(1) atoms and the basal planes (0.55 for OsO_4; 0.50 for $\mathbf{1^{Br}}$; 0.30 for $\mathbf{1^{Cl}}$; 0.28 Å for $\mathbf{1^{F'}}$) reveals that more basic anion causes more significantly structural change from tetrahedron to trigonal bipyramid. These interaction between halide anion and OsO_4 rationalized the presence of σ-hole interaction in the halide adducts ($\mathbf{1^{Br}}$ and $\mathbf{1^{Cl}}$) as reported in OsO_4-pyridine adduct.[55]

Regarding to the Os–O distances, the Os–O_{basal} distances of $\mathbf{1^{Br}}$ (Os(1)–O(2): 1.701(2), Os(1)–O(3): 1.707(2), and Os(1)–O(4): 1.700(2) Å) are not so different from the Os=O bond length of the original OsO_4 (1.712 Å for OsO_4,[54] the four Os–O bonds are equivalent), but those of $\mathbf{1^{Cl}}$ are somewhat elongated compared to that in OsO_4 (Os(1)–O(2): 1.717(5), Os(1)–O(3): 1.705(5), and Os(1)–O(4): 1.713(5) Å in $\mathbf{1^{Cl}}$), reflecting the stronger interaction of Os–Cl compared to Os–Br. The different degree of Os–X interaction is more pronounce in the Os–O_{axial} distances (Os(1)–O(1): 1.713(2) Å in $\mathbf{1^{Br}}$ and Os(1)–O(1): 1.733(7) Å in $\mathbf{1^{Cl}}$). Apparently, the observed $\nu_{Os=O}$ shifts in the FT-IR spectra can be ascribed to the elongation of the Os–O bonds.

Electrochemical Property.

Effects of halide-interaction with OsO_4 were also examined electrochemically using cyclic voltammetry (CV). OsO_4 itself exhibited a reversible redox couple assignable to the Os(VIII)/Os(VII) redox process at $E_{1/2}$ = –0.32 V (vs. Fc/Fc^+, E_{pa} = –0.28 V, E_{pc} = –0.35 V, black line in Figure 2-3). Addition of one equivalent of Bu_4NF (1.0 mM) to the OsO_4 solution gave a quasi-reversible redox wave in more negative region (red line), from which the redox potential of complex $\mathbf{1^F}$ ($E_{1/2}$) was determined as –0.42 V (vs. Fc/Fc^+, E_{pa} = –0.37 V, E_{pc} = –0.47 V). $\mathbf{1^{Cl}}$ and $\mathbf{1^{Br}}$ also gave quasi-reversible redox couples, when CVs were measured in the presence of a large excess of the counter anions to ensure the formation of the halide adducts (Figure 2-S7), from which apparent $E_{1/2}$ values were determined as –0.35 and –0.29 V vs. Fc/Fc^+, respectively. The redox potential of $\mathbf{1^{Cl}}$ also shifted to the negative direction compared to that of OsO_4. However,

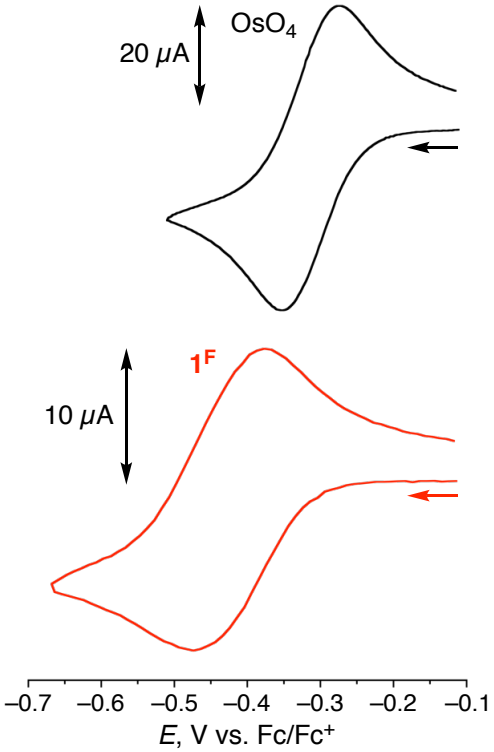

Figure 2-3. Cyclic voltammograms of OsO_4 (1.0 mM, black line) and that in the presence of an equimolar amount of Bu_4NF (1.0 mM, red line) in CH_3CN containing 0.1 M of Bu_4NPF_6 as the electrolyte at 25 °C.

its negative shift value was smaller than that of $\mathbf{1}^{\mathbf{F}}$. Thus, the stronger coordinative interaction of the halide anion makes the Os center harder to be reduced. In this respect, the positive shift of $E_{1/2}$ of $\mathbf{1}^{\mathbf{Br}}$ seems to be a little strange. However, such a positive shift of $E_{1/2}$ is understandable, if the electrostatic interaction between the oxido groups of $\mathbf{1}^{\mathbf{Br}}$ and the $^{n}Bu_4N^{+}$ cations of the supporting electrolyte ($^{n}Bu_4NPF_6$ existing in the solution in a large excess) is more predominant compared to the weak coordinative interaction between the Os center and Br^{-}. Such an electrostatic interaction causes an electronic structural perturbation of the Os core like $Os^{\delta+}$–$O^{\delta-}$, resulting a positive shift of $E_{1/2}$ of $\mathbf{1}^{\mathbf{Br}}$. In the case of $\mathbf{1}^{\mathbf{Cl}}$, on the other hand, the stronger coordinative interaction between the Os center and Cl^{-} ($K_f^{Cl} = 8.5\ M^{-1}$), compared to that between the Os center and Br^{-} ($K_f^{Br} = 0.69\ M^{-1}$), becomes more important, resulting the negative shift of $E_{1/2}$ of $\mathbf{1}^{\mathbf{Cl}}$.

Oxidation of Benzyl alcohol by $\mathbf{1}^{\mathbf{F}}$.

Since the K_f^X values of $\mathbf{1}^{\mathbf{Br}}$ and $\mathbf{1}^{\mathbf{Cl}}$ are too small (Table 2-S1) to generate the corresponding halide adducts quantitatively in solution, the oxidation ability of $\mathbf{1}^{\mathbf{X}}$ (0.8

mM) was evaluated using $\mathbf{1^F}$ in the oxidation of benzyl alcohol (1.0 mM) in acetonitrile at –40 °C. Although OsO_4 itself can oxidize benzyl alcohol to benzaldehyde after 10 min in a 6% yield,[56, 57] the yield of oxidation product increased significantly to 36% when $\mathbf{1^F}$ was used instead of OsO_4. Such an enhancement of oxidation ability of OsO_4 was also observed in alkene *cis*-dihydroxylation with OsO_4-pyridine adducts.[17] These phenomena are notable, since the adduct formation causes the decrease of reduction potential, thus decrease of the electron-transfer oxidation ability of OsO_4. Then, the oxidation of benzyl alcohol by $\mathbf{1^F}$ was investigated kinetically in order to get insights into the mechanism for the enhancement of oxidation ability.

In Figure 2-4(a) is shown the spectral change of the reaction at –40 °C, where the shoulder band around 420 nm due to $\mathbf{1^F}$ decreased with concomitant increase of a new absorption band at 700 nm. Appearance of the band around 700 nm suggested generation of an Os^{VI} species as discussed below (Scheme 2-2).[58] The kinetic trace based on the absorption changes at 700 nm consisted of two phases (Figure 2-4(a), inset). In the first phase (0-1200 sec), the absorption band at 700 nm appeared following first-order kinetics, but after that, the band around 700 nm further grown up to generate an Os^{VII} species (Figure 2-S8), which was similar to that of $[Os^{VII}O_4]^-$ (Figure 2-S3). The Os^{VII} species can be generated by the comproportionation reaction between an Os^{VI} species and remained Os^{VIII} species as also discussed below.[59]

Then, the reactions were followed by monitoring the absorption change at the first phase reaction. The pseudo-first-order rate constants (k_{obs}) of the reactions in the first phase were obtained based on the time course of absorption changes using non-linear curve fitting using a first-order kinetic equation of $[Os]_t = [Os]_0 \exp(-k_{obs}t)$. Then, the plot of k_{obs} against the concentration of benzyl alcohol gave a saturation curve (Figure 2-4(b)), suggesting a complex formation between $\mathbf{1^F}$ and benzyl alcohol ($\mathbf{1^F}$-$PhCH_2OH$) prior to alcohol oxidation process. In such a case, the reaction rate (k_{ox}) and the equilibrium constant (K_{add}) are expressed by equation (2), where $k_{obs} = k_{ox}K_{add}[PhCH_2OH]/(1 + K_{add}[PhCH_2OH])$.

$$v = k[\mathbf{1^F}\text{-}PhCH_2OH] = \frac{k_{ox}K_{add}[PhCH_2OH][Os]_T}{1 + K_{add}[PhCH_2OH]} = k_{obs}[Os]_T \quad \text{— (2)}$$

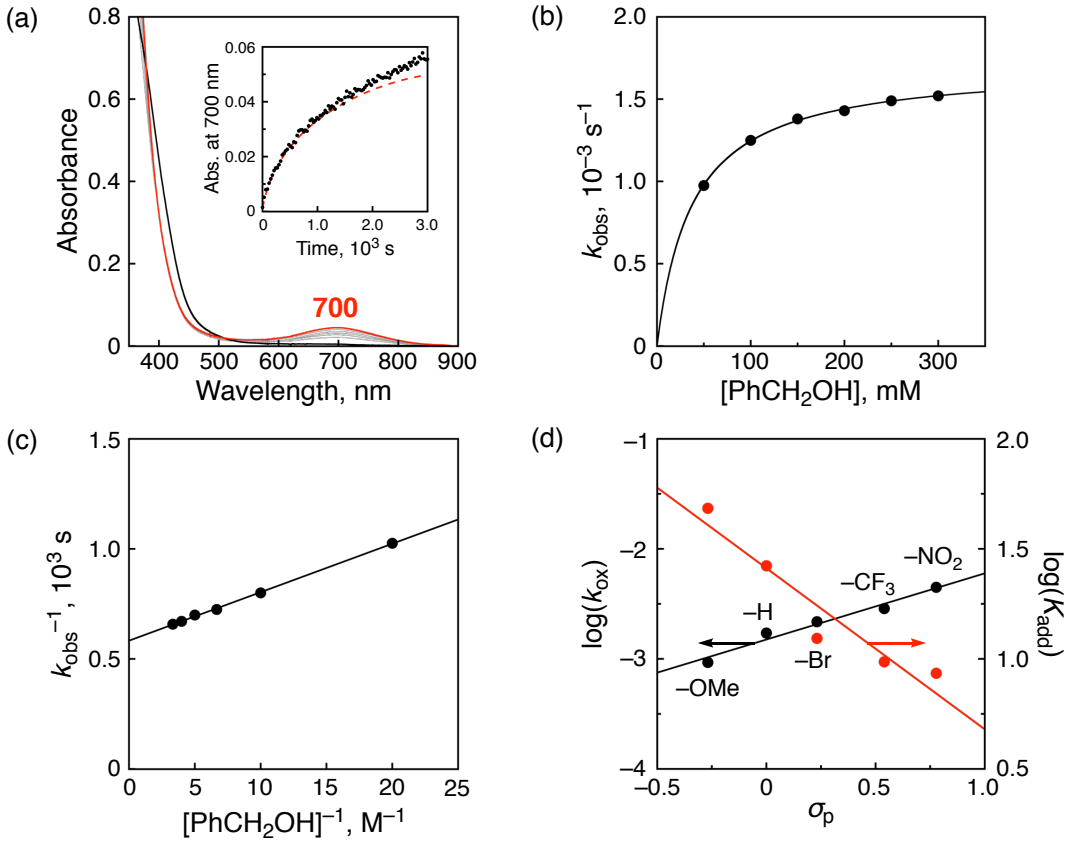

Figure 2-4. (a) UV-vis spectral changes measured until 1200 sec after addition of benzyl alcohol (200 mM) to $\mathbf{1}^{\mathbf{F}}$ (1.0 mM, black) in CH_3CN at –40 °C. Inset: The time course of the absorption changes at 700 mm. (b) The Plot of k_{obs} against $[PhCH_2OH]$. (c) A double-reciprocal plot of k_{obs}^{-1} against $[PhCH_2OH]^{-1}$ ($k_{obs}^{-1} = 22[PhCH_2OH]^{-1} + 583$). (d) A plot of $\log(k_{ox})$ and $\log(K_{add})$ against Hammett constant σ_p (ρ = 0.60 and –0.73, respectively)

Thus, k_{ox} and K_{add} were determined by the double reciprocal plot of k_{obs}^{-1} against $[PhCH_2OH]^{-1}$ ($k_{obs}^{-1} = (1 / k_{ox}K_{add})[PhCH_2OH]^{-1} + 1/k_{ox}$) (Figure 2-4(c)).[60] From the slope and the intercept of the linear line, equilibrium constant (K_{add}) and oxidation reaction rate (k_{ox}) were determined as 26.5 M^{-1} and 1.72 × 10^{-3} s^{-1}, respectively. To examine the electronic effect of *p*-substituent (Y) of the substrates, the reactions of $\mathbf{1}^{\mathbf{F}}$ with a series of *p*-substituted benzyl alcohol derivatives (*p*-Y-$C_6H_4CH_2OH$; Y = $–OCH_3$, –Br, $–CF_3$, and $–NO_2$) were examined (Figure 2-S9–S12). The K_{add} and k_{ox} values are summarized in Table 2-2.

Table 2-2. Kinetic parameters K_{add} and k_{ox} in the reaction of $\mathbf{1^F}$ with *p*-substituted benzyl alcohol.

–Y (*p*-substituent)	σ_p	K_{add}, M^{-1}	k_{ox}, s^{-1}
$–OCH_3$	–0.27	48.4	0.90×10^{-3}
–H	0	26.5	1.7×10^{-3}
–Br	0.23	12.4	2.2×10^{-3}
$–CF_3$	0.54	9.7	2.9×10^{-3}
$–NO_2$	0.78	8.6	4.5×10^{-3}

The plot of log(k_{ox}) against the Hammett constant σ_p gave a linear correlation with a positive ρ value of 0.60 (Figure 2-4(d), black line). Such a small positive ρ value indicates that $\mathbf{1^F}$ exhibits a nucleophilic radical character in the alcohol oxidation. Furthermore, by the reaction of $\mathbf{1^F}$ with a 1 : 1 mixture of benzyl alcohol ($PhCH_2OH$) and deuterated benzyl alcohol ($PhCD_2OH$) , a kinetic deuterium isotope effect (KIE) was determined as 4.5 from the integral ratio of benzaldehyde (PhCHO) and deuterated benzaldehyde (PhCDO) in the ^1H NMR spectrum (KIE; 1/(1.22 – 1.00) = 4.5, Scheme 2-S1 and Figure 2-S13). The KIE value could not be obtained by direct comparison of k_{ox}^H and k_{ox}^D, because the initial phase became obscure due to too slow reaction of $\mathbf{1^F}$ with $PhCD_2OH$. Furthermore, generation of hydrogen fluoride (HF) was confirmed by ^{19}F NMR after the reaction of $\mathbf{1^F}$ with benzyl alcohol (Figure 2-S14).[61, 62]

The plot of log(K_{add}) against the Hammett constant σ_p also exhibited a linear correlation with a negative ρ value of –0.73 (Figure 2-4(d), red line). This result was reasonable since the adduct formation constant K_{add} would increase as the electron donation by the *p*-substituent (Y) increases.

A possible reaction mechanism is shown in Scheme 2-2. First, benzyl alcohol ($PhCH_2OH$) adds to $\mathbf{1^F}$ to generate alcohol adduct intermediate **A**. The reversible alcohol adduct formation is consistent with the observed saturation kinetics shown in Figure 2-4(b). This equilibrium process is controlled by the electron donor ability of *p*-substituent of the substrate, which was supported by negative ρ value of –0.73 obtained in the plot of log(K_{add}) vs. σ_p. From this intermediate, there are two possible reaction pathways to give benzaldehyde product (PhCHO): benzylic hydrogen atom abstraction by the oxido group (path (i)) or by the fluoride group (path (ii)). In path (i),

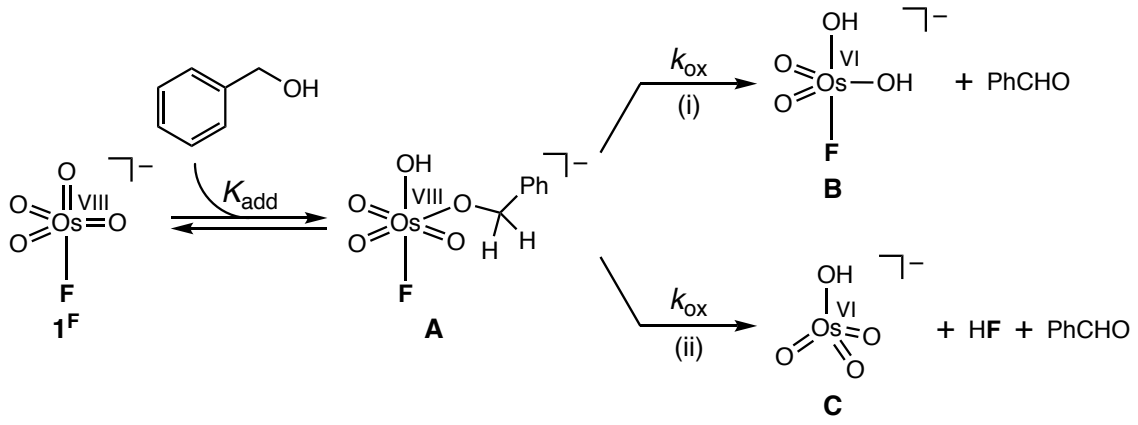

Scheme 2-2. Possible reaction mechanisms for the oxidation of benzyl alcohol by $\mathbf{1^F}$.

$[Os^{VI}O_2(OH)_2(F)]^-$ (**B**) is generated together with PhCHO after the reaction. On the other hand, in path (ii), the fluoride atom of the Os^{VIII}–F site of **A** abstracts hydrogen atom to give directly $[Os^{VI}O_3(OH)]^-$ (**C**), HF, and PhCHO. Since there is a relatively large KIE (4.5) in the benzyl alcohol oxidation, hydrogen atom abstraction (HAA) process is apparently involved in a rate-limiting step in both cases. Since the alcohol-adduct is the key intermediate, the author tried to detect it by using *tert*-butyl alcohol which may not be oxidized due to the absence of *α*-proton. However, the reaction did not proceed at all, probably due to the large steric hindrance of the *tert*-butyl group, preventing the initial adduct formation.

To get insights into the alcohol oxidation mechanism, density functional theoretical calculations were performed. Among the calculations for the singlet and triplet species, only the singlet species could be optimized. The calculated energy profiles for the possible mechanism were shown in Figure 2-5. In path (i), hydrogen atom abstraction by one of the oxido group at the equatorial position requires an activation barrier of 11.8 kcal/mol to produce **B** and benzaldehyde. Formation of **B** is exergonic by –63.5 kcal/mol. On the other hand, hydrogen atom abstraction by the coordinated fluoride group in path (ii) requires an activation barrier of 23.8 kcal/mol to produce **C**, HF, and benzaldehyde, although formation of **C** is also exergonic by –41.4 kcal/mol. Thus, it can be concluded that the oxidation of benzyl alcohol proceeds through path (i). The generated $[Os^{VI}O_2(OH)_2(F)]^-$ (**B**) may react with remained $[Os^{VIII}O_4(F)]^-$ ($\mathbf{1^F}$) to give $[Os^{VII}O_4]^-$ and HF. The yield of PhCHO was 36% based on the Os^{VIII} complex, which is consistent with the proposed mechanism, where the maximum yield of PhCHO is 50%.

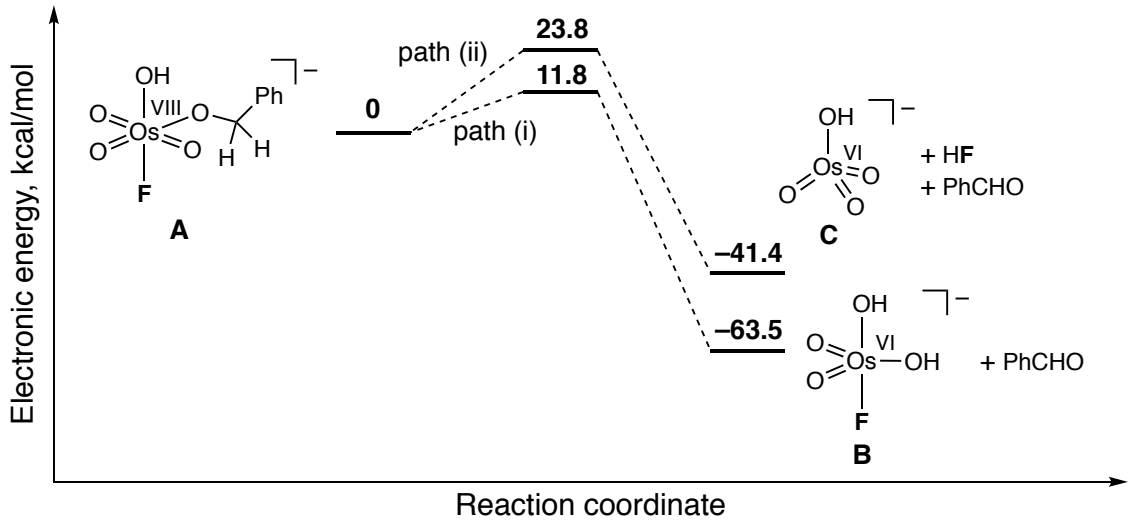

Figure 2-5. Computed energy diagrams for alcohol oxidation by $\mathbf{1^F}$ in the singlet state.

Conclusions

In Chapter 2, the reactions of OsO_4 with the series of halide anion (X^-) were examined to demonstrate that the interaction between the osmium center and X^- differs significantly. In the case of I^-, the adduct formation was observed only at a low temperature (–40 °C), from which homolytic Os^{VIII}–I bond cleavage occurs to give $[Os^{VII}O_4]^-$ and I•, the latter of which is converted to I_3^- *via* dimerization and subsequent association with I^- existing in the solution. On the other hand, Br^-, Cl^-, and F^- formed stable 1 : 1 adducts, $\mathbf{1^X}$, but the strength of the Os^{VIII}–X interaction is largely different among the three halide anions. Namely, the interaction of Os^{VIII}–Br is more like an electrostatic interaction having a significantly elongated bi-atomic distance of 3.4653(3) Å in the solid state, which is significantly longer than the sum of ionic radii of Os and Br atoms (2.35 Å). Thus, the formation constant (K_f^{Br}) is rather small as 0.69 M^{-1} in CH_3CN solution at 30 °C. The interaction between OsO_4 and Cl^- is stronger than that between OsO_4 and Br^- by one-order of magnitude (K_f^{Cl} = 8.5 M^{-1}). However, the distance between the osmium center and Cl atom (2.644(2) Å) is still longer than the sum of ionic radii of Os and Cl atoms (2.20 Å). Thus, the interaction between the osmium center and Br^- and Cl^- can be regarded as a *σ-hole interaction* as reported for the OsO_4-pyridine adducts.[55] Such an interaction resulted a structural distortion of the osmium center from tetrahedron to trigonal bipyramid.

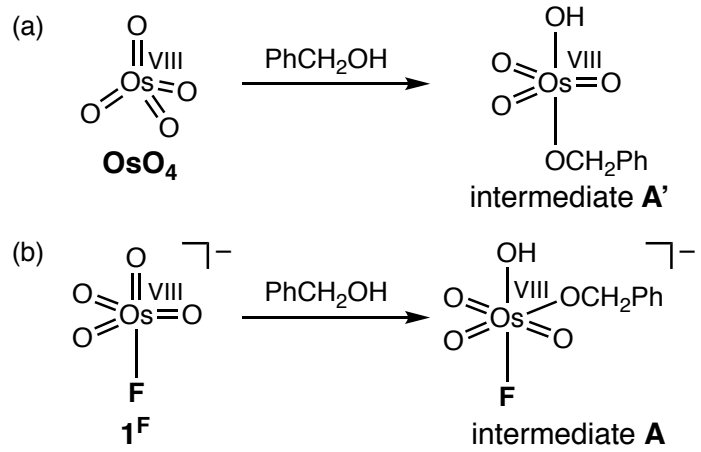

Scheme 2-3. Structural changes in the alcohol-addition step to (a) OsO_4 and to (b) $\mathbf{1^F}$.

Notably, F^- forms a strong *coordinative* interaction with the osmium center to give $\mathbf{1^F}$ having a slightly distorted trigonal bipyramidal structure. More importantly, the F-adduct $\mathbf{1^F}$ exhibited a higher reactivity compared to OsO_4 itself in the oxidation of benzyl alcohol. Kinetics and DFT calculation studies indicated that the reaction proceeds *via* adduct formation between $\mathbf{1^F}$ and benzyl alcohol substrate, from which hydrogen atom abstraction takes place from the benzylic position of the substrate by the oxido group in the adduct intermediate **A** to give benzaldehyde and Os^{VI} species. The enhancement of the alcohol-oxidation ability of OsO_4 can be attributed to the enhancement of the alcohol addition step to the osmium center. The structural change from the trigonal bipyramid of $\mathbf{1^F}$ to the octahedron of intermediate **A** may be easier than the direct addition of the alcohol substrate to the highly symmetric tetrahedral OsO_4 making a trigonal bipyramidal intermediate **A'** as shown in Scheme 2-3. Steric configuration between the oxido group and the benzylic position of the added alcohol substrate in intermediate **A** may also be favorable for the hydrogen atom abstraction step. The present results will give important insight into the effects of added base for the enhancement of OsO_4 reactivity.

References

1. V. VanRheenen, R. C. Kelly, D. Y. Cha, *Tetrahedron*. *Lett*. **1976**, *17*, 1973-1976.
2. M. J. Cleare, P. C. Hydes, W. P. Griffith, M. J. Wright, *J. Chem*. *Soc*., *Dalton Trans*. **1977**, 941-944.
3. K. B. Sharpless, A. Y. Teranishi, J. E. Backvall, *J. Am*. *Chem*. *Soc*. **1977**, *99*, 3120-3128.

4. S. G. Hentges, K. B. Sharpless, *J. Am. Chem. Soc*. **1980**, *102*, 4263-4265.
5. T. Yamada, K. Narasaka, *Chem. Lett*. **1986**, *15*, 131-134.
6. M. Tokles, J. K. Snyder, *Tetrahedron Lett*. **1986**, *27*, 3951-3954.
7. K. Tomioka, M. Nakajima, K. Koga, *J. Am. Chem. Soc*. **1987**, *109*, 6213-6215.
8. E. J. Corey, P. D. Jardine, S. Virgil, P. W. Yuen, R. D. Connell, *J. Am. Chem. Soc*. **1989**, *111*, 9243-9244.
9. M. Hirama, T. Oishi, S. Itô, *J. Chem. Soc*., *Chem. Commun*. **1989**, 665-666.
10. E. N. Jacobsen, I. Marko, M. B. France, J. S. Svendsen, K. B. Sharpless, *J. Am. Chem. Soc*. **1989**, *111*, 737-739.
11. K. Fuji, K. Tanaka, H. Miyamoto, *Tetrahedron Lett*. **1992**, *33*, 4021-4024.
12. T. Oishi, M. Hirama, *Tetrahedron Lett*. **1992**, *33*, 639-642.
13. Y. Imada, T. Saito, T. Kawakami, S.-I. Murahashi, *Tetrahedron Lett*. **1992**, *33*, 5081-5084.
14. S. Hanessian, P. Meffre, M. Girard, S. Beaudoin, J. Y. Sanceau, Y. Bennani, *J. Org. Chem*. **1993**, *58*, 1991-1993.
15. H. C. Kolb, P. G. Andersson, Y. L. Bennani, G. A. Crispino, K. S. Jeong, H. L. Kwong, K. B. Sharpless, *J. Am. Chem. Soc*. **1993**, *115*, 12226-12227.
16. E. J. Corey, S. Sarshar, M. D. Azimioara, R. C. Newbold, M. C. Noe, *J. Am. Chem. Soc*. **1996**, *118*, 7851-7852.
17. D. W. Nelson, A. Gypser, P. T. Ho, H. C. Kolb, T. Kondo, H.-L. Kwong, D. V. McGrath, A. E. Rubin, P.-O. Norrby, K. P. Gable, K. B. Sharpless, *J. Am. Chem. Soc*. **1997**, *119*, 1840-1858 .
18. B. C. Bales, P. Brown, A. Dehestani, J. M. Mayer, *J. Am. Chem. Soc*. **2005**, *127*, 2832-2833.
19. T. Osako, E. J. Watson, A. Dehestani, B. C. Bales, J. M. Mayer, *Angew. Chem., Int. Ed*. **2006**, *45*, 7433-7436.
20. A. Dehestani, W. H. Lam, D. A. Hrovat, E. R. Davidson, W. T. Borden, J. M. Mayer, *J. Am. Chem. Soc*. **2005**, *127*, 3423-3432.
21. J. M. Mayer, E. A. Mader, J. P. Roth, J. R. Bryant, T. Matsuo, A. Dehestani, B. C. Bales, E. J. Watson, T. Osako, K. Valliant-Saunders, W. H. Lam, D. A. Hrovat, W. T. Borden, E. R. Davidson, *J. Mol. Catal. A: Chem*. **2006**, *251*, 24-33.
22. F. H. Westheimer, A. Novick, *J. Chem. Phys*. **1943**, *11*, 506-512.

23. K. Bowden, I. M. Heilbron, E. R. H. Jones, B. C. L. Weedon, *J. Chem. Soc.* **1946**, 39-45.
24. G. I. Poos, G. E. Arth, R. E. Beyler, L. H. Sarett, *J. Am. Chem. Soc.* **1953**, *75*, 422-429.
25. R. U. Lemieux, E. V. Rudloff, *Can. J. Chem.* **1955**, *33*, 1701-1709.
26. K. B. Wiberg, K. A. Saegebarth, *J. Am. Chem. Soc.* **1957**, *79*, 2822-2824.
27. E. Klein, W. Rojahn, *Tetrahedron* **1965**, *21*, 2353-2358.
28. J. C. Collins, W. W. Hess, F. J. Frank, *Tetrahedron Lett.* **1968**, *9*, 3363-3366.
29. D. M. Walba, M. D. Wand, M. C. Wilkes, *J. Am. Chem. Soc.* **1979**, *101*, 4396-4397.
30. V. Duma, D. Hönicke, *J. Catal.* **2000**, *191*, 93-104.
31. F. Shi, M. K. Tse, M.-M. Pohl, A. Brückner, S. Zhang, M. Beller, *Angew. Chem., Int. Ed.* **2007**, *46*, 8866-8868.
32. V. Polshettiwar, R. S. Varma, *Org. Biomol. Chem.* **2009**, *7*, 37-40.
33. B. Anders, W. Karl-Axel, *Acta Chem. Scand.* **1950**, 1131-1141.
34. J. S. Stephens, D. W. J. Cruickshank, *Acta Cryst. B* **1970**, *26*, 222-226.
35. E. J. Corey, J. W. Suggs, *Tetrahedron Lett.* **1975**, *16*, 2647-2650.
36. G. Piancatelli, A. Scettri, M. D'Auria, *Synthesis* **1982**, 245-248.
37. N. Bernier, S. Carvalho, F. Li, R. Delgado, V. Félix, *The J. Org. Chem.* **2009**, *74*, 4819-4827.
38. S. K. Das, S. Roy, H. Khatua, B. Chattopadhyay, *J. Am. Chem. Soc.* **2020**, *142*, 16211-16217.
39. E. Bilger, J. Pebler, R. Weber, K. Dehnicke, *Z. Naturforsch., Teil. B*, **1984**, *39*, 259-261.
40. H. A. Benesi, J. H. Hildebrand, *J. Am. Chem. Soc.* **1949**, *71*, 2703-2707.
41. I. D. Kuntz, F. P. Gasparro, M. D. Johnston, R. P. Taylor, *J. Am. Chem. Soc.* **1968**, *90*, 4778-4781.
42. M. J. Frisch, G. W. Trucks, H. B. Schlegel, G. E. Scuseria, M. A. Robb, J. R. Cheeseman, G. Scalmani, V. Barone, G. A. Petersson, H. Nakatsuji, X. Li, M. Caricato, A. V. Marenich, J. Bloino, B. G. Janesko, R. Gomperts, B. Mennucci, H. P. Hratchian, J. V. Ortiz, A. F. Izmaylov, J. L. Sonnenberg, D. Williams-Young, F. Ding, F. Lipparini, F. Egidi, J. Goings, B. Peng, A. Petrone, T. Henderson, D. Ranasinghe, V. G. Zakrzewski, J. Gao, N. Rega, G. Zheng, W. Liang, M. Hada, M.

Ehara, K. Toyota, R. Fukuda, J. Hasegawa, M. Ishida, T. Nakajima, Y. Honda, O. Kitao, H. Nakai, T. Vreven, K. Throssell, J. A. Montgomery Jr., J. E. Peralta, F. Ogliaro, M. J. Bearpark, J. J. Heyd, E. N. Brothers, K. N. Kudin, V. N. Staroverov, T. A. Keith, R. Kobayashi, J. Normand, K. Raghavachari, A. P. Rendell, J. C. Burant, S. S. Iyengar, J. Tomasi, M. Cossi, J. M. Millam, M. Klene, C. Adamo, R. Cammi, J. W. Ochterski, R. L. Martin, K. Morokuma, O. Farkas, J. B. Foresman, D. J. Fox, Gaussian 16 Rev. A.03, Wallingford, CT, **2016**.

43. A. D. Becke, *Phys*. *Rev*. *A* **1988**, *38*, 3098-3100.
44. C. Lee, W. Yang, R. G. Parr, *Phys*. *Rev*. *B* **1988**, *37*, 785-789.
45. A. D. Becke, *J*. *Chem*. *Phys*. **1993**, *98*, 5648-5652.
46. M. Dolg, U. Wedig, H. Stoll, H. Preuss, *J*. *Chem*. *Phys*. **1987**, *86*, 866-872.
47. D. Andrae, U. Häußermann, M. Dolg, H. Stoll, H. Preuß, *Theoret*. *Chim*. *Acta* **1990**, *77*, 123-141.
48. R. Krishnan, J. S. Binkley, R. Seeger, J. A. Pople, *J*. *Chem*. *Phys*. **1980**, *72*, 650-654.
49. S. Fukuzumi, S. Kuroda, T. Tanaka, *J*. *Am*. *Chem*. *Soc*. **1985**, *107*, 3020-3027.
50. L. A. Woodward, H. L. Roberts, *Trans*. *Faraday Soc*. **1956**, *52*, 615-619.
51. R. Weber, K. Dehnicke, U. Müller, D. Fenske, *Z*. *anorg*. *allg*. *Chem*. **1984**, *516*, 214-222.
52. M. Gerken, D. A. Dixon, G. J. Schrobilgen, *Inorg*. *Chem*. **2000**, *39*, 4244-4255.
53. R. D. Shannon, *Acta Cryst*. *A* **1976**, *32*, 751-767.
54. H. M. Seip, *Selected Topics in Structure Chemistry*, ed. by P. Anderson, O. Bastiansen, S. Furberg, Oslo: Universitetsforlaget, **1967**, p. 25.
55. A. Daolio, A. Pizzi, M. Calabrese, G. Terraneo, S. Bordignon, A. Frontera, G. Resnati, *Angew*. *Chem*., *Int*. *Ed*. **2021**, *60*, 20723-20727.
56. A. M. Maione, A. Romeo, *Synthesis* **1984**, 955-957.
57. K. S. Coleman, M. Coppe, C. Thomas, J. A. Osborn, *Tetrahedron Lett*. **1999**, *40*, 3723-3726.
58. K. A. K. Lott, M. C. R. Symons, *J*. *Chem*. *Soc*. **1960**, 973-976.
59. T. E. Geswindt, W. J. Gerber, H. E. Rohwer, K. R. Koch, *Dalton Trans*. **2011**, *40*, 8581-8588.
60. H. Lineweaver, D. Burk, *J*. *Am*. *Chem*. *Soc*. **1934**, *56*, 658-666.

61. V. O. Gelmboldt, E. V. Ganin, M. S. Fonari, Y. A. Simonov, L. V. Koroeva, A. A. Ennan, S. S. Basok, S. Shova, H. Kählig, V. B. Arion, B. K. Keppler, *Dalton Trans*. **2007**, 2915-2924.
62. D. Sarauli, V. Popova, A. Zahl, R. Puchta, I. Ivanović-Burmazović, *Inorg*. *Chem*. **2007**, *46*, 7848-7860.

Supporting Information for Chapter 2

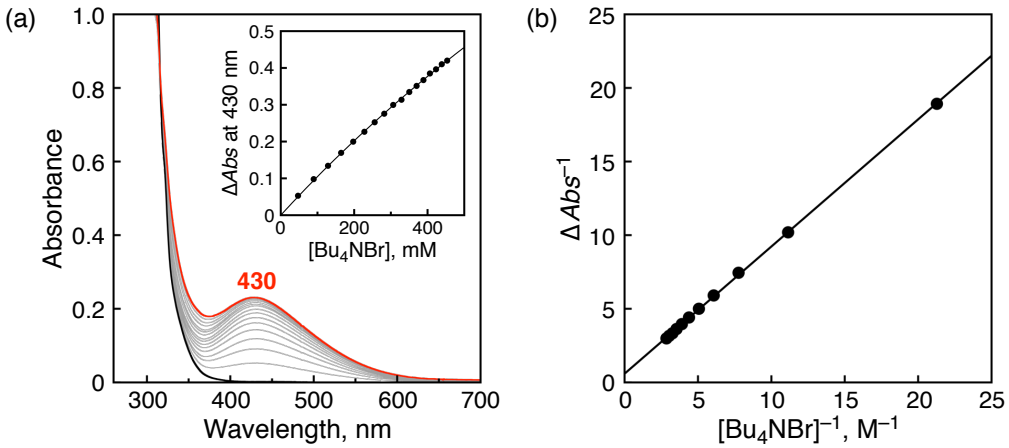

Figure 2-S1. (a) UV-vis spectral changes observed in the titration of OsO_4 (1.0 mM) by Bu_4NBr. Inset: Plot of ΔAbs at 430 nm against $[Bu_4NBr]$. (b) Plot of ΔAbs^{-1} against $[Bu_4NBr]^{-1}$.

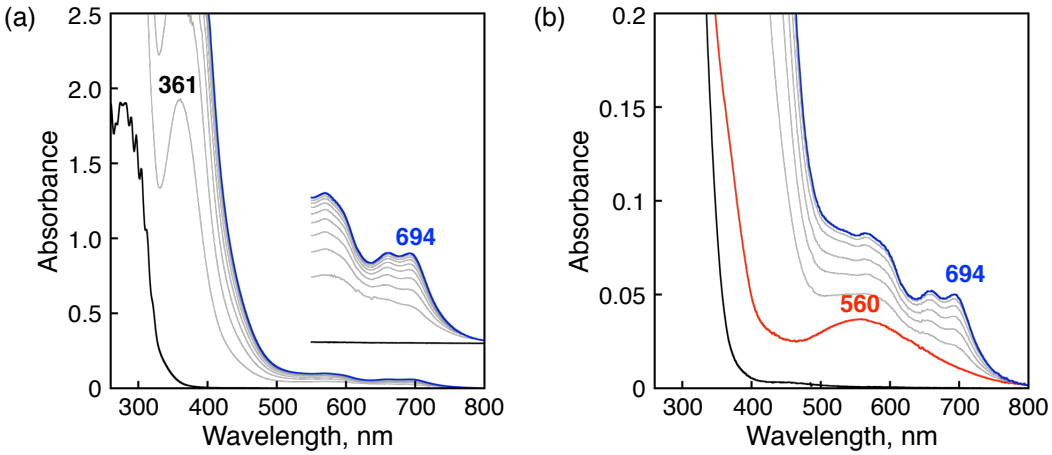

Figure 2-S2. UV-vis spectral changes observed in the reaction of OsO_4 (1.0 mM) with Bu_4NI (50 mM) (a) at 30 °C and (b) at –40 °C.

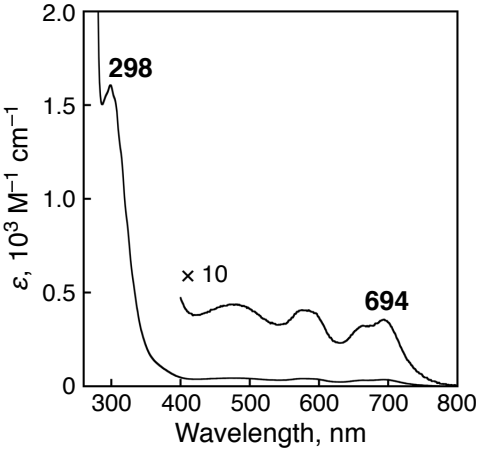

Figure 2-S3. UV-vis spectrum of the authentic sample of $[Ph_4P][Os^{VII}O_4]$ in CH_3CN.

Table 2-S1. The relationship between pK_a value of the conjugated acids (HX) and K_f^X.

X^-	pK_a of HX (in H_2O)	K_f^X
I^-	–10	—
Br^-	–9.0	0.69
Cl^-	–8.0	8.5
F^-	3.2	too large

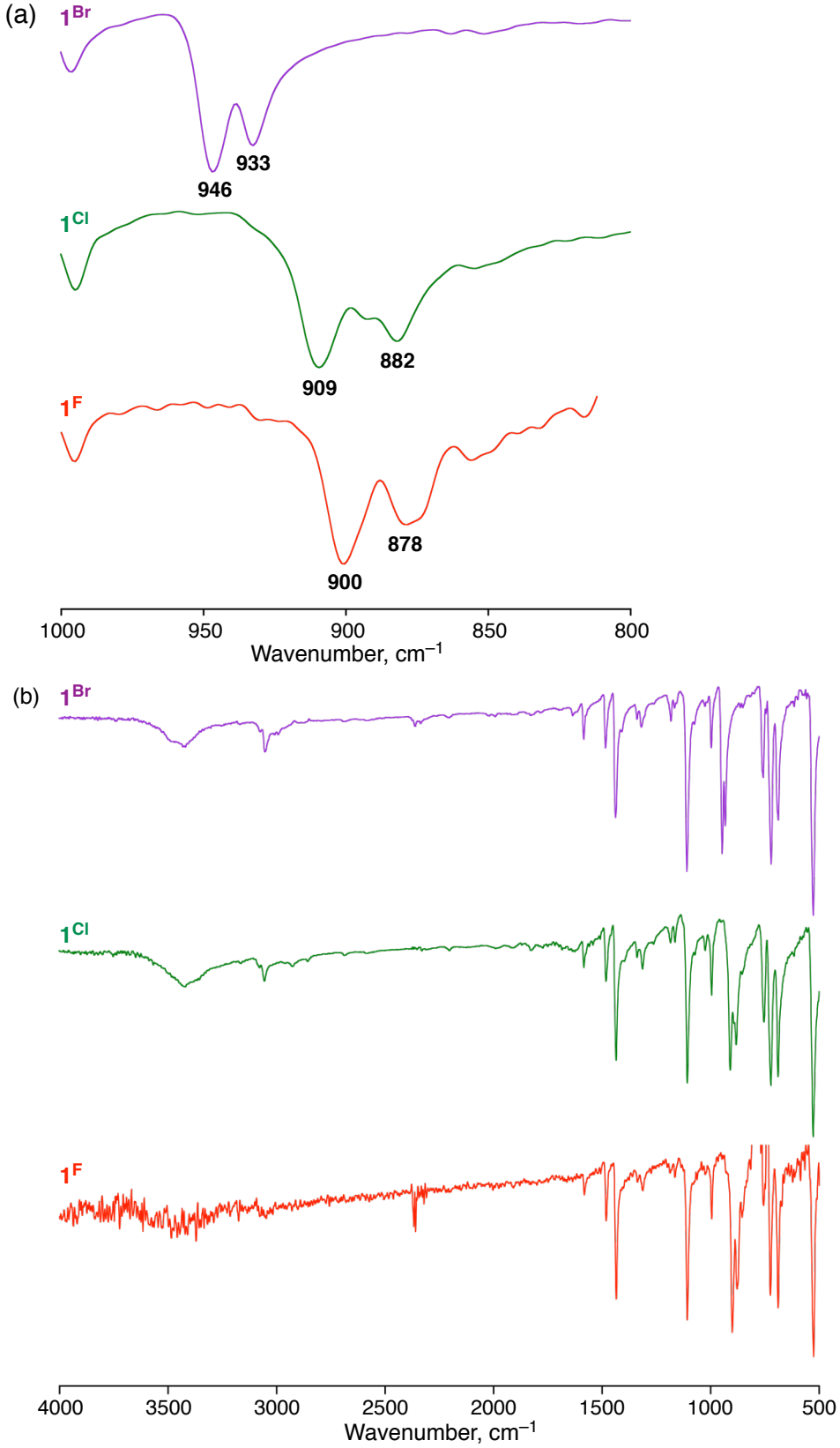

Figure 2-S4. FT-IR spectra of $\mathbf{1}^{\mathbf{Br}}$ (purple), $\mathbf{1}^{\mathbf{Cl}}$ (green), and $\mathbf{1}^{\mathbf{F}}$ (red) in a range from (a) 800 to 1000 cm^{-1} and (b) 500 to 4000 cm^{-1}.

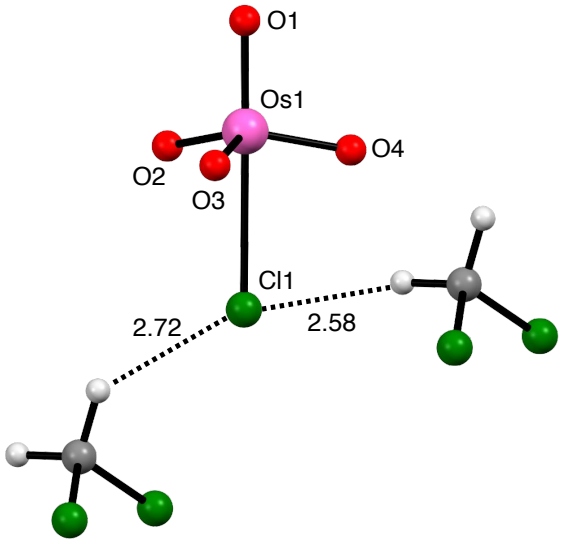

Figure 2-S5. Crystal structure of $[Ph_4P][OsO_4(Cl)]\bullet CH_2Cl_2$ ($\mathbf{1^{Cl'}}$) reported in Ref 51. Hydrogen bonds are indicated by dotted lines (the numbers shown in the figure represents bond distances (Å)).

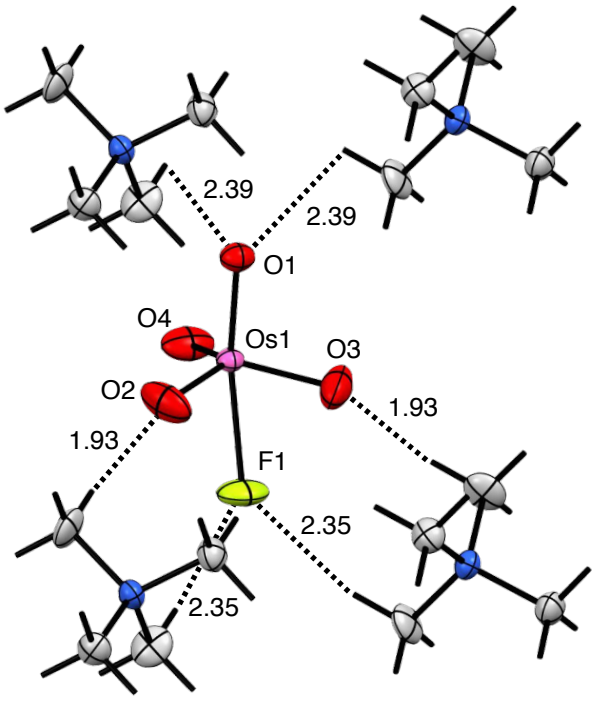

Figure 2-S6. Crystal structure of $[Me_4N][OsO_4(F)]$ ($\mathbf{1^{F'}}$) reported in Ref 52. Hydrogen bonds are indicated by dotted lines (the numbers shown in the figure represents bond distances (Å)).

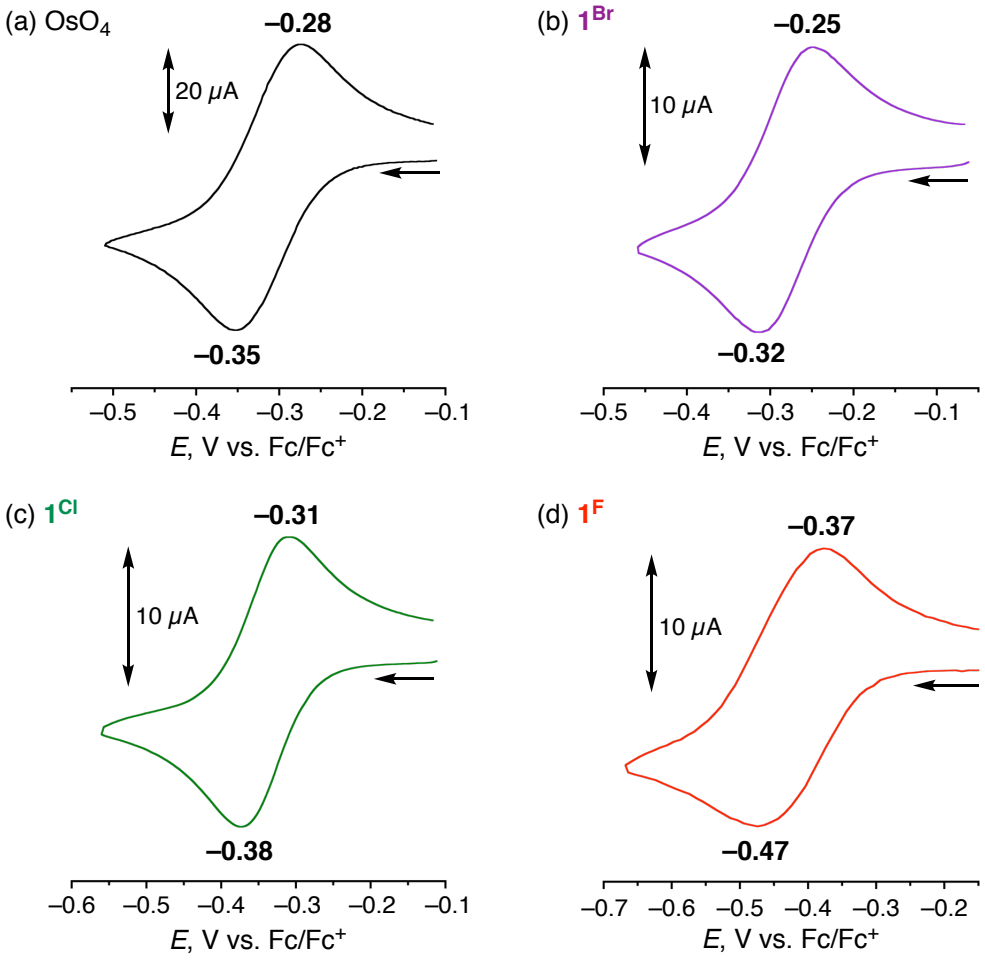

Figure 2-S7. Cyclic voltammograms of (a) OsO_4, (b) $\mathbf{1}^{Br}$, (c) $\mathbf{1}^{Cl}$, and (d) $\mathbf{1}^{F}$ in CH_3CN containing 0.1 M of Bu_4NPF_6 as the electrolyte at 25 °C. Conditions: $[OsO_4]_0 = 1.0$ mM, $[Bu_4NBr] = 1.8$ M (55% of $\mathbf{1}^{Br}$), $[Bu_4NCl] = 1.8$ M (94% of $\mathbf{1}^{Cl}$), $[Bu_4NF] = 1.0$ mM (100% of $\mathbf{1}^{F}$).

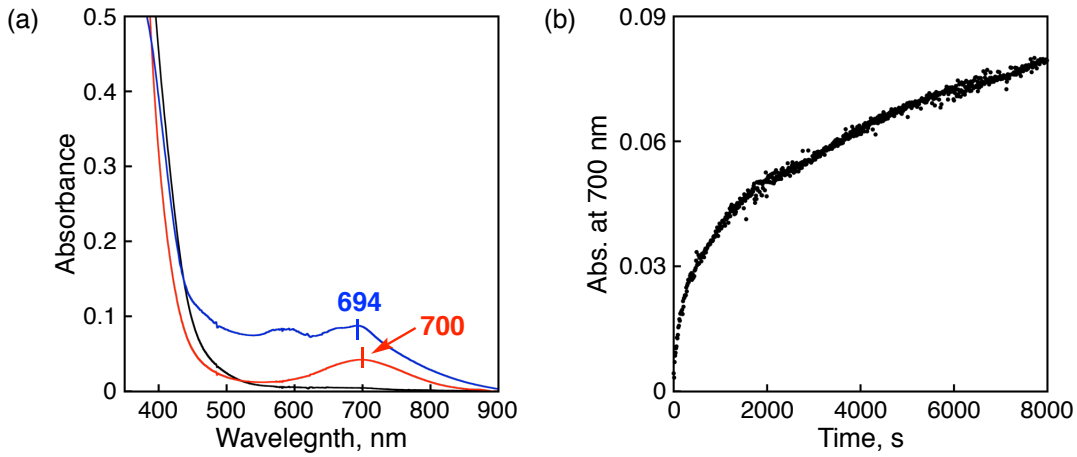

Figure 2-S8. (a) UV-vis spectral changes measured at 1200 sec (red) and 8000 sec (blue) after addition of benzyl alcohol (200 mM) to $\mathbf{1}^{\mathbf{F}}$ (1.0 mM, black) in CH_3CN at –40 °C. (b) The expanded time course of the growth of Os species monitored at 700 nm.

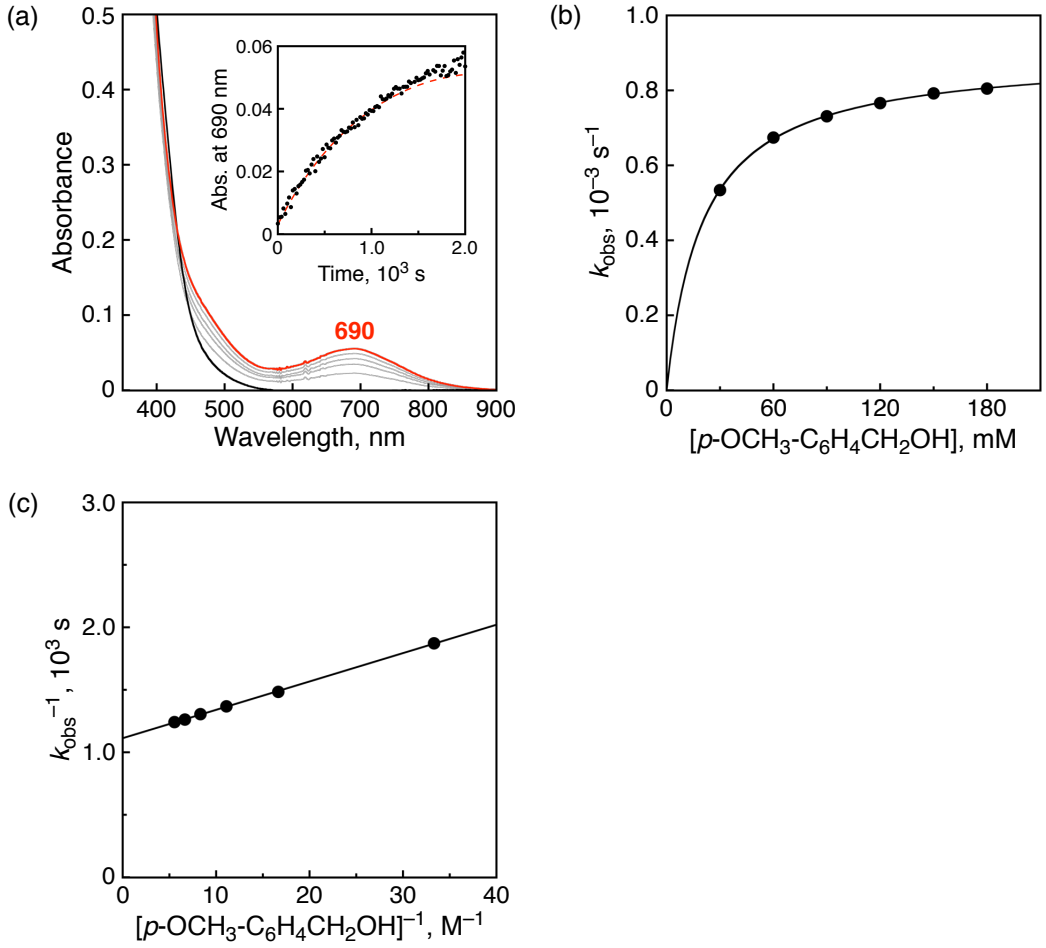

Figure 2-S9. (a) UV-vis spectral changes measured until 2000 sec after addition of *p*-methoxy benzyl alcohol (100 mM) to $\mathbf{1}^{\mathbf{F}}$ (1.0 mM, black) in CH_3CN at –40 °C. Inset: The time course of the absorption changes at 690 mm. (b) The Plot of k_{obs} against [*p*-OCH_3-$C_6H_4CH_2OH$]. (c) A double-reciprocal plot of k_{obs}^{-1} against [*p*-OCH_3-$C_6H_4CH_2OH$]$^{-1}$.

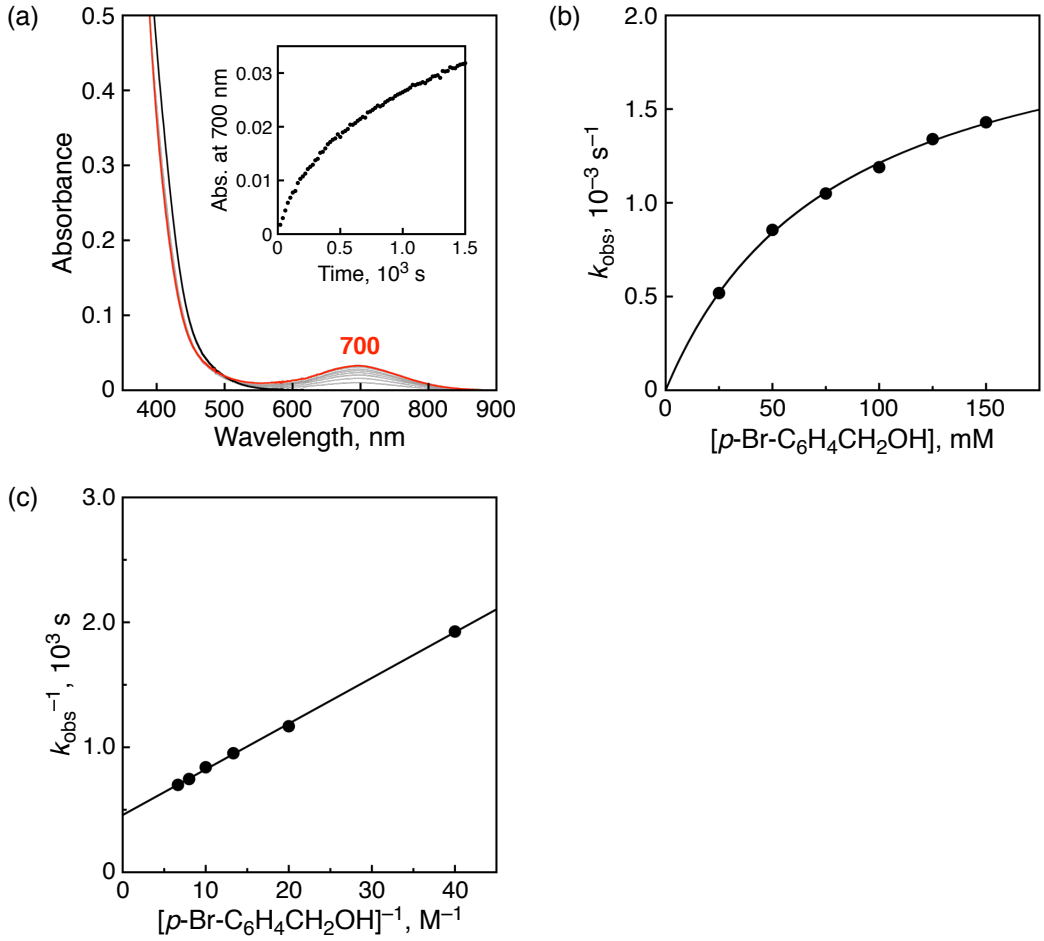

Figure 2-S10. (a) UV-vis spectral changes measured until 1500 sec after addition of *p*-bromobenzyl alcohol (50 mM) to $\mathbf{1}^{\mathbf{F}}$ (1.0 mM, black) in CH_3CN at –40 °C. Inset: The time course of the absorption changes at 700 mm. (b) The Plot of k_{obs} against [*p*-Br-$C_6H_4CH_2OH$]. (c) A double-reciprocal plot of k_{obs}^{-1} against [*p*-Br-$C_6H_4CH_2OH$]$^{-1}$.

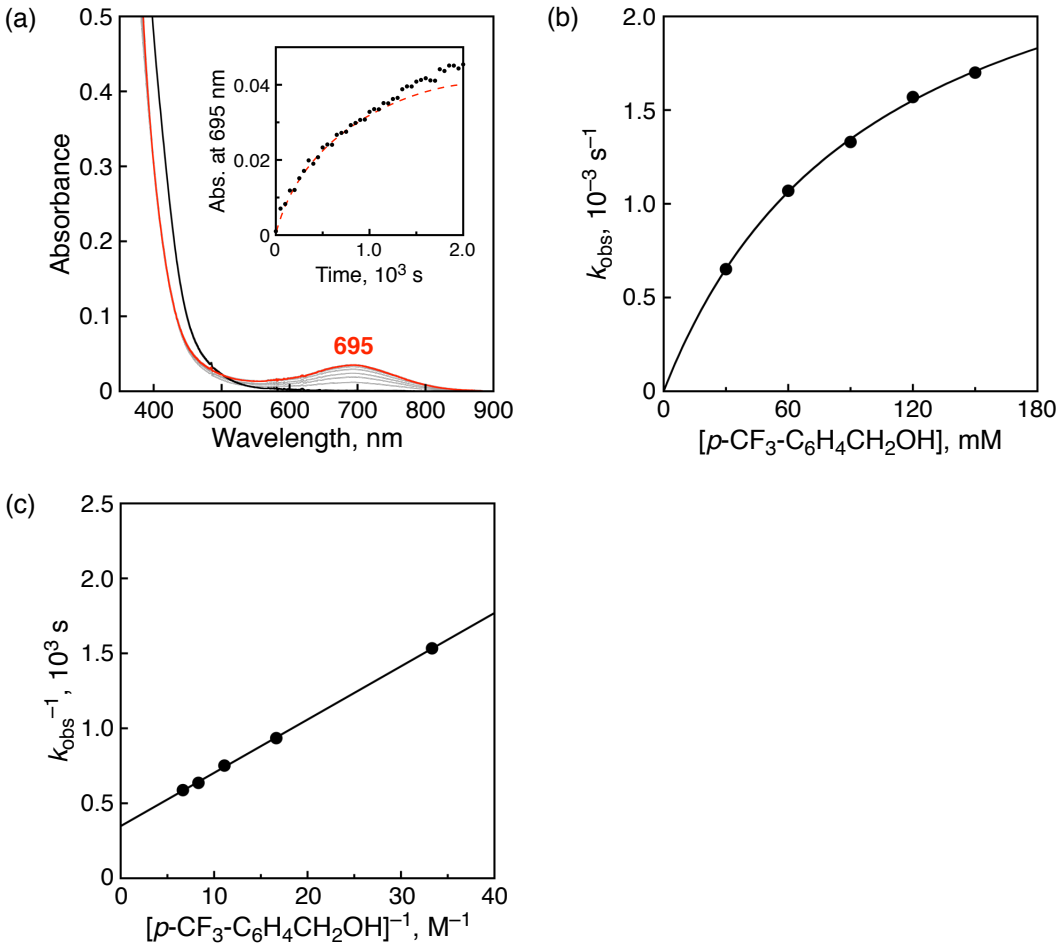

Figure 2-S11. (a) UV-vis spectral changes measured until 1200 sec after addition of *p*-(trifluoromethyl)benzyl alcohol (120 mM) to $\mathbf{1}^{\mathbf{F}}$ (1.0 mM, black) in CH_3CN at –40 °C. Inset: The time course of the absoption changes at 695 mm. (b) The Plot of k_{obs} against [*p*-CF_3-$C_6H_4CH_2OH$]. (c) A double-reciprocal plot of k_{obs}^{-1} against [*p*-CF_3-$C_6H_4CH_2OH$]$^{-1}$.

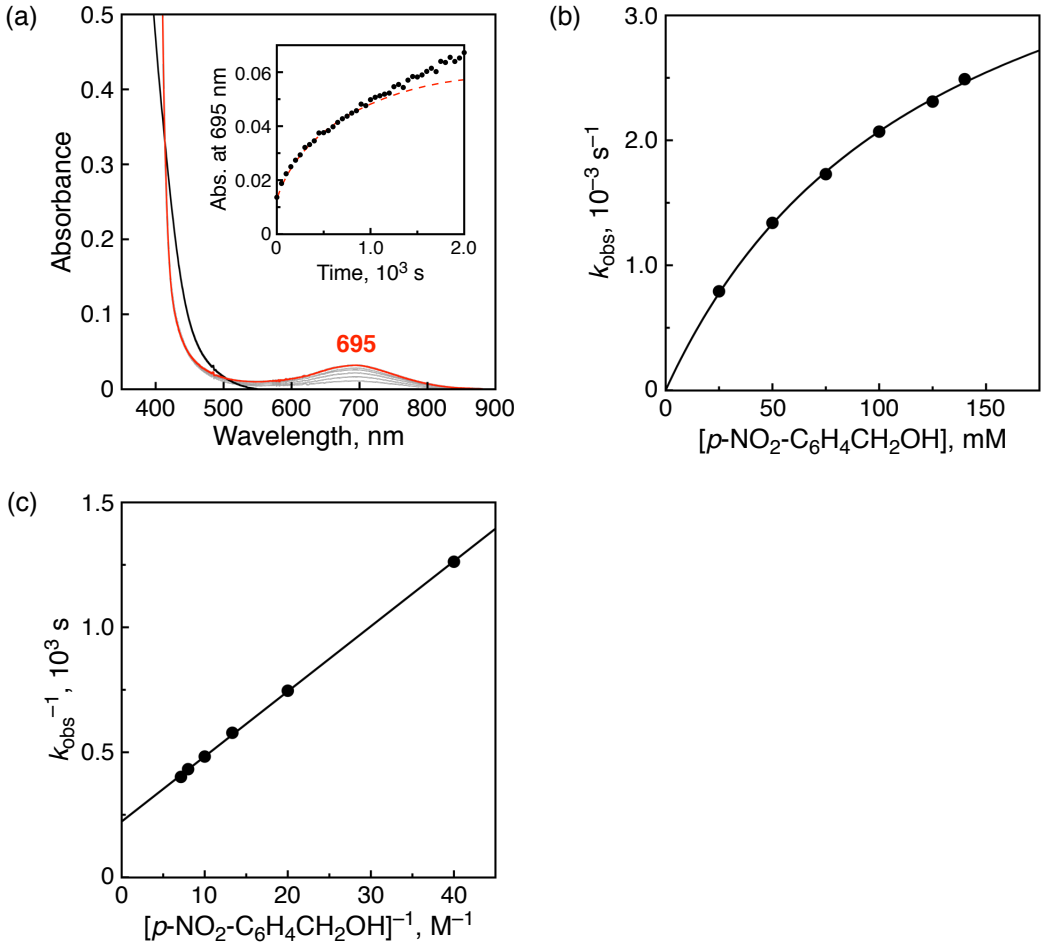

Figure 2-S12. (a) UV-vis spectral changes measured until 800 sec after addition of *p*-nitrobenzyl alcohol (125 mM) to $\mathbf{1}^{\mathbf{F}}$ (1.0 mM, black) in CH_3CN at –40 °C. Inset: The time course of the absorption changes at 695 mm. (b) The Plot of k_{obs} against [*p*-NO_2-$C_6H_4CH_2OH$]. (c) A double-reciprocal plot of k_{obs}^{-1} against [*p*-NO_2-$C_6H_4CH_2OH$]$^{-1}$.

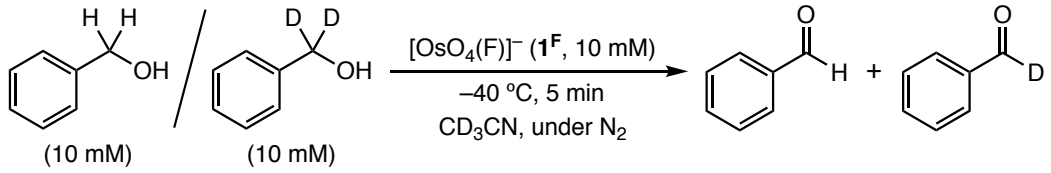

Scheme S1. Competitive oxidation reaction of $PhCH_2OH$ vs. $PhCD_2OH$.

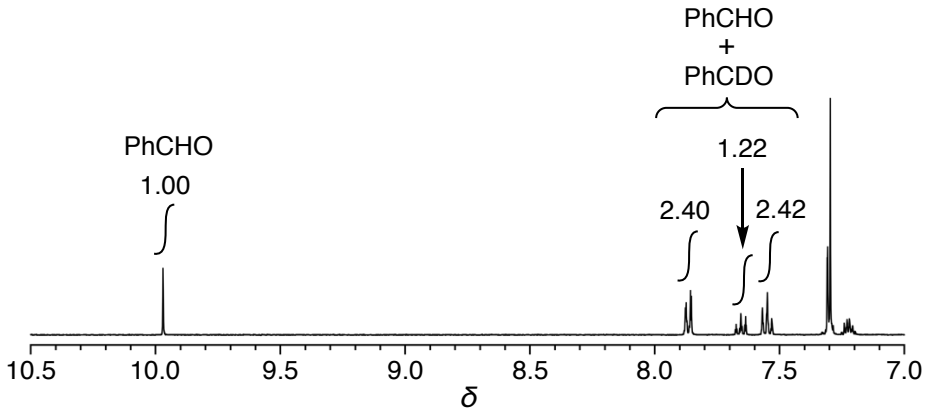

Figure 2-S13. ^1H NMR spectrum measured after the reaction of $\mathbf{1^F}$ with a 1 : 1 mixture of benzyl alcohol ($PhCH_2OH$) and deuterated benzyl alcohol ($PhCD_2OH$) in CD_3CN at –40 °C. Two peaks at 7.22 and 7.30 ppm are assigned to remained benzyl alcohol.

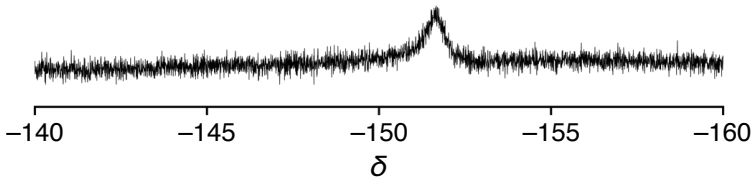

Figure 2-S14. ^{19}F NMR spectrum measured after the reaction of $\mathbf{1^F}$ with benzyl alcohol.

Chapter 3

C(sp^3)–H Bond Activation by Carboxylate-Adduct of OsO_4

Introduction

Activation of C(sp^3)–H bonds is of great importance in synthetic organic chemistry, industrial chemistry and biological chemistry. Metal-oxido complexes with a high oxidation state have been frequently employed as an oxidant in the oxidation of a variety of organic compounds in those systems. Osmium tetroxide (OsO_4) having the high oxidation state of VIII at the metal center is a versatile oxidant in synthetic organic chemistry.[1-3] Majority of the oxidation reactions induced by OsO_4 is, however, *cis*-dihydroxylation and *cis*-aminohydroxylation of alkenes.[4-12] In 2005, Mayer and co-workers reported that OsO_4 can also induce oxygenation reaction of simple alkanes under an aqueous alkaline condition (pH = 12.1, at 85 °C for 7 days), where alkane substrates having a tertiary C–H bond (R_3C–H) are oxidized to the corresponding alcohols (R_3C–OH) whereas cyclic alkanes having secondary C–H bonds (R_2CH_2) such as cyclohexane and cyclopentane are converted to the ring-opened dicarboxylic acid derivatives.[13] They also reported oxidation of methane to methanol using an OsO_4/$NaIO_4$ system in water.[14] Although mechanistic details of such alkane oxygenation reactions have yet to be clarified, a hydroxide adduct of OsO_4, $[OsO_4(OH)]^-$, was proposed as an active oxidant in the alkane oxygenation reaction, where the C–H bond oxidation proceeds *via* a concerted [3+ 2] mechanism illustrated in Scheme 3-1(a). On the other hand, Lau and co-workers reported that an oxido-osmium(V) complex, $[Os^V(O)(qpy)(pic)Cl]^{2+}$ (qpy = 2,2':6',2'':6'',2'''-quaterpyridine; pic = 4-picoline), exhibited C(sp^3)–H bond hydroxylation reactivity, for which they proposed hydrogen

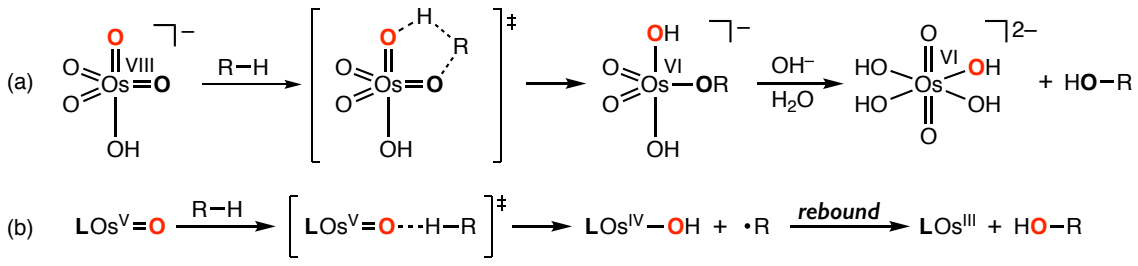

Scheme 3-1. Proposed mechanisms for C(sp^3)–H bond hydroxylation by osmium-oxido complexes.

atom abstraction and subsequent OH rebound mechanism (Scheme 3-1(b)).[15]

Meanwhile, it has been demonstrated that the oxidation ability of OsO_4 in the *cis*-dihydroxylation is largely enhanced when Lewis base such as pyridine coordinates to the Os-metal center.[16] The author has also found that coordination of fluoride anion (F^-) to OsO_4 enhances the reactivity toward alcohol oxidation reaction in Chapter 2.[17] Thus, it is highly desired to explore the effects of external ligands in more detail in the alkane oxidation reaction by OsO_4.

In Chapter 3, the author investigated the reactivity of carboxylate-adducts of OsO_4, $[OsO_4(X)]^-$ (**1**$^{\mathbf{X}}$, acetate: $X^- = AcO^-$ and benzoate: $X^- = BzO^-$) in C(sp^3)–H hydroxylation. Adoption of the carboxylate anion as the external ligand allowed us to perform isolation and structural characterization of the anion adducts of OsO_4 as well as kinetic studies on the hydroxylation reactions of a series of alkane substrates. Combined with DFT calculations, the author proposes a mechanism involving two oxido groups, acting as the hydrogen atom accepter from the alkane substrate (R–H) and the oxygen atom donor to the generated alkyl radical intermediate (R•), a stepwise version of the [3+2] mechanism.

Experimental Section

General. The reagents and the solvents used in this study were commercial products of the highest available purity and further purified by the standard methods, if necessary.[18] ^{1}H NMR spectra were recorded on a JEOL ECP400 or a JEOL ECS400 spectrometer. FT-IR spectra were recorded with a Jasco FT/IR-4100 spectrometer. Elemental analysis was carried out with a Yanaco CHN-Corder MT-5. UV-vis spectra were recorded on a Hewlett Packard 8453 photo diode array spectrometer or a Jasco V-650 spectrometer. Electrochemical measurements were performed with a Hokuto Denko HZ-7000. A set of carbon working electrode, an Ag/Ag^+ reference electrode, and a platinum counter electrode was employed in these experiments. After the CV measurements, ferrocene was added to the sample solution as an internal standard and the redox potential of Fc/Fc^+ was set as 0.0 V. A 0.1 M acetonitrile stock solution of OsO_4 was prepared by dissolving 1.0 g of OsO_4 (3.93 mmol) in 39.3 mL of acetonitrile and stored in a bottle with a screw cap. Products formed after the oxidation of substrates with osmium compounds were analyzed with a HPLC system of an EXTREMA series (JASCO Co.) equipped with a reverse-phase column (column: Nacalai Co. COSMOSIL 5C_{18}-AR-II, eluent: CH_3CN /

H_2O = 4 / 6). Ph_4POBz, $[Ph_4P][Os^{VII}O_4]$ and deuterated xanthene (xanthene-d_2) were synthesized by reported methods.[19-22]

Synthesis of $[Bu_4N][OsO_4(OAc)]$ ($\mathbf{1^{OAc}}$). Bu_4NOAc (60.3 mg, 0.20 mmol) was dissolved in a 2.0 mL of an acetonitrile stock solution containing 0.1 M OsO_4 (0.20 mmol), and the resultant solution was stirred for 15 min, during which color of the solution became orange. Diethyl ether was added to the resultant orange solution to give an orange powder, which was collected by filtration and dried under air. Yield: 87.7 mg (0.16 mmol, 79%). Single crystals suitable for X-ray crystallographic analysis were obtained by slow diffusion of diethyl ether into a dichloromethane solution containing the product complex. Elemental analysis data did not match well with the calculated values because the orange powder changed to a black powder under air within a few hours. UV-vis (in-situ generated $\mathbf{1^{OAc}}$ in acetonitrile): λ_{max} = 320 nm (ε = 2560 M^{-1} cm^{-1}), 390 (840). FT-IR (KBr): 886 ($\nu_{(Os=O)asym}$) and 909 cm^{-1} ($\nu_{(Os=O)sym}$). IR spectrum was measured quickly before the color changed to black.

Synthesis of $[Ph_4P][OsO_4(OBz)]$ ($\mathbf{1^{OBz}}$). This compound was prepared according to a similar procedure described for synthesis of $\mathbf{1^{OAc}}$ by using Ph_4POBz (50.2 mg, 0.20 mmol) instead of Bu_4NOAc. The generated violet powder was collected by filtration and dried under air. Yield: 62.6 mg (0.12 mmol, 62%). Single crystals suitable for X-ray crystallographic analysis were obtained by slow diffusion of diethyl ether into a dichloromethane solution containing the complex. Anal. Calcd. for $\mathbf{1^{OAc}}$ ($C_{31}H_{25}O_6OsP$): C, 52.09; H, 3.53%. Found: C, 52.45; H, 3.58%. UV-vis (acetonitrile): λ_{max} = 320 nm (ε = 2600 M^{-1} cm^{-1}), 390 (800). FT-IR (KBr): 886 ($\nu_{(Os=O)asym}$) and 906 cm^{-1} ($\nu_{(Os=O)sym}$).

Determination of formation constant (K_f) for Os-carboxylate adduct complexes $\mathbf{1^X}$. The titration of OsO_4 by $Bu_4N^+X^-$ (X^- = AcO^- or BzO^-) was carried out in acetonitrile at 30 °C using a 1.0 cm path length UV-vis cell closed with a septum cap. Concentrations of the reagents are described in the figure captions of Figures 3-1 and 3-S1. The formation constants of complexes $\mathbf{1^{OAc}}$ and $\mathbf{1^{OBz}}$ were calculated from the plots of $(A–A_0)/(A_\infty–A)$ against $[L]_0–\alpha[M]_0$ (α = $(A–A_0)/(A_\infty–A_0)$), which is ordinary used to determine larger equilibrium constants,[23, 24] where $[M]_0$ is the initial concentration of OsO_4, $[L]_0$ is concentration of the Bu_4NX added, A_0 and A_∞ are the initial and final

absorbance, respectively, and A is the observed absorbance at added [Bu_4NX] (eq. 1).

$$K_f([Bu_4NX]_0 - \alpha[OsO_4]_0) = \frac{A - A_0}{A_\infty - A} \quad \left[\alpha = \frac{A - A_0}{A_\infty - A_0} \right] \quad \text{— (1)}$$

Kinetic studies. All reactions of $\mathbf{1}^{\mathbf{OAc}}$ (0.5 mM) with the substrates (5.0-450 mM) were carried out in a 1.0 cm path length UV-cell closed with a septum cap. After generation of $\mathbf{1}^{\mathbf{OAc}}$ by the treatment of OsO_4 (0.5 mM) with Bu_4NOAc (5.0 mM) in acetonitrile, reactions were started by adding the substrate into the solution through a septum cap with using a microsyringe at 70 °C under N_2 atmosphere. The reactions were followed by monitoring the increase of an absorption band around 694 nm due to an Os^{VII} species. After the reaction, anisole was added into the resulting solution as an internal standard to analyze the products by HPLC. The yields of products were calculated by comparing the peak area of the products to those of the authentic samples using calibration curves.

X-ray crystallographic analysis. The single crystal was mounted on a loop with a mineral oil, and all X-ray data were collected at –170 °C on a Rigaku R-AXIS RAPID diffractometer using filtered Mo-Kα radiation. The structures were solved by direct method (SIR 2011) and expanded using Fourier techniques. The non-hydrogen atoms were refined anisotropically by full-matrix least-squares on F^2. The hydrogen atoms were attached at idealized positions on carbon atoms and were not refined. All of the crystallographic calculations were performed using the Crystal Structure software package of Molecular Structure Corp. [Crystal Structure, Crystal Structure Analysis Package, version 3.8.1, Molecular Structure Corp. and Rigaku Corp. (2005)]. Crystallographic parameters are summarized in Table 3-1.

Computational Details. The density-functional-theory (DFT) calculations were performed with the Gaussian 16 program package (Rev. C01).[25] All geometry optimizations were carried out with the M06 functional.[26] The SDD (Stuttgart/Dresden pseudopotentials) basis set[27, 28] for Os and the 6-311+G** basis set[29] for the other atoms were employed. After geometry optimizations, vibrational analyses were calculated for all reaction species to confirm stable and transition structures. Energy profiles of calculated pathway are presented as the SCF energy considering the solvent effect of acetonitrile (ε = 35.688) based on the Polarizable Continuum Model (PCM).[30]

Table 3-1. Crystallographic data for [Bu_4N][OsO_4(OAc)] (**1**^{OAc}) and [Ph_4P][OsO_4(OBz)] (**1**^{OBz}).

	1^{OAc}	**1**^{OBz}
Formula	$C_{18}H_{39}NO_6Os$	$C_{31}H_{25}O_6OsP$
Formula weight	555.74	714.71
Crystal system	Monoclinic	Monoclinic
Space group	$P2_1/c$ (#14)	$P2_1/c$ (#14)
a, Å	9.5061(6)	13.58334(10)
b, Å	14.4323(8)	9.34707(8)
c, Å	16.7770(9)	21.6745(2)
α, deg	90.0000	90.0000
β, deg	98.4039(19)	93.6901(7)
γ, deg	90.0000	90.0000
V, Å^3	2277.0(2)	2746.19(4)
Z	4	4
D_{calcd}, g/cm^{-3}	1.612	1.729
F(000)	1100.00	1400.00
μ(Mo-Kα), cm^{-1}	56.26	97.05 (Cu-Kα)
Crystal size, mm	0.20 × 0.20 × 0.10	—
T, K	103	153
$2\theta_{max}$, deg	55.0	148.9
No. of reflns obsd	5219	5464
No. of params	235	352
R_1[a]	0.0353	0.0372
wR_2[b]	0.0808	0.0996
GOF	1.075	0.397

[a] $R_1 = \Sigma(|F_o| - |F_c|)/\Sigma|F_o|$

[b] $wR_2 = [\Sigma(w(F_o^2 - F_c^2)^2)/\Sigma w(F_o^2)^2]^{1/2}$

Results and Discussion

Adduct formation of OsO_4 with carboxylate ions.

The reactions of OsO_4 with carboxylate ions, AcO^- and BzO^-, were first examined. In Figure 3-1(a) is shown the UV-vis spectral changes observed upon addition of various amounts of Bu_4NOAc to an acetonitrile solution of OsO_4 (0.5 mM) at 30 °C. OsO_4 has no absorption band in the visible region in CH_3CN, whereas an intense absorption band at 310 nm and a shoulder band at 390 nm gradually appeared as the amount of AcO^- increased. The spectral change almost completed when total concentration of Bu_4NOAc reached about 4.0 mM, and the plot of ΔAbs against the concentration of Bu_4NOAc gave a saturation curve (Figure 3-1(a), inset), which can be analyzed by using equation (1) (see Experimental Section). Thus, the plot of $(A–A_0)/(A_\infty–A)$ against $[Bu_4NOAc]_0 – \alpha[OsO_4]_0$ showed a straight line as shown in Figure 3-1(b), from which the formation constant K_f^{OAc} of $\mathbf{1}^{\mathbf{OAc}}$ was calculated as 5.7×10^3 M^{-1}. The formation constant K_f^{OBz} for $\mathbf{1}^{\mathbf{OBz}}$ was also determined as 5.4×10^3 M^{-1} by a similar manner (Figure 3-S1). In both cases, the K_f^X values are nearly the same, reflecting the similar pK_a value of the conjugated acid (22.3 of AcOH and 20.7 of BzOH in CH_3CN).

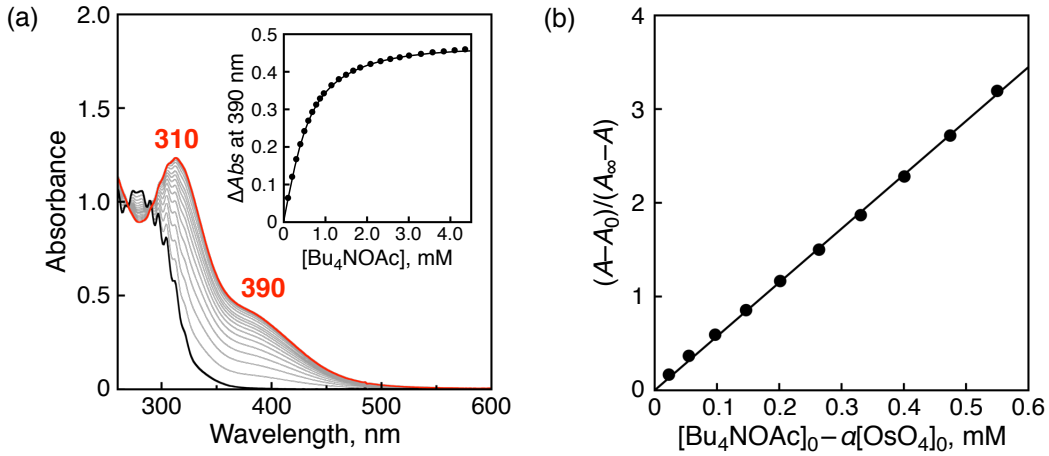

Figure 3-1. (a) UV-vis spectral changes observed in the titration of OsO_4 (0.5 mM) by Bu_4NOAc in acetonitrile at 30 °C. Inset: Plot of ΔAbs at 390 nm against $[Bu_4NOAc]$. (b) Plot of $(A–A_0)/(A_\infty–A)$ against $[Bu_4NOAc]_0 – \alpha[OsO_4]_0$.

Crystal structures and spectroscopic characteristics of $[OsO_4(X)]^-$.

The Os^{VIII}-carboxylate adducts, $[Bu_4N][OsO_4(OAc)]$ ($\mathbf{1}^{\mathbf{OAc}}$) and $[Ph_4P][OsO_4(OBz)]$ ($\mathbf{1}^{\mathbf{OBz}}$), were obtained as powder samples from the preparative scale reactions in acetonitrile (see Experimental Section). The isolated carboxylate-adducts exhibited two strong IR bands ascribable to asymmetric ($\nu_{(Os=O)asym}$) and symmetric ($\nu_{(Os=O)sym}$) Os=O stretches at 886 and 909 cm^{-1} for $\mathbf{1}^{\mathbf{OAc}}$ and 886 and 906 cm^{-1} for $\mathbf{1}^{\mathbf{OBz}}$, respectively, in the solid state (KBr) (Figure 3-S2). These values are lower than those of OsO_4 itself (954 and 965 cm^{-1}),[31] reflecting weakened Os=O bonds due to electron donation by the carboxylate anion and/or decrement of the coordination number from 4 to 5. Furthermore, the $\nu_{Os=O}$ values of $\mathbf{1}^{\mathbf{OAc}}$ and $\mathbf{1}^{\mathbf{OBz}}$ are nearly the same due to similar degree of Os–X bonding interaction as reflecting in the Os–X bond lengths in the crystal structures as described below.

The crystal structures of $\mathbf{1}^{\mathbf{OAc}}$ and $\mathbf{1}^{\mathbf{OBz}}$ are shown in Figure 3-2. The osmium centers are coordinated by the five oxygen atoms, four oxide oxygen atoms (O(1) to O(4)) and one carboxylate oxygen atom O(5). In $\mathbf{1}^{\mathbf{OAc}}$, the O(1)–Os(1)–O(5) angle is 177.45(1)°, and three bond angles of O(2)–Os(1)–O(3), O(2)–Os(1)–Os(4), and O(3)–Os(1)–O(4) are close each other (116.57(1), 115.93(2), and 118.50(2)°, respectively). The sum of the three bond angles is 351.0° and the Os(1) atom is located above the plane consisting of O(2), O(3), and O(4) atoms by 0.299 Å. The bond angles of O(1)–Os(1)–O(2), O(1)–Os(1)–O(3), and O(1)–Os(1)–O(4) also are very close each other (100.43(2), 100.28(2), and 99.56(2)°, respectively). It should be also noted that the Os(1)–O(1) bond is elongated upon coordination of AcO^- anion to the Os(1) center from 1.712 Å to 1.730(4) Å.[32] These observations reveal that the Os(1) center adopts a slightly distorted trigonal-bipyramidal geometry having a O(1)–Os(1)–O(5) C_{3v} axis. The overall structures of $\mathbf{1}^{\mathbf{OBz}}$ are similar to that of $\mathbf{1}^{\mathbf{OAc}}$ as shown in Figure 3-2. In this case as well, the coordination of BzO^- makes the osmium center to adapt a slightly distorted trigonal bipyramidal structure.

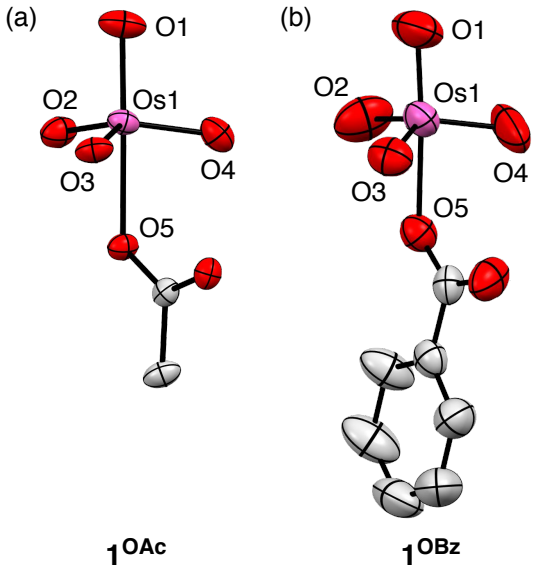

$\mathbf{1}^{\mathbf{OAc}}$ $\mathbf{1}^{\mathbf{OBz}}$

Figure 3-2. ORTEP drawings of (a) $\mathbf{1}^{\mathbf{OAc}}$ and (b) $\mathbf{1}^{\mathbf{OBz}}$ showing 50% probability thermal ellipsoids. Hydrogen atoms and counter cation are omitted for clarity. Selected bond distances (Å) and angles (°): For $\mathbf{1}^{\mathbf{OAc}}$, Os(1)–O(1), 1.730(4); Os(1)–O(2), 1.709(3); Os(1)–O(3), 1.706(3); Os(1)–O(4), 1.707(3); Os(1)–O(5), 2.218(3); O(1)–plane(O2O3O4), 0.299; O(1)–Os(1)–O(5), 177.45(1); O(1)–Os(1)–O(2), 100.43(2); O(2)–Os(1)–O(3), 116.57(1); O(3)–Os(1)–O(4), 118.50(2). For $\mathbf{1}^{\mathbf{OBz}}$, Os(1)–O(1), 1.719(5); Os(1)–O(2), 1.691(4); Os(1)–O(3), 1.704(4); Os(1)–O(4), 1.701(5); Os(1)–O(5), 2.225(3); O(1)–plane(O2O3O4), 0.302; O(1)–Os(1)–O(5), 175.54(2); O(1)–Os(1)–O(2), 99.80(3); O(2)–Os(1)–O(3), 116.28(2); O(3)–Os(1)–O(4), 117.39(2).

Electrochemical properties.

The cyclic voltammetric (CV) measurements were performed to examine the electronic effects of coordinated carboxylate anions. OsO_4 itself exhibited a reversible redox couple assignable to the Os(VIII)/Os(VII) redox process at $E_{1/2}$ = –0.32 V (vs. Fc/Fc^+, E_{pa} = –0.28 V, E_{pc} = –0.35 V, black line trace in Figure 3-3). Addition of an excess amount of Bu_4NOAc (10 mM) to the OsO_4 (1.0 mM) solution gave a quasi-reversible redox wave in the negative region (red line trace), from which the redox potential of complex $\mathbf{1}^{\mathbf{OAc}}$ ($E_{1/2}$) was determined as –0.42 V (vs. Fc/Fc^+, E_{pa} = –0.37 V, E_{pc} = –0.46 V). $\mathbf{1}^{\mathbf{OBz}}$ also gave a quasi-reversible redox couple (Figure 3-S3), from which $E_{1/2}$ values was determined as –0.42 V (vs. Fc/Fc^+, E_{pa} = –0.38 V, E_{pc} = –0.46 V).

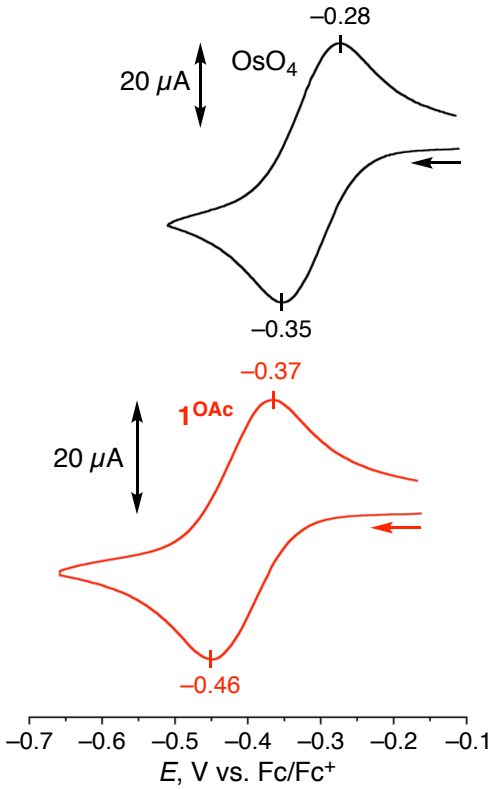

Figure 3-3. Cyclic voltammograms of OsO_4 (1.0 mM, black line trace) and that in the presence of Bu_4NOAc (10 mM, red line trace) in CH_3CN containing 0.1 M of Bu_4NPF_6 as the electrolyte at a scan rate of 100 mV/sec 25 °C.

The redox potential shifted to the negative direction compared to that of OsO_4, indicating that the coordination of the carboxylate anion makes the osmium center harder to be reduced. Such a negative shift of the redox potential (ΔE = 0.10 V) demonstrates that the electron-transfer oxidation power of complex $\mathbf{1}^{\mathbf{OAc}}$ and $\mathbf{1}^{\mathbf{OBz}}$ decreases by 9.6 kJ mol^{-1}.

Oxidation of C(sp^3)–H bonds by $\mathbf{1}^{\mathbf{X}}$.

The oxidation ability of $\mathbf{1}^{\mathbf{OAc}}$ and $\mathbf{1}^{\mathbf{OBz}}$ was examined in the oxidation of xanthene. In Figure 3-4(a) is shown the UV-vis spectral changes observed in the reaction of OsO_4 (0.5 mM) and xanthene (15 mM) in the presence of Bu_4NOAc (20 mM) in CH_3CN at 70 °C under N_2 atmosphere. Under this reaction condition, almost all OsO_4 is converted to the acetate adduct $\mathbf{1}^{\mathbf{OAc}}$ based on the K_f^{OAc} value determined by the titration at 70 °C (Figure 3-S4, $K_f^{OAc} = 1.3 \times 10^3$ M^{-1} at 70 °C in CH_3CN). The shoulder band around 390 nm due to $\mathbf{1}^{\mathbf{OAc}}$ decreased with concomitant increase of a new absorption bands at 573, 660, and 694 nm. These bands are similar to those of the authentic sample of $[Os^{VII}O_4]^-$

(Figure 3-S5), the formation of which was confirmed by ESI-MS of the resultant solution (Figure 3-S6). $[Os^{VII}O_4]^-$ can be generated by the comproportionation reaction between Os^{VI} species and remained $\mathbf{1}^{\mathbf{OAc}}$ as discussed below.[33] From the final reaction solution, xanthone (ketone) and xanthydrol (alcohol) were obtained in a 13 and a 22% yield based on OsO_4, respectively (Table 3-2). Since xanthone and xanthydrol are four-electron and two-electron oxidation products, respectively, the product yields based on the oxidation equivalent are 52 and 44%, respectively (total 96%). A similar result was obtained in the oxidation of xanthene by $\mathbf{1}^{\mathbf{OBz}}$ (Table 3-S1). On the other hand, such oxidation products were hardly obtained in the reaction of OsO_4 itself and xanthene under the same reaction condition (Table 3-S1). Thus, it is apparent that the adduct formation greatly enhances the reactivity of OsO_4 in the $C(sp^3)$–H bond oxidation reaction. Such an

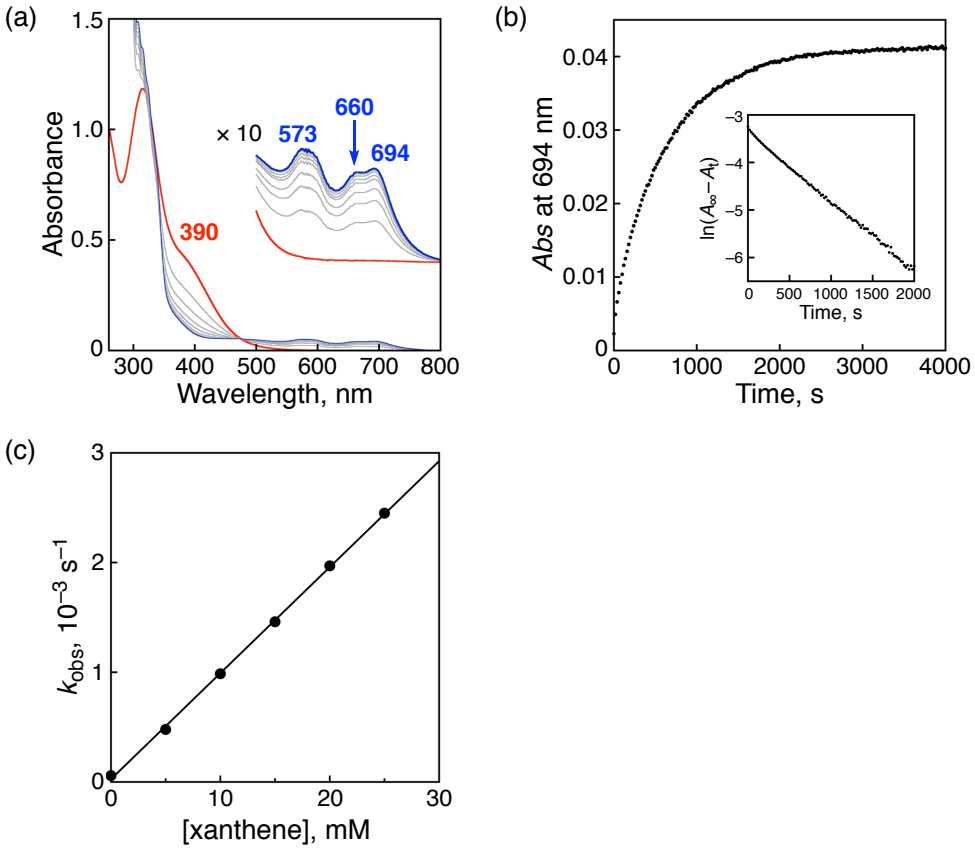

Figure 3-4. (a) UV-vis spectral change of $\mathbf{1}^{\mathbf{OAc}}$ ($[OsO_4]_0$ = 0.5 mM, $[Bu_4NOAc]_0$ = 20 mM) observed upon addition of xanthene (15 mM) in CH_3CN at 70 °C under N_2 atmosphere. (b) The time course of the growth of Os^{VII} species monitored at 694 nm ([xanthene] = 15 mM). Inset: Plot of $\ln(A_\infty - A_t)$ against the reaction time. (c) Plot of k_{obs} against [xanthene].

Table 3-2. Rate constants and products of the oxidation of C(sp^3)–H substrates by $\mathbf{1}^{\mathbf{OAc}}$.

Substrate[a]	BDE_{C-H} (kcal/mol)	k_2 (M^{-1} s^{-1})	k_2' (M^{-1} s^{-1})	Product[b] and Yield[c]
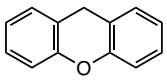	75.0	9.7×10^{-2}	4.8×10^{-2}	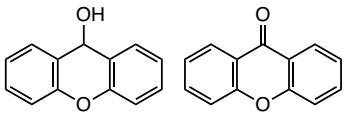 22% (44%) 13% (52%)
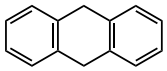	76.2	9.3×10^{-2}	2.3×10^{-2}	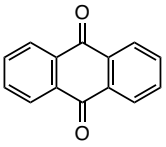 12% (96%)
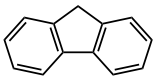	80.0	7.6×10^{-3}	3.8×10^{-3}	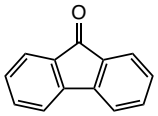 19% (76%)
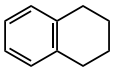	82.5	3.2×10^{-3}	0.81×10^{-3}	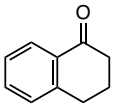 6% (24%)

[a] Reaction conditions: [$\mathbf{1}^{\mathbf{OAc}}$] = 0.5 mM (1.0 μmol / 2.0 mL) in the oxidation of xanthene (5.0 mM), [$\mathbf{1}^{\mathbf{OAc}}$] = 1.0 mM (2.0 μmol / 2.0 mL) in the oxidation of 9,10-dihydroanthracene (10 mM), fluorene (50 mM) and tetralin (200 mM) in CH_3CN at 70 °C for 2 h under N_2. [b] Products were detected by HPLC or ^1H NMR. [c] Numbers shown in the parenthesis are the yields based on the oxidation equivalent.

enhancement of oxidation ability of OsO_4 was also observed in alkene *cis*-dihydroxylation when pyridine was added to the reaction solution.[16] These phenomena are notable because the adduct formation causes the decrease of the electron-transfer oxidation ability of OsO_4 as mentioned above (Figure 3-3 and 3-S3). Thus, the oxidation of xanthene by $\mathbf{1}^{\mathbf{OAc}}$ and $\mathbf{1}^{\mathbf{OBz}}$ was further investigated kinetically to get further insights into the reaction mechanism.

The time course of the absorption changes at 694 nm is shown in Figure 3-4(b). The pseudo-first order rate constants (k_{obs}) were then determined by the plots of ln(ΔA) against the reaction time as shown in Figure 3-4(b) (inset). Then, the plot of k_{obs} against the concentrations of xanthene gave a straight line (Figure 3-4(c)), from the slope of which the second-order rate constant (k_2) was determined as 9.7×10^{-2} M^{-1} s^{-1}. The reaction of $\mathbf{1}^{\mathbf{OBz}}$ with xanthene were analyzed in the same way to get $k_2 = 7.6 \times 10^{-2}$ M^{-1}

s^{-1} at 70 °C, where K_f^{OBz} at 70 °C was also determined as 1.0×10^3 M^{-1} by a similar manner in the case of $\mathbf{1}^{OAc}$ (Figure 3-S7 and 3-S8). Since $\mathbf{1}^{OAc}$ and $\mathbf{1}^{OBz}$ showed similar reactivity, further kinetic studies were performed using $\mathbf{1}^{OAc}$.

The second-order rate constant k_2^D was determined as 1.0×10^{-2} M^{-1} s^{-1} using xanthene-d_2 (Figure 3-5 and 3-S9). Thus, the kinetic deuterium isotope effect (KIE = k_2^H/k_2^D) was determined as 9.7, indicating that the C(sp^3)–H bond cleavage of xanthene is involved in the rate determining step. In addition to xanthene (BDE_{C-H} = 75.0 kcal mol^{-1}), oxidation of 9,10-dihydroanthracene (BDE_{C-H} = 76.2 kcal mol^{-1}), fluorene (BDE_{C-H} = 80.0 kcal mol^{-1}), and 1,2,3,4-tetrahydronaphthalene (tetralin) (BDE_{C-H} = 82.5 kcal mol^{-1}) were also investigated in the same manner (Figure 3-S10–S12), and the normalized second-order rate constant (k_2') of each substrate was obtained by dividing the observed second-order rate constant k_2 with the number of equivalent C(sp^3)–H bond

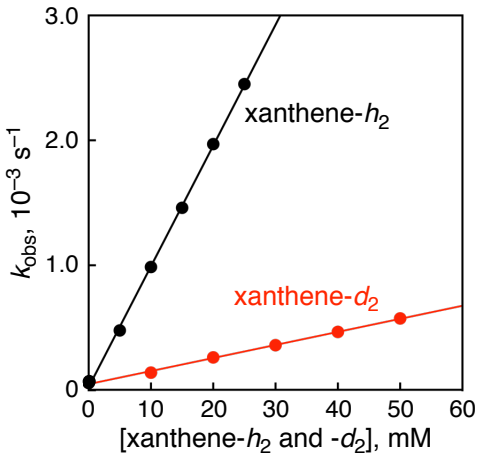

Figure 3-5. Plots of k_{obs} against [xanthene-h_2] and [xanthene-d_2].

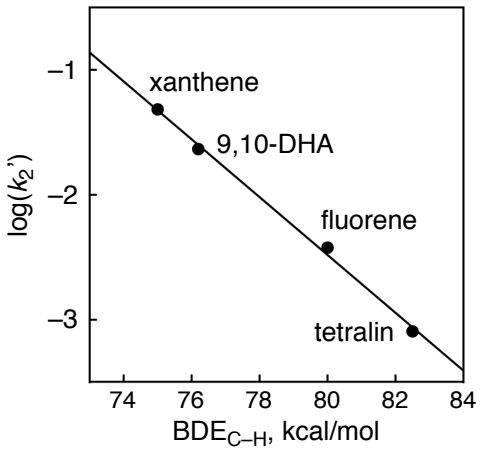

Figure 3-6. Plot of log(k_2') against BDE_{C-H} for the oxidation of a series of substrates.

in the substrate (Figure 3-S13). Figure 3-6 shows the plot of log(k_2') against the $BDE_{C–H}$ of the substrates. As clearly seen, there is a good linear correlation between them, strongly supporting that the reaction involves the C–H bond cleavage in the rate-limiting process.

Notably, the keto-products were obtained as the major products in the oxidation of 9,10-dihydroanthracene, fluorene and tetralin by $\mathbf{1}^{\mathbf{OAc}}$ (Table 3-2). For instance, anthraquinone was obtained in a 12% yield based on OsO_4, which corresponds to a 96% yield based on the oxidation equivalent, since anthraquinone is 8-electron oxidation product (12% × 8 = 96%). The yields of fluorene and α-tetralone (four-electron oxidation products) are 76 and 24% based on the oxidation equivalent, respectively. In the oxidation of tetralin, some oxidation products besides α-tetralone were observed by HPLC, however, they could not be identified.

To get insights into the oxidation mechanism, density functional theoretical (DFT) calculations were performed. Except for **A** + radical species, which is the open-shell singlet state, the ground state is the closed-shell singlet state. The calculated energy diagram and optimized structures in each step are shown in Figure 3-7 and 3-S14, respectively. First, a reactant complex (RC) was generated between $\mathbf{1}^{\mathbf{OAc}}$ and xanthene. Then, hydrogen atom abstraction takes place by the oxido group at the axial position of

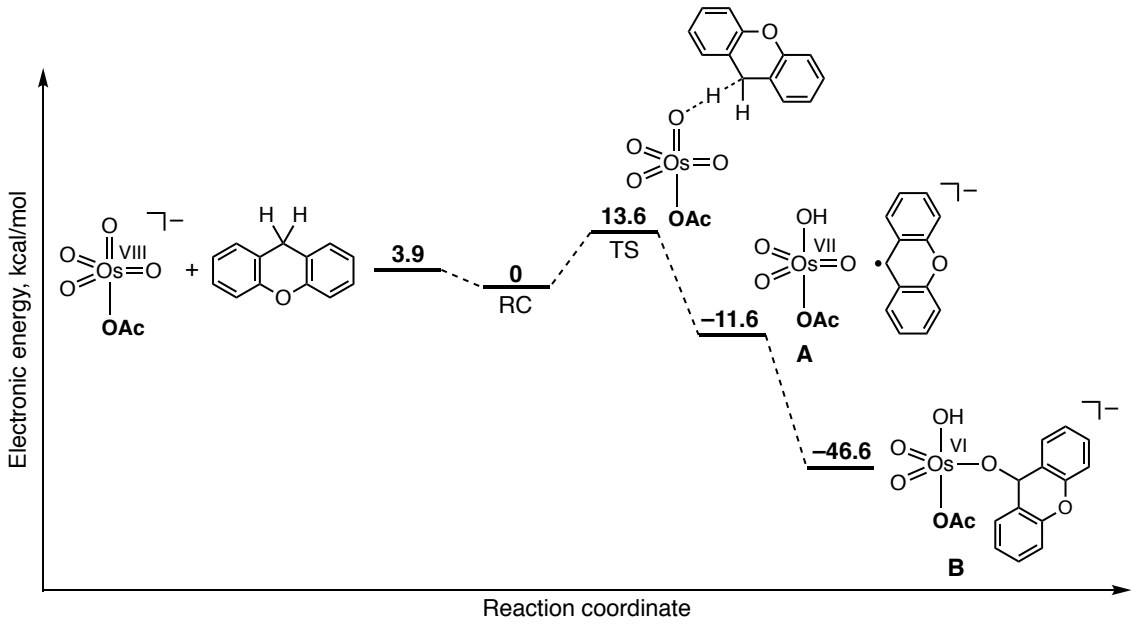

Figure 3-7. Computed energy diagrams for the oxidation of xanthene by 1^{OAc} in the singlet state.

$\mathbf{1}^{\mathbf{OAc}}$ *via* a transition-state (TS) with an activation barrier of 13.6 kcal/mol to produce hydroxido-osmium(VII) species **A** and a radical intermediate of the substrate. In the final step, the radical carbon atom binds to one of the three equatorial oxido groups of **A** with nearly barrierless in energy to form alkoxide product **B** (Figure 3-S15). The formation of **B** from RC is an exothermic reaction of 46.6 kcal/mol. These computed results indicated that the oxygen atom of the alcohol product is derived from one of the oxido groups in $\mathbf{1}^{\mathbf{OAc}}$.

In general, oxidation of 9,10-dihydroanthracene with metal-oxido complexes gives anthracene as the major product, which is formed by hydrogen atom abstraction and subsequent rapid aromatisation.[34-38] On the other hand, the reaction of 9,10-dihydroanthracene and $\mathbf{1}^{\mathbf{OAc}}$ only gave the oxygenated product, 9,10-anthraquinone (Table 3-2). Other substrates also gave the oxygenated products (Table 3-2). Thus, the bond formation between one oxido group of **A** and the carbon radical intermediate, generated by the initial hydrogen atom abstraction, may be much faster than the aromatization process. Then, alcohol product was dissociated from the alkoxide adduct **B** to give Os^{VI} species such as $[Os^{VI}(O)_3(OAc)]^-$. The generated Os^{VI} species may be oxidized by remained $[Os^{VIII}O_4(OAc)]^-$ to give $[Os^{VII}O_4]^-$, $Os^{VII}(O)_3(OAc)$ and AcO^- as experimentally detected as the final products (Figure 3-4(a) and Scheme 3-S1). On the other hand, the alcohol products may be immediately oxidized by $\mathbf{1}^{\mathbf{X}}$ to give the keto-products.

Conclusions

In Chapter 3, the reactions of OsO_4 with carboxylate anions (AcO^- and BzO^-) were examined to investigate the anion coordination effects on the structure, physicochemical properties and oxidation reactivity. The carboxylate anions formed stable 1 : 1 adducts with OsO_4, $\mathbf{1}^{\mathbf{X}}$ with the formation constants of $K_f^{OAc} = 5.7 \times 10^3\ M^{-1}$ and $K_f^{OBz} = 5.4 \times 10^3\ M^{-1}$. Structures of the 1 : 1 adduct $\mathbf{1}^{\mathbf{X}}$ were determined by X-ray crystallographic analysis as a slightly distorted trigonal bipyramid structure. The strong interaction induces the negative shift of the redox potentials of $\mathbf{1}^{\mathbf{OAc}}$ and $\mathbf{1}^{\mathbf{OBz}}$ in the cyclic voltammetric measurements. Nonetheless, these adducts showed a higher reactivity in the oxidation of benzylic $C(sp^3)$–H bonds compared to OsO_4 itself. Kinetics and DFT calculation studies indicated that the reaction proceeds *via* hydrogen atom abstraction

from the benzylic position of the substrate by the axial oxido group of $\mathbf{1}^{\mathbf{OAc}}$ and subsequent bond formation between carbon-center radical and one of the equatorial oxido ligands of Os^{VII}–hydroxido species **A** to give alkoxido-adduct **B** (Figure 3-7). The enhancement of the C(sp^3)–H oxidation ability of OsO_4 can be attributed to the increase of reactivity of the axial oxido group by strong anion coordination from *trans*-position, as reflected with the elongation of Os(1)–O(1) bond length (1.71 Å → 1.73 Å) and red shifts of $\nu_{Os=O}$ stretches by carboxylate anion coordination to OsO_4. These effects may enhance the hydrogen atom abstraction. The subsequent radical rebound to one of the oxido group at the equatorial position may also be enhanced by the structural distortion from tetrahedron to trigonal bipyramid. Namely, the steric relation between the oxygen atom of the oxido group in intermediate **A** and the carbon center radical may be favorable to induce the oxygen rebound process and prevent the aromatization reaction. The present studies give deeper insights into the [3+2] type alkane hydroxylation mechanism by with the anion-adducts of OsO_4.

References

1. H. C. Kolb, M. S. VanNieuwenhze, K. B. Sharpless, *Chem. Rev.* **1994**, *94*, 2483-2547.
2. H. C. Kolb, K. B. Sharpless, *Transition Metals for Organic Synthesis* **2004**, 309-336.
3. B. S. Pilgrim, T. J. Donohoe, *J. Org. Chem.* **2013**, *78*, 2149-2167.
4. N. A. Milas, S. Sussman, *J. Am. Chem. Soc.* **1936**, *58*, 1302-1304.
5. K. B. Sharpless, D. W. Patrick, L. K. Truesdale, S. A. Biller, *J. Am. Chem. Soc.* **1975**, *97*, 2305-2307.
6. K. B. Sharpless, K. Akashi, *J. Am. Chem. Soc.* **1976**, *98*, 1986-1987.
7. V. VanRheenen, R. C. Kelly, D. Y. Cha, *Tetrahedron Lett.* **1976**, *17*, 1973-1976.
8. K. B. Sharpless, A. O. Chong, K. Oshima, *J. Org. Chem.* **1976**, *41*, 177-179.
9. K. Akashi, R. E. Palermo, K. B. Sharpless, *J. Org. Chem.* **1978**, *43*, 2063-2066.
10. E. Herranz, S. A. Biller, K. B. Sharpless, *J. Am. Chem. Soc.* **1978**, *100*, 3596-3598.
11. R. Ray, D. S. Matteson, *Tetrahedron Lett.* **1980**, *21*, 449-450.
12. S. G. Hentges, K. B. Sharpless, *J. Org. Chem.* **1980**, *45*, 2257-2259.
13. B. C. Bales, P. Brown, A. Dehestani, J. M. Mayer, *J. Am. Chem. Soc.* **2005**, *127*, 2832-2833.

14. T. Osako, E. J. Watson, A. Dehestani, B. C. Bales, J. M. Mayer, *Angew*. *Chem*., *Int*. *Ed*. **2006**, *45*, 7433-7436.
15. Y. Liu, S.-M. Ng, W. W. Y. Lam, S.-M. Yiu, T.-C. Lau, *Angew*. *Chem*., *Int*. *Ed*. **2016**, *55*, 288-291.
16. D. W. Nelson, A. Gypser, P. T. Ho, H. C. Kolb, T. Kondo, H.-L. Kwong, D. V. McGrath, A. E. Rubin, P.-O. Norrby, K. P. Gable, K. B. Sharpless, *J*. *Am*. *Chem*. *Soc*. **1997**, *119*, 1840-1858.
17. T. Fujimoto, Y. Hirata, H. Sugimoto, M. Miyanishi, Y. Shiota, K. Yoshizawa, S. Itoh, *Bull*. *Chem*. *Soc*. *Jpn*. **2022**, *95*, 64-72.
18. N. Bernier, S. Carvalho, F. Li, R. Delgado, V. Félix, *J*. *Org*. *Chem*. **2009**, *74*, 4819-4827.
19. K. Harada, Y. Imbe, K. Nishihira, S. Tanaka, S. Fujitsu, R. Sugise, K. Kashiwagi, T. Sumida, T. Doi, M. Nishio, US Pat., 5,892,091, **1999**.
20. E. Bilger, J. Pebler, R. Weber, K. Dehnicke, *Z*. *Naturforsch*. *Teil*. *B* **1984**, *39*, 259-261.
21. H. Gao, J. T. Groves, *J*. *Am*. *Chem*. *Soc*. **2017**, *139*, 3938-3941.
22. M. A. Ehudin, D. A. Quist, K. D. Karlin, *J*. *Am*. *Chem*. *Soc*. **2019**, *141*, 12558-12569.
23. S. Itoh, H. Kawakami, S. Fukuzumi, *Biochemistry* **1998**, *37*, 6562-6571.
24. S. Itoh, M. Taniguchi, S. Fukuzumi, *Chem*. *Commun*. **2000**, 329-330.
25. M. J. Frisch, G. W. Trucks, H. B. Schlegel, G. E. Scuseria, M. A. Robb, J. R. Cheeseman, G. Scalmani, V. Barone, G. A. Petersson, H. Nakatsuji, X. Li, M. Caricato, A. V. Marenich, J. Bloino, B. G. Janesko, R. Gomperts, B. Mennucci, H. P. Hratchian, J. V. Ortiz, A. F. Izmaylov, J. L. Sonnenberg, D. Williams-Young, F. Ding, F. Lipparini, F. Egidi, J. Goings, B. Peng, A. Petrone, T. Henderson, D. Ranasinghe, V. G. Zakrzewski, J. Gao, N. Rega, G. Zheng, W. Liang, M. Hada, M. Ehara, K. Toyota, R. Fukuda, J. Hasegawa, M. Ishida, T. Nakajima, Y. Honda, O. Kitao, H. Nakai, T. Vreven, K. Throssell, J. A. Montgomery Jr., J. E. Peralta, F. Ogliaro, M. J. Bearpark, J. J. Heyd, E. N. Brothers, K. N. Kudin, V. N. Staroverov, T. A. Keith, R. Kobayashi, J. Normand, K. Raghavachari, A. P. Rendell, J. C. Burant, S. S. Iyengar, J. Tomasi, M. Cossi, J. M. Millam, M. Klene, C. Adamo, R. Cammi, J. W. Ochterski, R. L. Martin, K. Morokuma, O. Farkas, J. B. Foresman, D. J. Fox, Gaussian 16, Rev. A.03, Wallingford, CT, **2016**.

26. Y. Zhao, D. G. Truhlar, *Theor*. *Chem*. *Acc*. **2008**, *120*, 215-241.
27. M. Dolg, U. Wedig, H. Stoll, H. Preuss, *J. Chem*. *Phys*. **1987**, *86*, 866-872.
28. D. Andrae, U. Häußermann, M. Dolg, H. Stoll, H. Preuß, *Theoret*. *Chim. Acta* **1990**, *77*, 123-141.
29. R. Krishnan, J. S. Binkley, R. Seeger, J. A. Pople, *J. Chem*. *Phys*. **1980**, *72*, 650-654.
30. M. Cossi, V. Barone, R. Cammi, J. Tomasi, *Chem*. *Phys*. *Lett*. **1996**, *255*, 327-335.
31. L. A. Woodward, H. L. Roberts, *Trans*. *Faraday Soc*. **1956**, *52*, 615-619.
32. H. M. Seip, *Selected Topics in Structure Chemistry*, ed. P. Anderson, O. Bastiansen and S. Furberg, Oslo: Universitetsforlaget, **1967**, p. 25.
33. T. E. Geswindt, W. J. Gerber, H. E. Rohwer, K. R. Koch, *Dalton Trans*. **2011**, *40*, 8581-8588.
34. J. R. Bryant, J. M. Mayer, *J. Am*. *Chem*. *Soc*. **2003**, *125*, 10351-10361.
35. T. H. Parsell, M.-Y. Yang, A. S. Borovik, *J. Am*. *Chem*. *Soc*. **2009**, *131*, 2762-2763.
36. A. Company, I. Prat, J. R. Frisch, D. R. Mas-Ballesté, M. Güell, G. Juhász, X. Ribas, D. E. Münck, J. M. Luis, L. Que Jr, M. Costas, *Chem*. *Eur*. *J*. **2011**, *17*, 1622-1634.
37. S. Hong, F. F. Pfaff, E. Kwon, Y. Wang, M.-S. Seo, E. Bill, K. Ray, W. Nam, *Angew*. *Chem*., *Int*. *Ed*., **2014**, *53*, 10403-10407.
38. B. Wang, Y.-M. Lee, W.-Y. Tcho, S. Tussupbayev, S.-T. Kim, Y. Kim, M. S. Seo, K.-B. Cho, Y. Dede, B. C. Keegan, T. Ogura, S. H. Kim, T. Ohta, M.-H. Baik, K. Ray, J. Shearer, W. Nam, *Nat*. *Commun*. **2017**, *8*, 14839.

Supporting Information for Chapter 3

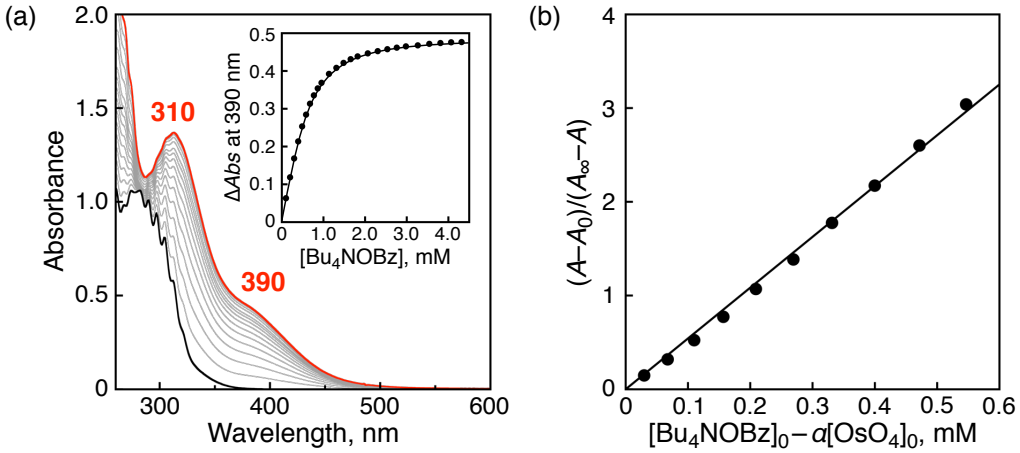

Figure 3-S1. (a) UV-vis spectral changes observed in the titration of OsO_4 (0.5 mM) by Bu_4NOBz in acetonitrile at 30 °C. Inset: Plot of ΔAbs at 390 nm against $[Bu_4NOBz]$. (b) Plot of $(A-A_0)/(A_\infty-A)$ against $[Bu_4NOBz]_0 - \alpha[OsO_4]_0$.

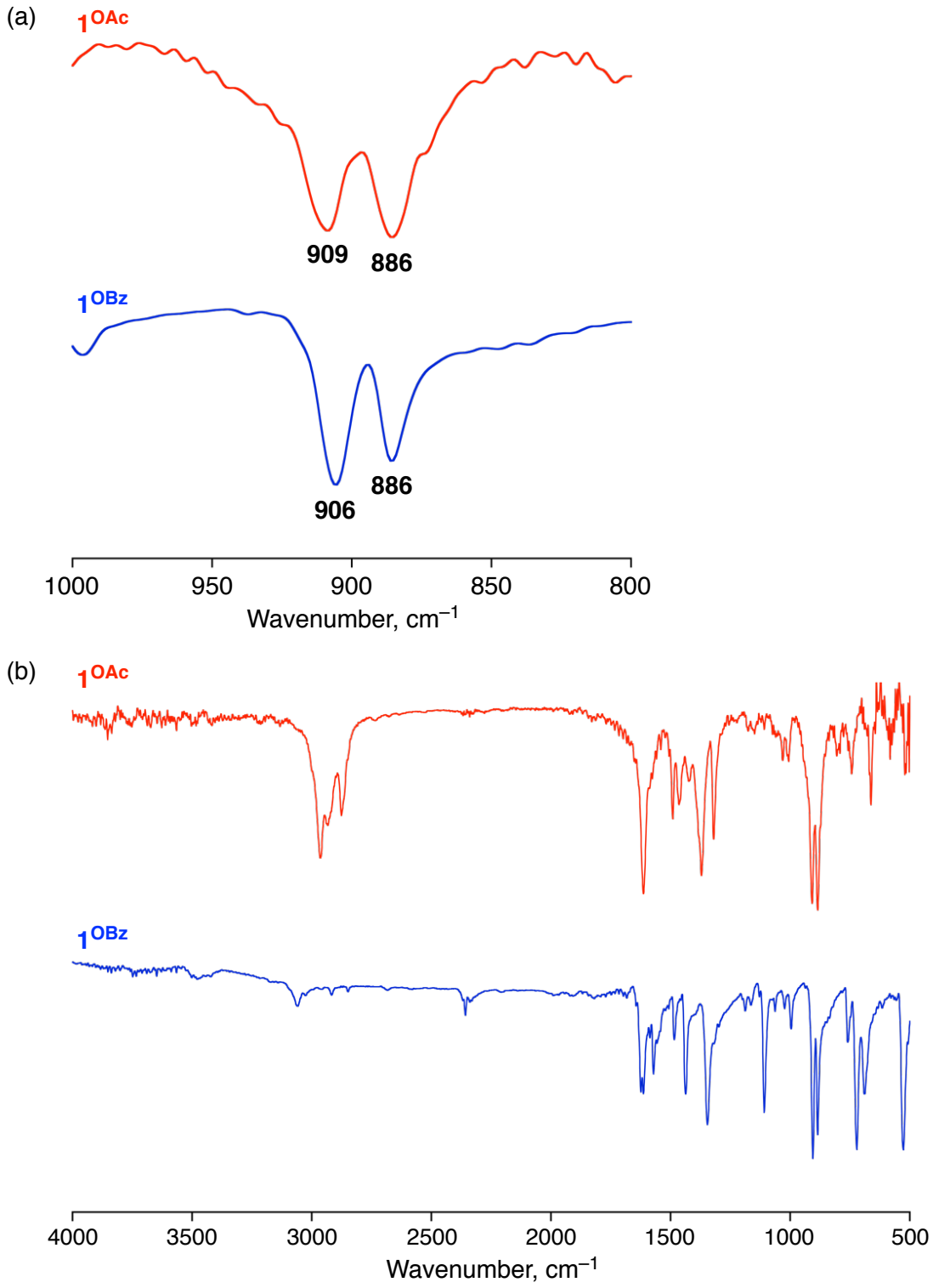

Figure 3-S2. FT-IR spectra of $\mathbf{1}^{\mathbf{OAc}}$ (red) and $\mathbf{1}^{\mathbf{OBz}}$ (blue) in a range from (a) 800 to 1000 cm^{-1} and (b) 500 to 4000 cm^{-1}.

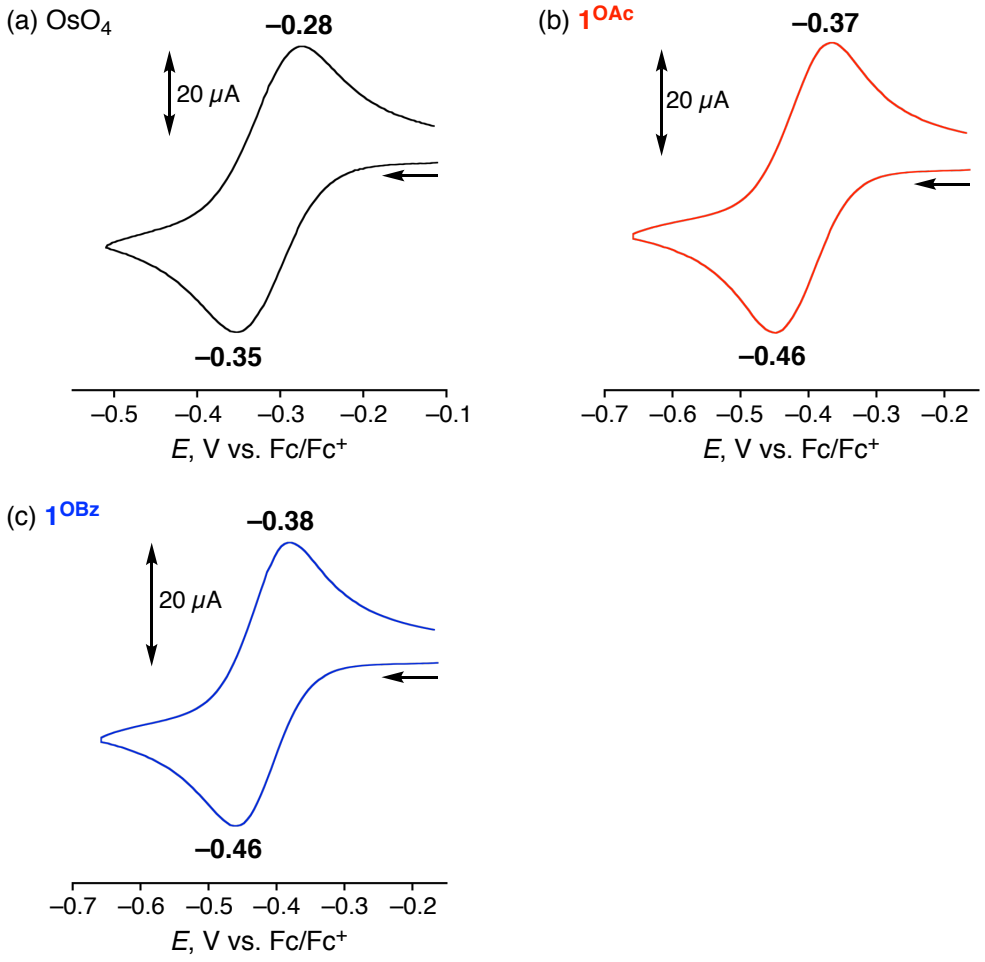

Figure 3-S3. Cyclic voltammograms of (a) OsO_4, (b) $\mathbf{1}^{\mathbf{OAc}}$, and (c) $\mathbf{1}^{\mathbf{OBz}}$ in CH_3CN containing 0.1 M of Bu_4NPF_6 as the electrolyte at 25 °C. Conditions: $[OsO_4]_0 = 1.0$ mM, $[Bu_4NOAc] = 10$ mM, $[Bu_4NOBz] = 10$ mM, Scan rate = 100 mV/sec.

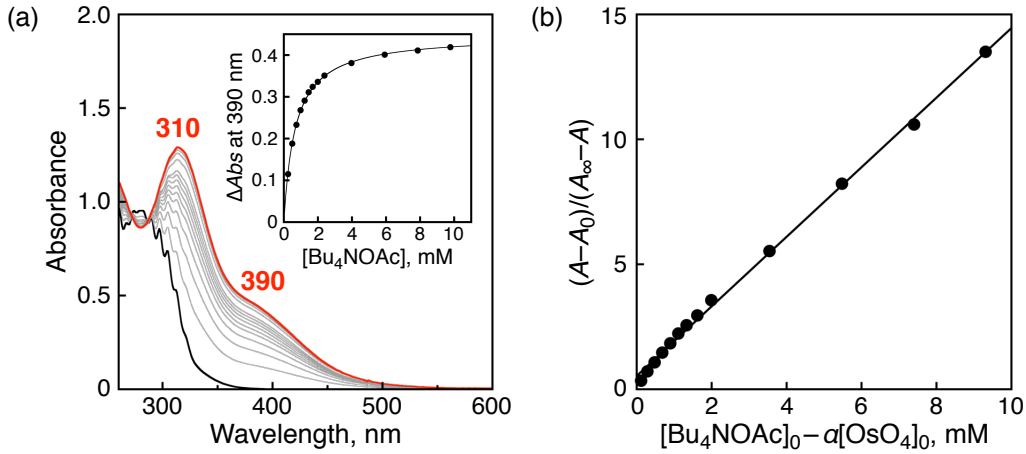

Figure 3-S4. (a) UV-vis spectral changes observed in the titration of OsO_4 by Bu_4NOAc at 70 °C. Inset: ΔAbs at 390 nm. (b) Plot of $(A–A_0)(A_\infty–A)$ against $[Bu_4NOAc]_0 – \alpha[OsO_4]_0$ according to equation (1) ($K_f^{OAc} = 1.3 \times 10^3$ M^{-1} at 70 °C in CH_3CN).

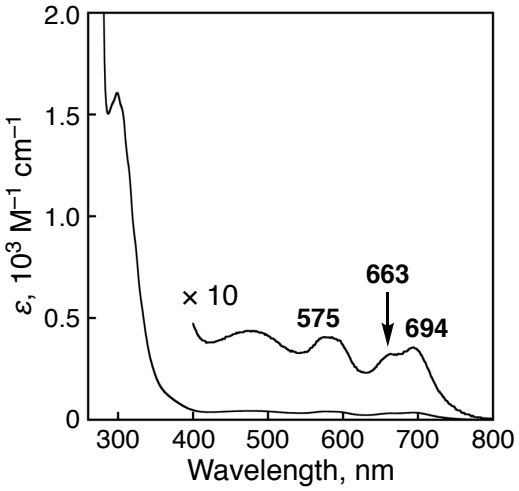

Figure 3-S5. UV-vis spectrum of the authentic sample of $[PPh_4][Os^{VII}O_4]$ in CH_3CN.

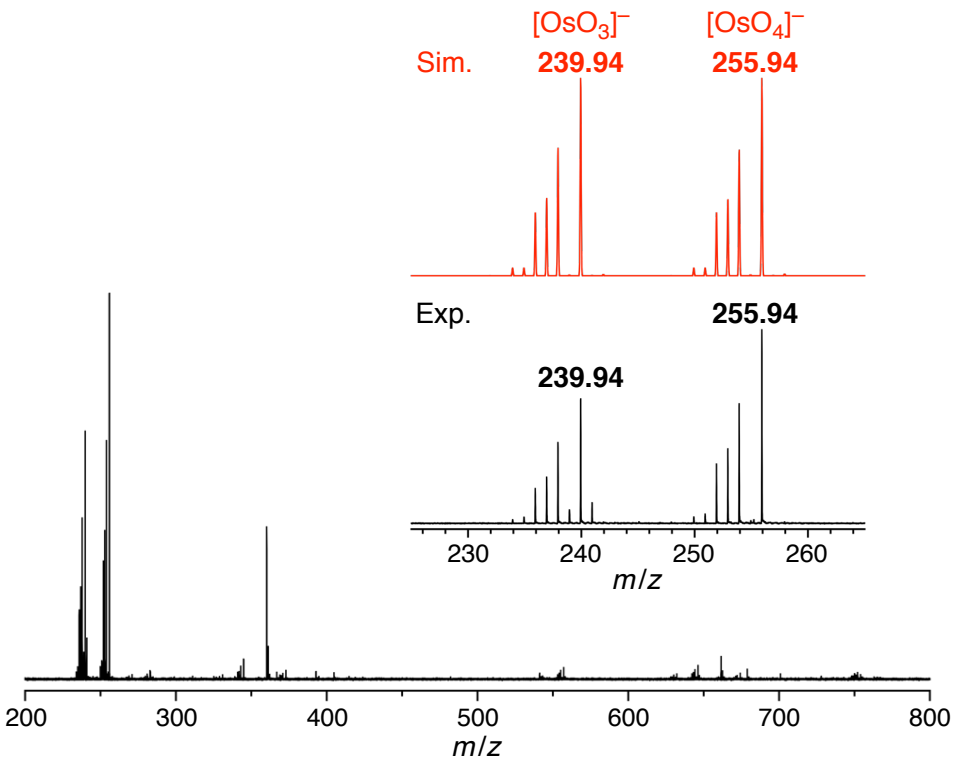

Figure 3-S6. ESI-MS of the resultant solution after the reaction of $\mathbf{1}^{\mathbf{OAc}}$ with xanthene.

Table 3-S1. Oxidation of xanthene by OsO_4, $\mathbf{1}^{\mathbf{OAc}}$, and $\mathbf{1}^{\mathbf{OBz}}$ in CH_3CN.

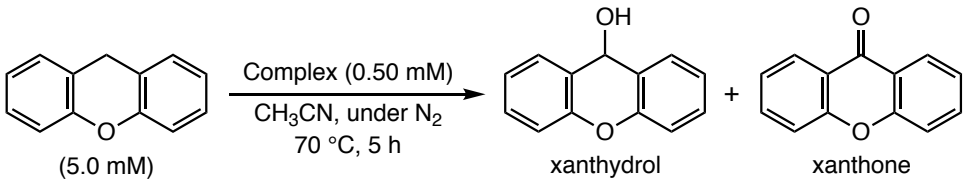

Complex	Yield, %	
	xanthydrol	xanthone
OsO_4	0	5
$\mathbf{1}^{\mathbf{OAc}}$	22	13
$\mathbf{1}^{\mathbf{OBz}}$	8	19

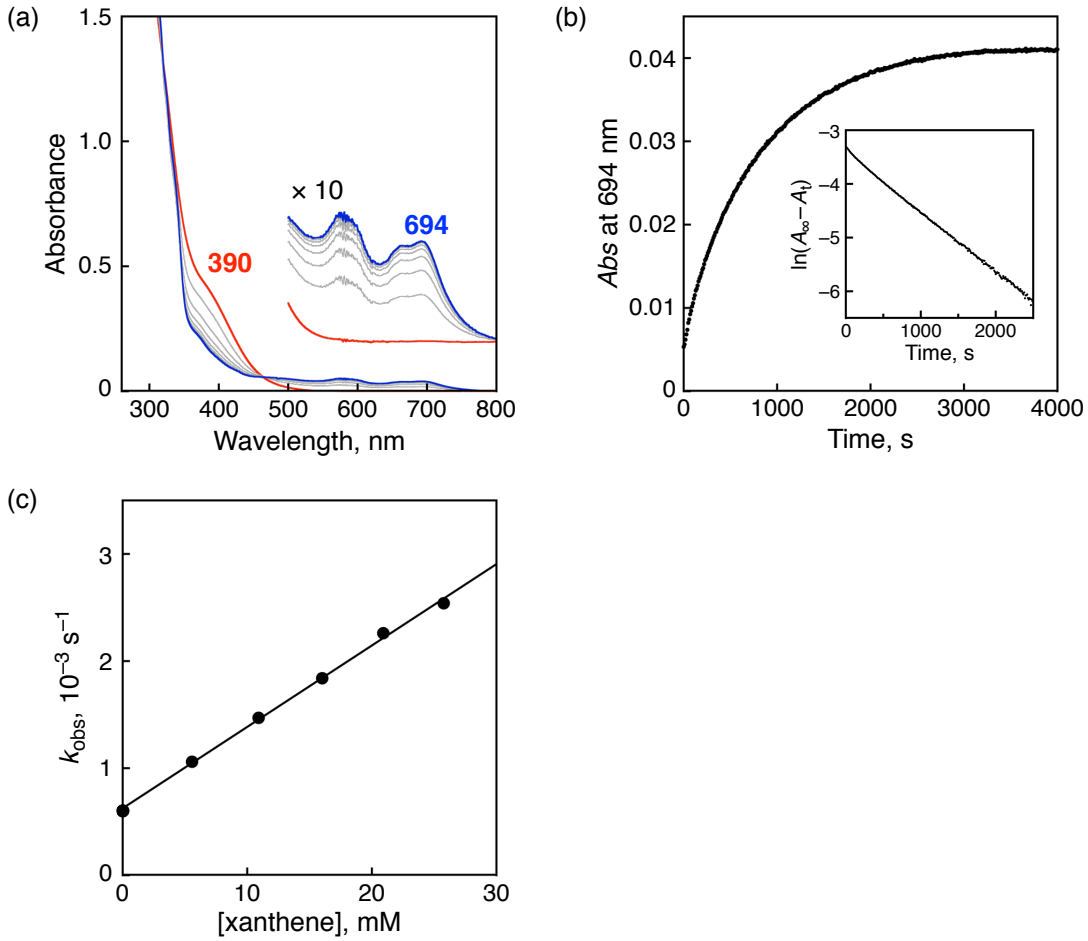

Figure 3-S7. (a) UV-vis spectral change of $\mathbf{1}^{\mathbf{OBz}}$ ($[OsO_4]_0$ = 0.5 mM, $[Bu_4NOBz]_0$ = 20 mM) observed upon addition of xanthene (5.0 mM) in CH_3CN at 70 °C under N_2 atmosphere. (b) The time course of the growth of Os^{VII} species monitored at 694 nm ([xanthene] = 5.0 mM). Inset: Plot of $\ln(A_\infty - A_t)$ against the reaction time. (c) Plot of k_{obs} against [xanthene].

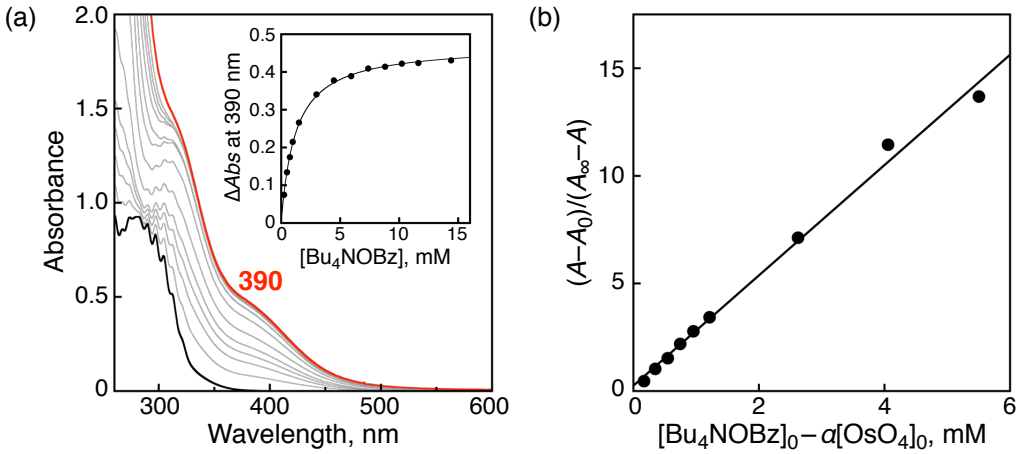

Figure 3-S8. (a) UV-vis spectral changes observed in the titration of OsO_4 by Bu_4NOBz at 70 °C. Inset: ΔAbs at 390 nm. (b) Plot of $(A–A_0)(A_\infty–A)$ against $[Bu_4NOBz]_0 – \alpha[OsO_4]_0$ according to equation (1) ($K_f^{OBz} = 1.0 \times 10^3$ M^{-1} at 70 °C in CH_3CN).

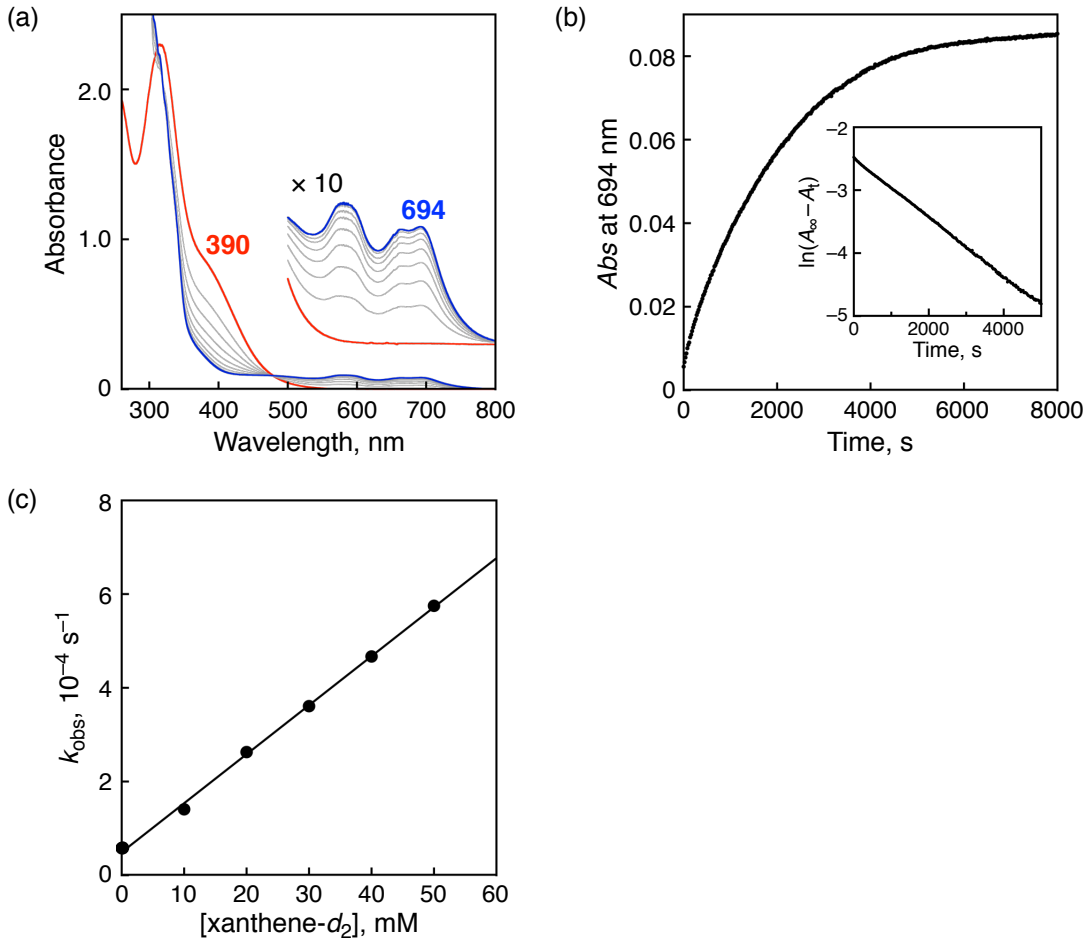

Figure 3-S9. (a) UV-vis spectral change of $\mathbf{1}^{\mathbf{OAc}}$ ($[OsO_4]_0$ = 1.0 mM, $[NBu_4OAc]_0$ = 20 mM) upon addition of xanthene-d_2 (40 mM) in CH_3CN at 70 °C under N_2 atmosphere. (b) The time course of the growth of Os^{VII} species monitored at 694 nm ([xanthene-d_2] = 40 mM). Inset: Plot of $\ln(A_\infty - A_t)$ against the reaction time. (c) The plot of k_{obs} against [xanthene-d_2].

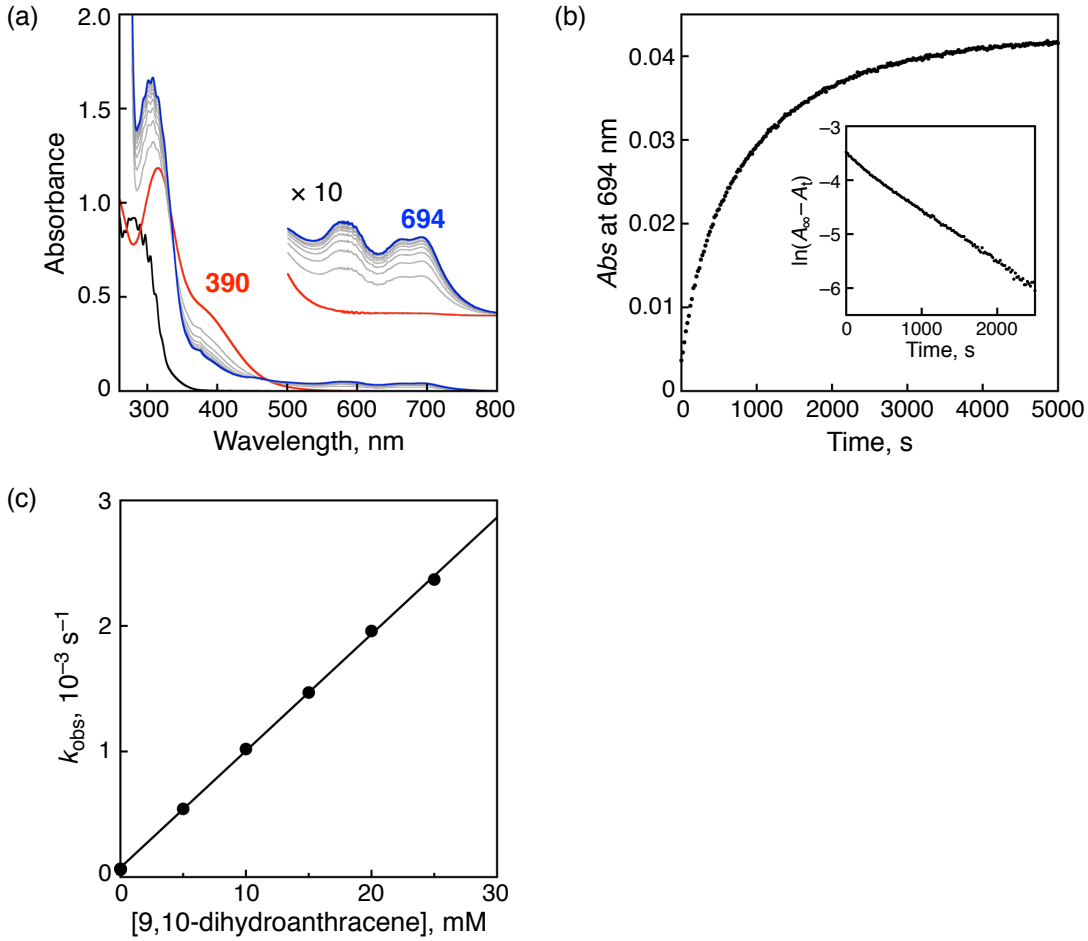

Figure 3-S10. (a) UV–vis spectral change of $\mathbf{1}^{\mathbf{OAc}}$ ($[OsO_4]_0$ = 1.0 mM, $[Bu_4NOAc]_0$ = 20 mM) upon addition of 9,10-dihydroanthracene (10 mM) in CH_3CN at 70 °C under N_2 atmosphere. (b) The time course of the growth of Os^{VII} species monitored at 694 nm ([9,10-dihydroanthracene] = 10 mM). Inset: Plot of $\ln(A_\infty - A_t)$ against the reaction time. (c) The plot of k_{obs} against [9,10-dihydroanthracene].

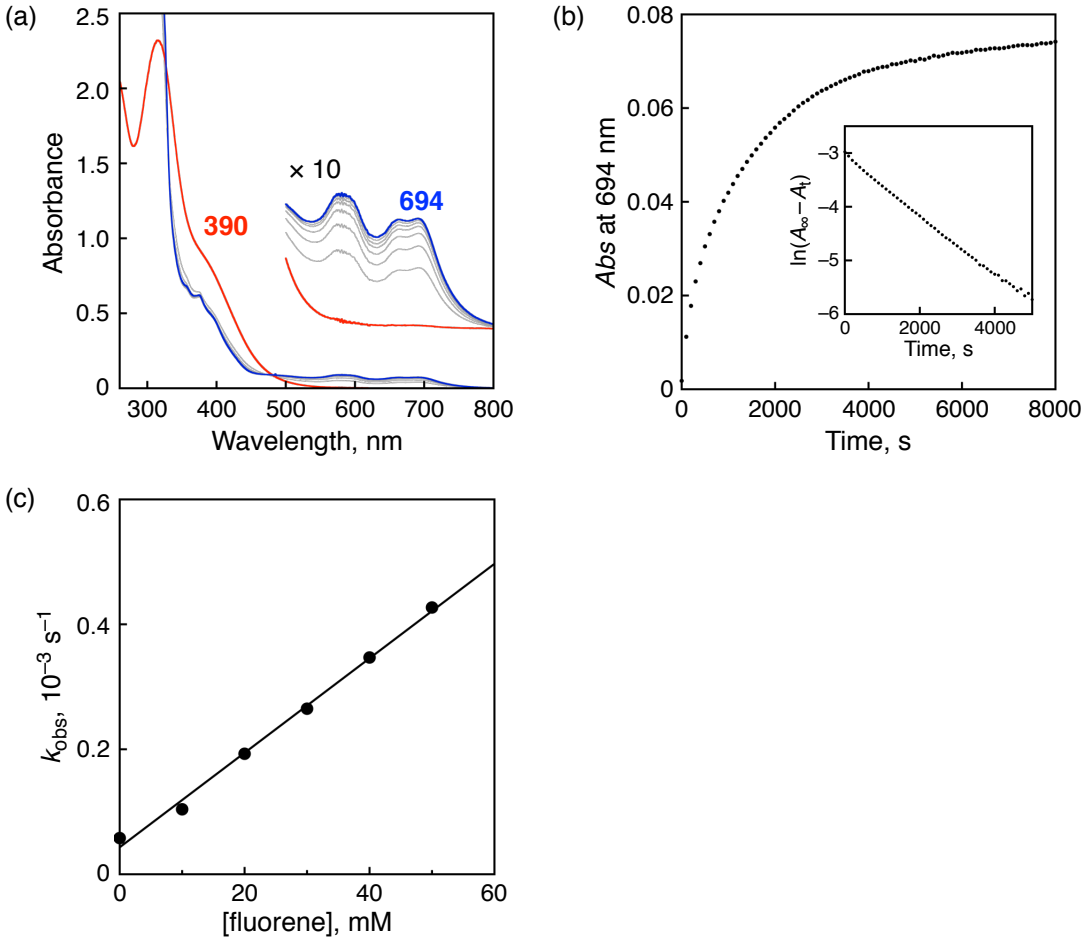

Figure 3-S11. (a) UV-vis spectral change of $\mathbf{1}^{\mathbf{OAc}}$ ($[OsO_4]_0$ = 1.0 mM, $[Bu_4NOAc]_0$ = 20 mM) upon addition of fluorene (50 mM) in CH_3CN at 70 °C under N_2 atmosphere. (b) The time course of the growth of Os^{VII} species monitored at 694 nm ([fluorene] = 50 mM). Inset: Plot of $\ln(A_\infty - A_t)$ against the reaction time. (c) The plot of k_{obs} against [fluorene].

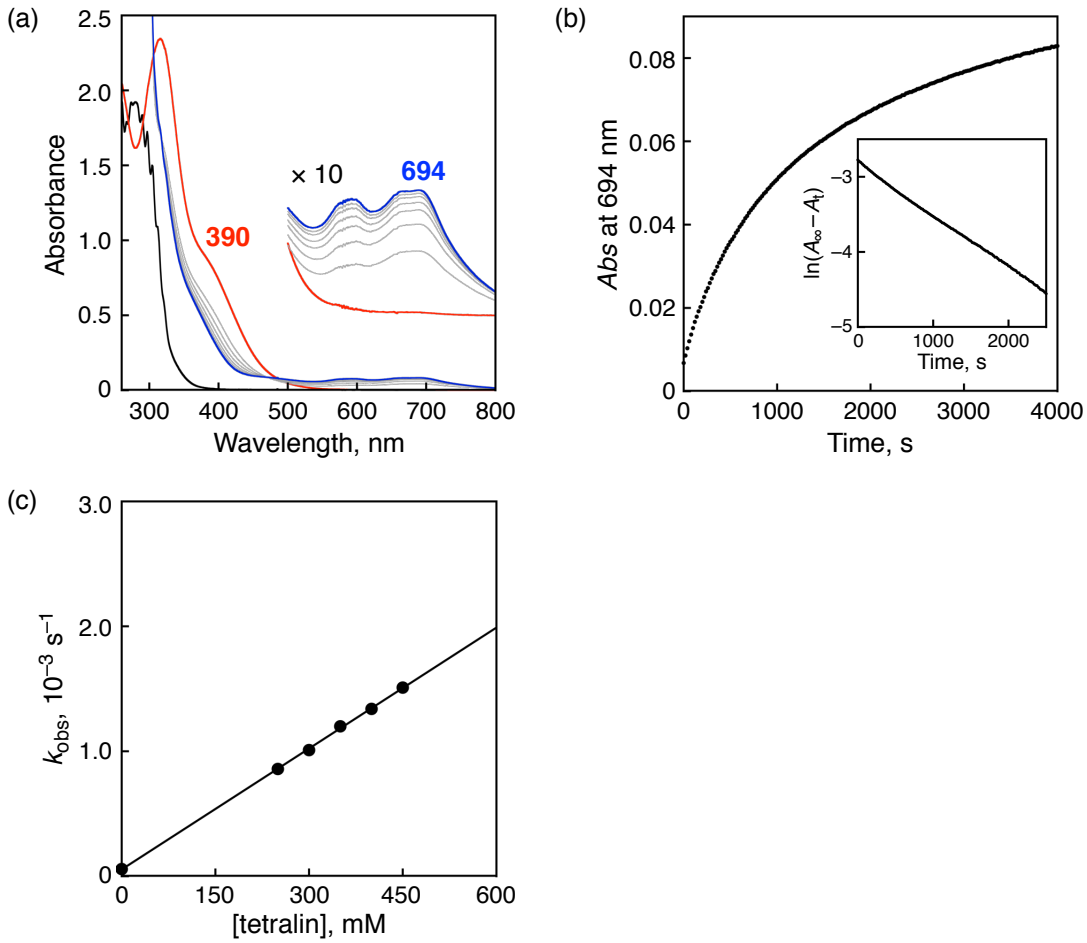

Figure 3-S12. (a) UV-vis spectral change of $\mathbf{1}^{\mathbf{OAc}}$ ($[OsO_4]_0$ = 1.0 mM, $[Bu_4NOAc]_0$ = 20 mM) upon addition of tetralin (250 mM) in CH_3CN at 70 °C under N_2 atmosphere. (b) The time course of the growth of Os^{VII} species monitored at 694 nm ([tetralin] = 250 mM). Inset: Plot of $\ln(A_\infty - A_t)$ against the reaction time. (c) The plot of k_{obs} against [tetralin].

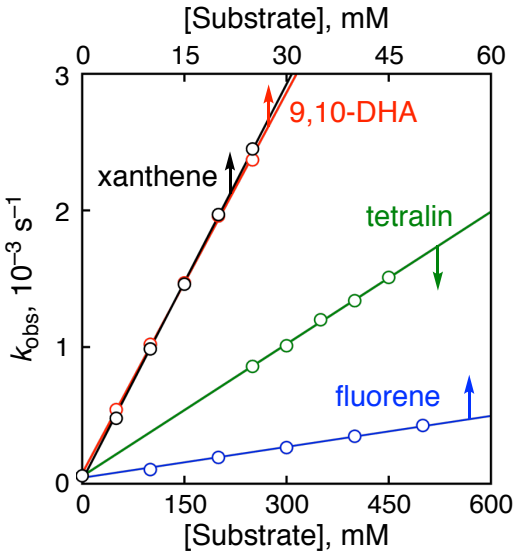

Figure 3-S13. The plot of k_{obs} against the concentration of the substrates.

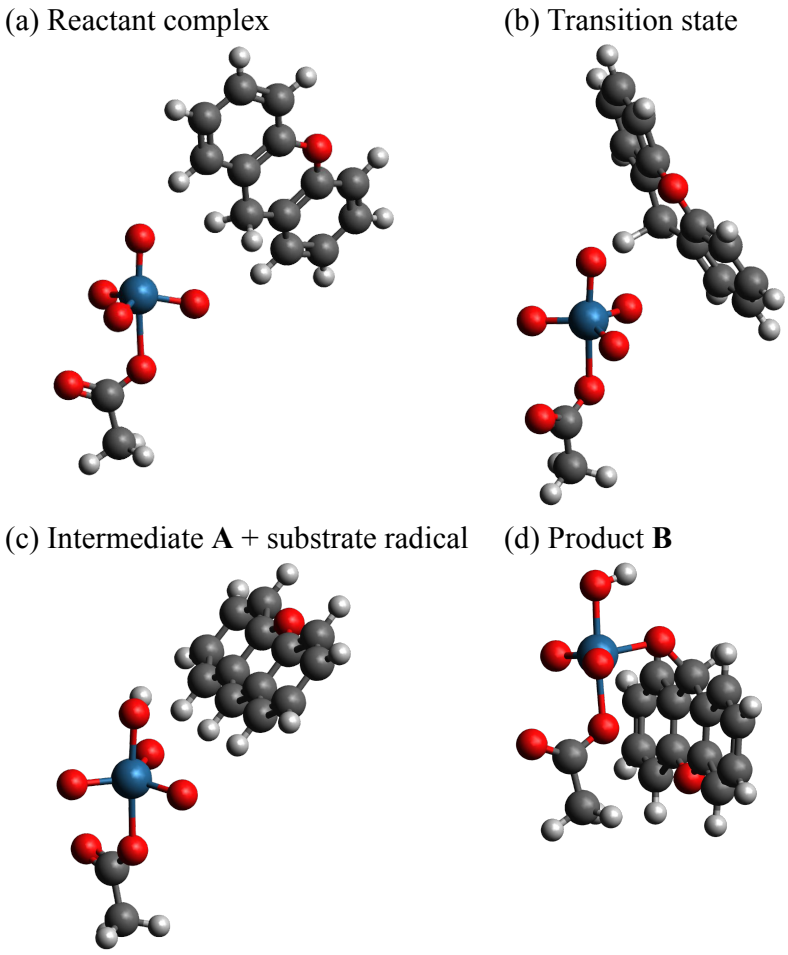

Figure 3-S14. DFT-calculated 3D-structures of (a) reactant complex, (b) the transition state, (c) intermediate **A** and substrate radical and (d) product **B**.

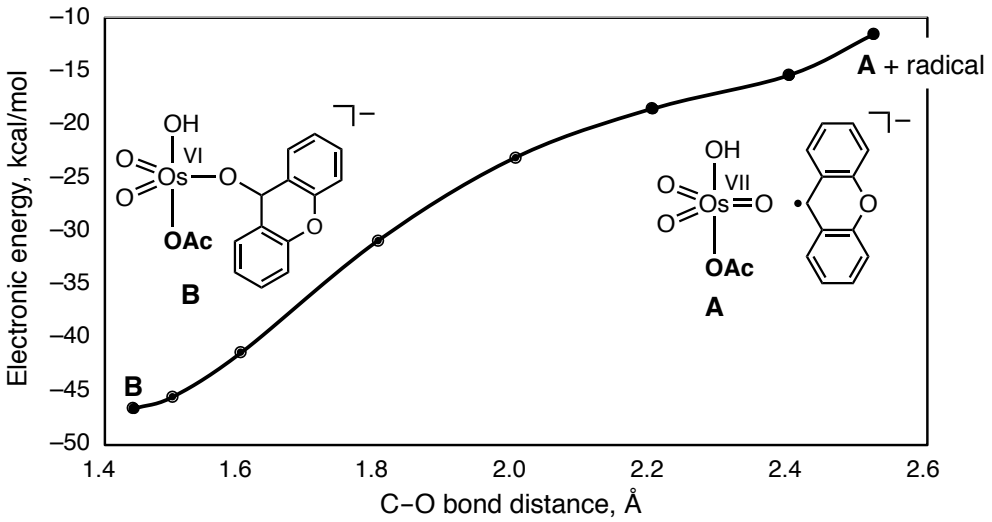

Figure 3-S15. Energy plots of relaxed scan calculations as a function of C-O distance.

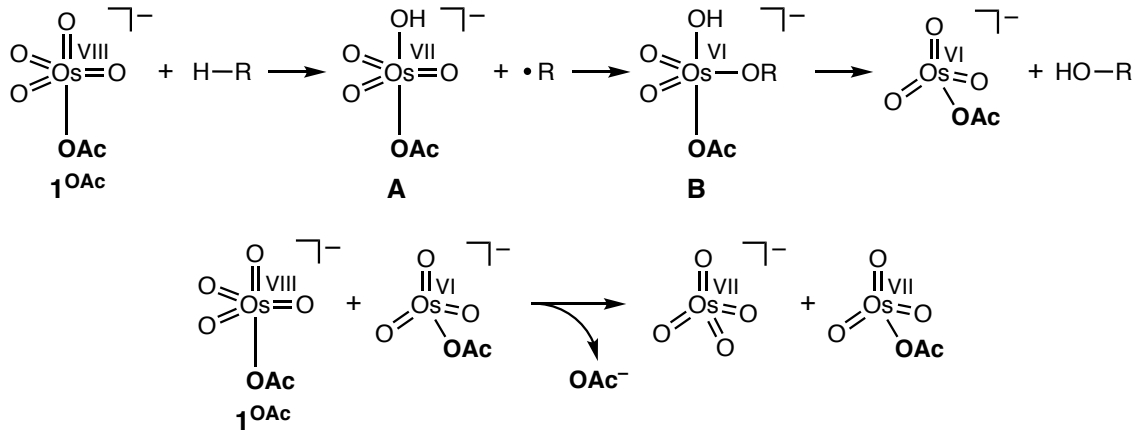

Scheme 3-S1. A possible mechanism for the generation of Os^{VII} products.

Chapter 4

Alkane Oxidation with H_2O_2 Catalyzed by OsO_4

Introduction

Selective alkane hydroxylation is an important process to obtain valuable alcohol products in synthetic organic chemistry and industrial chemistry.[1] However, transformation of the strong C(sp^3)–H bond of alkanes into the C–OH bond requires harsh conditions such as high temperature and high pressure. Under such conditions, over-oxidation of alcohol products occurs because alcohols are more easily oxidized compared to alkanes. Thus, it is highly desired to develop an efficient catalytic alkane hydroxylation system under mild conditions.

Metal oxides (MO_n) have been employed as the oxidant in a variety oxidation reaction.[2-7] Among transition metal oxides, osmium tetroxide (OsO_4) is single molecule adopting the highest oxidation state of +VIII and symmetric tetrahedral structure. It has long been known to catalyze *cis*-dihydroxylation of alkenes, where coordination of an amine or pyridine to the osmium center is demonstrated to enhance the catalytic activity (Scheme 4-1(a)).[8-15] On the other hand, the osmium-hydroxide adduct ($[OsO_4(OH)_n]^{n-}$), generated in an aqueous alkaline solution, can oxidize H_2 molecule to generate $[Os^{VI}(O)_2(OH)_4]^{2-}$ (Scheme 4-1(b)).[16, 17] However, structural characterization of the hydroxide-adduct has yet to be accomplished.

In Chapter 2, the author has demonstrated that osmium-halide adducts ($[OsO_4(X)]^-$, $X^- = Br^-$, Cl^-, and F^-) show higher reactivity in the alcohol oxidation reaction compared to OsO_4 itself (Scheme 4-1(c)).[18] Regarding to the alkane hydroxylation reaction

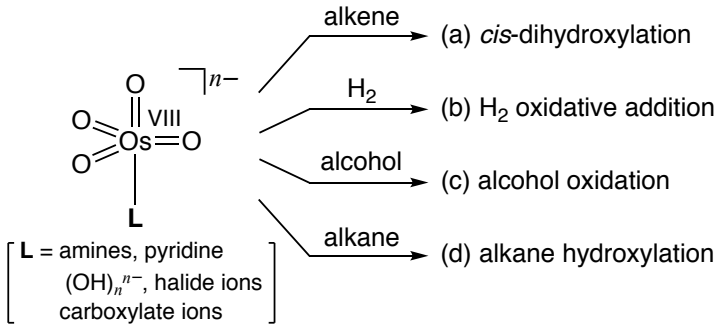

Scheme 4-1. Oxidation reactions with ligand-bound OsO_4 species ($[OsO_4(L)]^{n-}$) (n = 0, 1, 2).

((Scheme 4-1(d)), Mayer and co-workers reported that OsO_4 can induce oxygenation reaction of simple alkanes under an aqueous alkaline condition (pH = 12.1, at 85 °C for 7 days), where alkane substrates having a tertiary C–H bond (R_3C–H) are oxidized to the corresponding alcohols (R_3C–OH), whereas cyclic alkanes having secondary C–H bonds (R_2CH_2) such as cyclohexane and cyclopentane are converted to the ring-opened dicarboxylic acid derivatives.[19] They also reported oxidation of methane to methanol using an OsO_4/$NaIO_4$ system in water.[20] Although mechanistic details of such alkane oxygenation reactions have yet to be clarified, a hydroxide adduct of OsO_4, $[OsO_4(OH)]^-$, was proposed as an active oxidant in the alkane oxygenation reaction. The author also revealed that the distinct carboxylate adducts of OsO_4 ($[OsO_4(X)]^-$, X^- = AcO^- and BzO^-) exhibit much higher reactivity in the C(sp^3)–H bond activation reactions.[21] The author herein demonstrates that environmentally benign oxidant H_2O_2 can be employed as a re-oxidant in a catalytic alkane oxidation by the OsO_4/carboxylate system.

Experimental Section

General. The reagents and the solvents used in this study were commercial products of the highest available purity and further purified by the standard methods, if necessary.[22] UV-vis spectra were recorded on a Hewlett Packard 8453 photo diode array spectrometer or a Jasco V-650 spectrometer. A 0.10 M acetonitrile stock solution of OsO_4 was prepared by dissolving 1.0 g of OsO_4 (3.93 mmol) in 39.3 mL of acetonitrile and stored in a bottle with a screw cap. Gas chromatography (flame ionization detector (GC-FID)) measurements were performed on a Shimadzu GC-2010 equipped with GL Science InertCapWAX capillary column (30 m × 0.25 mm), an AOC-20s auto sampler, and an AOC-20i auto injector.

Oxidation of cyclohexane catalyzed by OsO_4. All procedures of the catalytic oxidation reactions were carried out under inert atmospheres (N_2) unless otherwise noted. The total volume of the reaction solution adjusted to 2.0 mL. The reaction was started by adding H_2O_2 (2.4 mmol) to an CH_3CN solution containing OsO_4 (1.6 μmol) and cyclohexane (2.4 mmol). The reaction conditions are shown in reaction scheme of Table 4-1. After quenching the reaction by passing the reaction mixture through a short column of NH_2-silica and treatment with excess amount of PPh_3, products were analyzed by using GC-FID. All peaks of interest were identified by comparing the retention times

with those of the authentic samples. The products were quantified by comparing their peak areas with that of an internal standard (nitrobenzene) using calibration curves consisting of plots of molar ratio (moles of organic compound / moles of internal standard) versus area ratio (area of organic compound / area of internal standard). Reaction conditions: [OsO_4] = 0.8 mM (1.6 μmol / 2.0 mL), [H_2O_2] = [cyclohexane] = 1.2 mM (2.4 mmol / 2.0 mL).

Coordinative anion effect on the oxidation reactivity of OsO_4. Before the catalytic reaction, CH_3CN solution of Bu_4NOBz (80 mM, 100 μL, 8.0 μmol) was added to 0.8 mM of OsO_4 solution to generate osmium-benzoate adduct, $[OsO_4(OBz)]^-$, *in situ*. In this case, the adduct is generated as >99% based on the formation constant determined in Chapter 3. After the generation of the adduct, the procedures of the catalytic oxidation reactions in the presence of benzoate anion were the same with the oxidation reaction by OsO_4 itself as described above.

Synthesis of mesoporous silica SBA-15(COOH). A carboxylate-functionalized mesoporous silica (SBA-15(COOH)) was prepared by similar manners for the previously reported one by Hikichi and co-workers.[23] 8.0 g of the surfactant Pluronic P123 (triblock copolymer $EO_{20}PO_{70}EO_{20}$ where EO = poly(ethylene oxide) and PO = poly(propylene oxide)) was placed in flask and then dissolved in 260 mL of water with 40 mL of conc. HCl solution (36 wt%) by stirring at 40 °C for 4 h. To the resulting solution, 18.2 mL (81.3 mmol) of tetraethoxysilane (TEOS) and 640 mg (0.82 mmol) of carboxyethylsilanetriol sodium salt (CES) were added. The mixture was stirred at 40 °C for 20 h and subsequently heated at 90 °C for 24 h. Once cooled, the solid product was filtered and washed with water and ethanol. The P123 surfactant was removed by Soxhlet extraction with a mixture of 200 mL of water and 200 mL of ethanol over a 72 h period. The resulting white solid was dried under vacuum to give 5.40 g of SBA-15(COOH).

Synthesis of OsO_4-immobilized mesoporous silica (Os-SBA-15(COOH)). SBA-15(COOH) (500 mg) and 15% hexane solution of ^{n}BuLi (500 μL, 0.80 mmol) were mixed in hexane (25 mL) and stirred for 2 h. The powder was collected by filtration and dried in vacuo. An OsO_4 stock solution (0.10 M, 1.60 mL, 0.16 mmol) was added to the treated SBA-15(COOH) (500 mg) in CH_3CN (15 mL). The heterogeneous suspension

changed in color from colorless to gray. The mixture was stirred at 30 °C for 24 h, and then filtered to give gray powder (500.6 mg) and colorless filtrate. The presence of 0.20 μmol of OsO_4 in the filtrate was determined by ε value of OsO_4 at 304 nm (ε = 1500 M^{-1} cm^{-1}) with UV-vis spectrum, indicating that 159.8 (160 – 0.20) μmol of OsO_4 was used in immobilization on the surface. Thus, the loaded OsO_4 on SBA-15(COOLi) was 0.32 mmol/g (159.8 μmol / 500.6 mg). The obtained Os-SBA-15(COOLi) (100 mg) was treated with acetic acid (4.0 mL) in CH_3CN (15 mL). After stirring for 5 min, the protonated silica, Os-SBA-15(COOH), was collected by filtration. UV-vis analysis of the filtrate showed the absence of OsO_4, indicating no elution of OsO_4 during the AcOH treatment.

Oxidation of cyclohexane catalyzed by OsO_4-immobilized silica (Os-SBA15(COOH)). The amount of Os-SBA-15(COOH) used in the reaction was determined by loading amount of OsO_4 determined above. To obtain 0.8 μmol of OsO_4 in the silica, 2.53 mg of Os-SBA-15(COOH) was employed (0.32 mmol/g × 2.53 mg = 0.80 μmol). The total volume of the reaction solution is 1.0 mL, which is a half compared to the homogeneous system. The procedures of the catalytic oxidation reaction by Os-SBA-15(COOH) were almost the same with the oxidation reaction by OsO_4 itself as described above. Reaction conditions: [OsO_4 (in Os-SBA-15)] = 0.8 μmol / 1.0 mL, [H_2O_2] = [cyclohexane] = 1.2 M (1.2 mmol / 1.0 mL) in CH_3CN.

Results and Discussion

First of all, oxidation of cyclohexane with H_2O_2 in the presence of a catalytic amount of OsO_4 was examined at 30 °C in CH_3CN under N_2 (Table 4-1). After 3 h, the reaction mixture was directly analyzed by GC-FID to show the formation of cyclohexanol (**A**) and cyclohexanone (**K**) in 25.6 and 32.0 μmol, respectively (entry 1). When the post reaction mixture was treated with PPh_3 before the GC-FID analysis, the product distribution differed significantly to give **A** as the major product (91.2 mmol) together with a small amount of **K** (3.2 mmol) (entry 2). These results indicated that the primary product was cyclohexyl hydroperoxide (**P**), and **A** and **K** were generated from **P** during the GC-FID analysis in entry 1.[24] It is well known that the treatment of **P** with PPh_3 gives **A** selectively.[25, 26] A blank experiment without OsO_4 or H_2O_2 didn't produce any oxidation products, confirming that both reagents are essential for the catalytic reaction (entries 3 and 4). The remaining H_2O_2 in the final reaction solution was determined as 83% by a titration experiment using I_3^-,[27] which confirmed that 17% (0.41 mmol) of the added H_2O_2 was consumed during the reaction (Figure 4-S1). This means that the oxidant efficiency is 24% and the rest of H_2O_2 decomposed to H_2O and O_2 as a side reaction (catalase reaction).[28, 29] The advantages of the present reaction compared to the Mayer's OsO_4/$NaIO_4$ system are as follows.[19] (1) Environmentally benign H_2O_2, can

Table 4-1. Oxidation of cyclohexane with H_2O_2 by OsO_4.

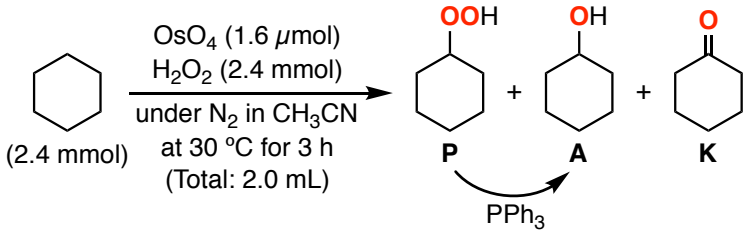

Entry	Product, mM (μmol)[a]		Alcohol selctivity (**A**/**K**)
	A	**K**	
1	12.8 (25.6)	16.0 (32.0)	0.8
2[b]	45.6 (91.2)	1.6 (3.2)	29
3[c]	n.d.	n.d.	—
4[d]	n.d.	n.d.	—

[a] Oxidation products were determined by GC-FID. [b] PPh_3 was added after the reaction (before GC-FID analysis). [c] without OsO_4. [d] without H_2O_2.

be used as a re-oxidant instead of $NaIO_4$. (2) **A** is selectively obtained from **P** by the easy work-up treatment using PPh_3. (3) The reaction conditions are significantly milder (85 °C, 7 days vs. 30 °C, 3 hours).

To see the effect of O_2 generated by the decomposition of H_2O_2 on the current catalytic reaction, a reaction was carried out under continuous N_2 bubbling conditions. Exclusion of generated O_2 from the reaction vessel resulted in a significant decrease of **A**/**K** ratio from 28.5 (91.2 μmol /3.2 μmol) to 5.6 (11.2 mmol /2.0 mmol) even after the PPh_3 treatment, indicating that oxygen atom of **A** is derived from O_2 generated from H_2O_2. The catalytic reaction conducted under air gave almost the same results as those shown in entry 2 [**A**: 44.2 mM (88.4 μmol), **K**: 2.6 mM (5.2 μmol)]. Furthermore, addition of trichlorobromomethane (CCl_3Br) as a radical trap reagent[30-32] in the catalytic reaction under the same condition of entry 2 gave bromocyclohexane (17.6 μmol) together with **A** (1.6 μmol) and **K** (3.2 μmol). Formation of bromocyclohexane clearly indicated generation of cyclohexyl radical intermediate (C_6H_{11}•) *via* hydrogen atom abstraction by an active oxidant derived from OsO_4 as shown in Scheme 4-2. The generated radical intermediate is trapped by CCl_3Br to give bromocyclohexane. Under the general reaction conditions (entry 1), C_6H_{11}• rapidly reacts with O_2 at a rate of ~10^9 M^{-1} s^{-1} to generate cyclohexyl peroxyl radical species ($C_6H_{11}OO$•) (Scheme 4-2).[33] Hydrogen atom abstraction by $C_6H_{11}OO$• from a hydrogen atom donor reagent generates cyclohexyl hydroperoxide **P**. Judging from the bond dissociation energy of the C–H bond of cyclohexane (BDE_{C-H} = 99.5 kcal/mol) and that of the O–H bond of H_2O_2 (BDE_{O-H} = 87.5 kcal/mol),[34] H_2O_2 is more likely as the hydrogen atom donor rather than cyclohexane (Scheme 4-2). Hydroperoxyl radical (HOO•) thus generated may disproportionate to

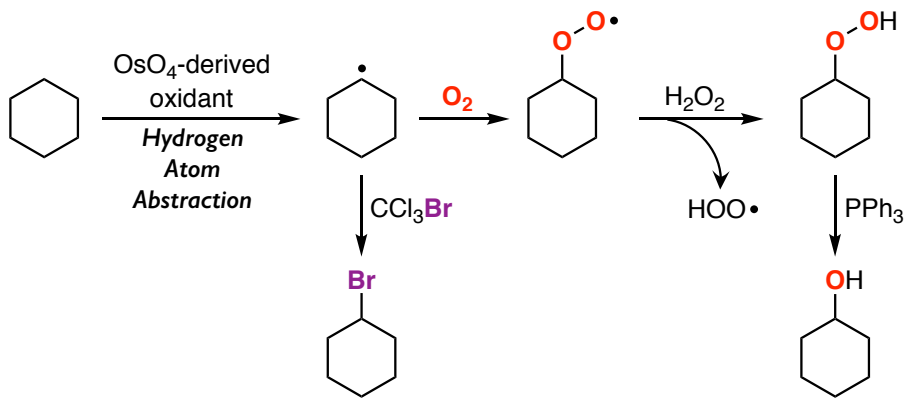

Scheme 4-2. Possible reaction mechanism of the oxidation of cyclohexane.

H_2O_2 and O_2 (catalase reaction).[35] As mentioned above, **P** is converted to **A** by the workup treatment using PPh_3. In the present catalytic oxidation reaction, other hydroperoxides such as *tert*-butyl and cumene hydroperoxide did not work at all (Table 4-S1).

In Chapter 3, the author has found that a carboxylate adduct of OsO_4 such as $[OsO_4(OBz)]^-$ (OBz = benzoate) exhibits a higher reactivity compared to OsO_4 itself in C(sp^3)–H bond activation reaction.[21] Thus, the author next examined the effect of carboxylate anion in the present catalytic reaction. In Figure 4-1 is shown the time courses of product formation in the presence (red line) and the absence (black line) of Bu_4NOBz. As clearly seen, the oxidation rate is significantly accelerated upon the addition of benzoate anion by 14 times (v_{obs} = 0.88 mM/min → 12.4 mM/min). In Chapter 3, the author also demonstrated that the acetate adduct $[OsO_4(OAc)]^-$ can induce direct activation of benzylic C–H bonds (BDE is less than 82.5 kcal/mol) to give oxygenated products.[21] However, the author could not observe direct oxidation of cyclohexane (BDE_{C-H} = 99.5 kcal/mol) by $[OsO_4(OBz)]^-$ under the reaction conditions employed here. Thus, clarification of the real active oxidant needs to further investigations.

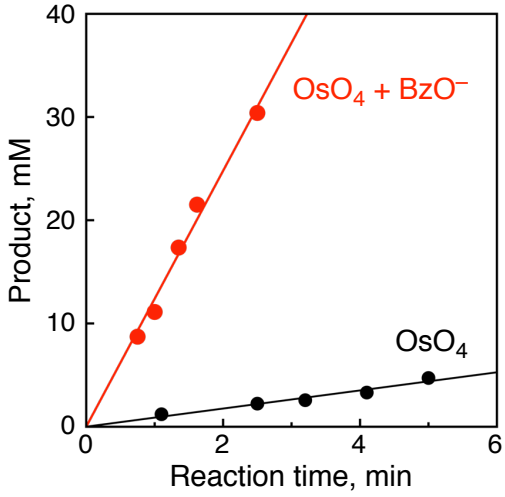

Figure 4-1. Time courses of product formation (**A** + 2**K** obtained after PPh_3 treatment) at the initial stage of the oxidation of cyclohexane (2.4 mmol) with H_2O_2 (2.4 mmol) and OsO_4 (1.6 mmol) in the absence (black) and the presence of BzO^- (8.0 μmol, red) in CH_3CN at 30 °C.

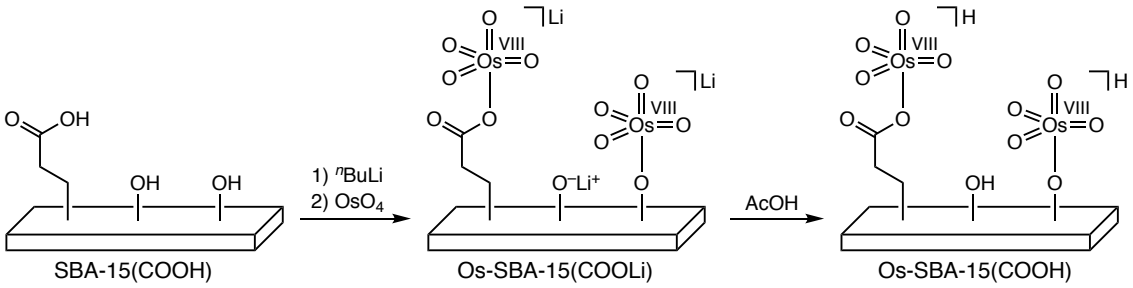

Scheme 4-3. Synthesis of OsO_4-immoblized mesoporous silica (Os-SBA-15(COOH)).

Taking advantage of the enhancement of catalytic activity of OsO_4 by benzoate addition, the author developed a heterogeneous catalyst by immobilizing OsO_4 on SBA-15(COOH) mesoporous silica containing carboxylic acid functional groups on the surface[36-38] according to a procedure illustrated in Scheme 4-3. Thus, OsO_4 is immobilized on the silica surface by reacting with the silica pretreated with ^{n}BuLi. Then, the Os-SBA-15(COOLi) is washed with acetic acid to protonate the remained hydroxylate groups. The detail synthetic procedures are described in Experimental Section. Immobilization of OsO_4 onto the surface through the carboxylate-Os bond was confirmed by the reflectant spectrum, where a characteristic absorption band due to $[OsO_4(OCOR)]^-$ species appeared as shown in Figure 4-2. Since the band around 303 nm is characteristic of the electronic spectrum of the isolated $[OsO_4(OBz)]^-$ but not of OsO_4 itself (Inset of Figure 4-2), appearance of the band indicates that OsO_4 was immobilized on SBA-15(COOH) through the coordination with the carboxylate functional group.[21] The broad peak around 520 nm may be due to a Os^{VII} and/or Os^{VI} species generated by reduction of

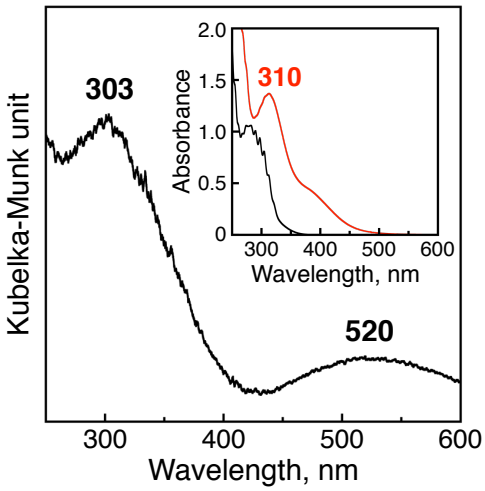

Figure 4-2. UV-vis reflection spectra of Os-SBA-15(COOH). Inset: UV-vis spectra of OsO_4 (black) and $[OsO_4(OBz)]^-$ (red) in CH_3CN.

$Os^{VIII}O_4$ during the preparation process.[18, 39] The amount of the loaded OsO_4 on the surfaces was estimated by dividing the amounts of OsO_4 used in immobilization by weight of the obtained powders (see Experimental Section).

The catalytic activity of the OsO_4-immobilized silica (Os-SBA-15(COOH)) in the oxidation of cyclohexane with H_2O_2 was examined. In this reaction, 2.53 mg of Os-SBA-15(COOH) was employed, so that the amount of OsO_4 was 0.8 μmol (0.32 mmol/g × 2.53 mg = 0.8 μmol). In Figure 4-3 are shown the time courses of the product formation for the cyclohexane oxidation with H_2O_2 using (a) OsO_4, (b) OsO_4-OBz, and (c) Os-SBA-15(COOH) as the catalyst. As mentioned above (Figure 4-1), the initial rate of the OsO_4-OBz system was much higher than that of OsO_4 only system. However, in the former reaction with OsO_4-OBz, the catalytic reaction stopped after about 1 h. This is due to consumption of all H_2O_2 added. Namely, OsO_4-OBz also enhance the catalase reaction (decomposition of H_2O_2 to H_2O and O_2). On the other hand, such a catalase activity was significantly depressed in the case of Os-SBA-15(COOH) and the reaction proceeded continuously even after 6 h, so that the amount of product (204.8 mM) was much higher than those of other systems.

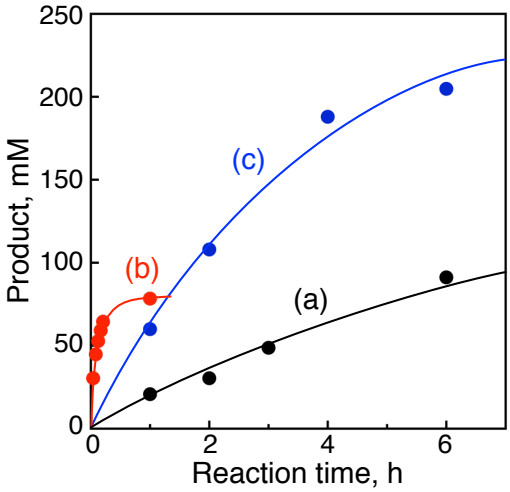

Figure 4-3. Time courses of product formation in the oxidation of cyclohexane (1.2 mM) with H_2O_2 (1.2 mM) catalyzed by (a) OsO_4 (0.8 mM), (b) OsO_4-OBz (0.8 mM), and (c) Os-SBA-15(COOH) (0.8 mM) in CH_3CN at 30 °C.

Conclusions

In Chapter 4, oxidation of cyclohexane with H_2O_2 catalyzed by OsO_4 and its carboxylate adducts was examined. Cyclohexyl hydroperoxide (**P**) was selectively obtained, which was converted to cyclohexanol (**A**) by the workup treatment using PPh_3. The catalytic reactivity was significantly enhanced by the addition of benzoate anion. This result suggests that osmium-benzoate adduct has higher oxidation ability than OsO_4 itself toward catalytic alkane oxidation as observed in Chapter 3.[21] Furthermore, an OsO_4-immobilized heterogeneous catalyst was developed by immobilizing OsO_4 on the mesoporous silica, SBA-15(COOH), through the coordination of the carboxylate functional groups on the surface. The Os-immobilized catalyst showed good catalytic performance compared to OsO_4 and its benzoate adduct. Namely, immobilization of OsO_4 on coordinative ligand on the solid surface was found to be effective for enhancement of the catalytic activity of OsO_4 and depression of the catalase activity. This is the first example of the efficient alkane oxidation system with using environmentally benign oxidant H_2O_2 and the carboxylate adducts of OsO_4 as the catalyst. Mechanistic details are now under investigation to improve the catalytic efficiency.

References

1. *Advanced Organic Chemistry*: Part B: Reactions and Synthesis, 5th ed., ed. by F. Carey, R. Sundberg, Springer-Verlag, New York, **2007**.
2. F. H. Westheimer, A. Novick, *J. Chem. Phys*. **1943**, *11*, 506-512.
3. K. Bowden, I. M. Heilbron, E. R. H. Jones, B. C. L. Weedon, *J. Chem. Soc*. **1946**, 39-45.
4. R. U. Lemieux, E. V. Rudloff, *Can. J. Chem*. **1955**, *33*, 1701-1709.
5. K. B. Wiberg, K. A. Saegebarth, *J. Am. Chem. Soc*. **1957**, *79*, 2822-2824.
6. V. Duma, D. Hönicke, *J. Catal*. **2000**, *191*, 93-104.
7. F. Shi, M. K. Tse, M.-M. Pohl, A. Brückner, S. Zhang, M. Beller, *Angew. Chem., Int. Ed*. **2007**, *46*, 8866-8868.
8. V. VanRheenen, R. C. Kelly, D. Y. Cha, *Tetrahedron Lett*. **1976**, *17*, 1973-1976.
9. S. G. Hentges, K. B. Sharpless, *J. Am. Chem. Soc*. **1980**, *102*, 4263-4265.
10. M. Tokles, J. K. Snyder, *Tetrahedron Lett*. **1986**, *27*, 3951-3954.
11. E. N. Jacobsen, I. Marko, M. B. France, J. S. Svendsen, K. B. Sharpless, *J. Am*.

Chem. *Soc*. **1989**, *111*, 737-739.

12. S. Hanessian, P. Meffre, M. Girard, S. Beaudoin, J. Y. Sanceau, Y. Bennani, *J*. *Org*. *Chem*. **1993**, *58*, 1991-1993.
13. H. C. Kolb, P. G. Andersson, Y. L. Bennani, G. A. Crispino, K. S. Jeong, H. L. Kwong, K. B. Sharpless, *J*. *Am*. *Chem*. *Soc*. **1993**, *115*, 12226-12227.
14. E. J. Corey, S. Sarshar, M. D. Azimioara, R. C. Newbold, M. C. Noe, *J*. *Am*. *Chem*. *Soc*. **1996**, *118*, 7851-7852.
15. D. W. Nelson, A. Gypser, P. T. Ho, H. C. Kolb, T. Kondo, H.-L. Kwong, D. V. McGrath, A. E. Rubin, P.-O. Norrby, K. P. Gable, K. B. Sharpless, *J*. *Am*. *Chem*. *Soc*. **1997**, *119*, 1840-1858.
16. A. Dehestani, W. H. Lam, D. A. Hrovat, E. R. Davidson, W. T. Borden, J. M. Mayer, *J*. *Am*. *Chem*. *Soc*. **2005**, *127*, 3423-3432.
17. J. M. Mayer, E. A. Mader, J. P. Roth, J. R. Bryant, T. Matsuo, A. Dehestani, B. C. Bales, E. J. Watson, T. Osako, K. Valliant-Saunders, W. H. Lam, D. A. Hrovat, W. T. Borden, E. R. Davidson, *J*. *Mol*. *Catal*. *A* **2006**, *251*, 24-33.
18. T. Fujimoto, Y. Hirata, H. Sugimoto, M. Miyanishi, Y. Shiota, K. Yoshizawa, S. Itoh, *Bull*. *Chem*. *Soc*. *Jpn*. **2022**, *95*, 64-72.
19. B. C. Bales, P. Brown, A. Dehestani, J. M. Mayer, *J*. *Am*. *Chem*. *Soc*. **2005**, *127*, 2832-2833.
20. T. Osako, E. J. Watson, A. Dehestani, B. C. Bales, J. M. Mayer, *Angew*. *Chem*., *Int*. *Ed*. **2006**, *45*, 7433-7436.
21. T. Fujimoto, Y. Hirata, H. Sugimoto, M. Miyanishi, Y. Shiota, K. Yoshizawa, S. Itoh, *Dalton Trans*., **2022**, *51*, 1123-1130.
22. N. Bernier, S. Carvalho, F. Li, R. Delgado, V. Félix, *J*. *Org*. *Chem*. **2009**, *74*, 4819-4827.
23. T. Tsuruta, T. Yamazaki, K. Watanabe, Y. Chiba, A. Yoshida, S. Naito, J. Nakazawa, S. Hikichi, *Chem*. *Lett*. **2014**, *44*, 144-146.
24. G. B. Shul'pin, *J*. *Mol*. *Catal*. *A* **2002**, *189*, 39-66.
25. I. Garcia-Bosch, M. A. Siegler, *Angew*. *Chem*., *Int*. *Ed*. **2016**, *55*, 12873-12876.
26. J. Gu, M. Wen, Y. Cai, Z. Shi, A. S. Arol, M. V. Kirillova, A. M. Kirillov, *Inorg*. *Chem*. **2019**, *58*, 2403-2412.
27. S. Fukuzumi, S. Kuroda, T. Tanaka, *J*. *Am*. *Chem*. *Soc*. **1985**, *107*, 3020-3027.

28. R. F. Beers, I. W. Sizer, *J. Biol. Chem.* **1952**, *195*, 133-140.
29. S.-i. Yamazaki, C. Morioka, S. Itoh, *Biochemistry* **2004**, *43*, 11546-11553.
30. J. T. Groves, T. E. Nemo, *J. Am. Chem. Soc.* **1983**, *105*, 6243-6248.
31. L. M. Slaughter, J. P. Collman, T. A. Eberspacher, J. I. Brauman, *Inorg. Chem.* **2004**, *43*, 5198-5204.
32. O. V. Nesterova, D. S. Nesterov, J. Jezierska, A. J. L. Pombeiro, A. Ozarowski, *Inorg. Chem.* **2018**, *57*, 12384-12397.
33. B. Maillard, K. U. Ingold, J. C. Scaiano, *J. Am. Chem. Soc.* **1983**, *105*, 5095-5099.
34. *Comprehensive Handbook of Chemical Bond Energies*, ed. by Y.-R. Luo, CRC Press, Boca Raton, **2007**.
35. Y. N. Kozlov, A. D. Nadezhdin, A. P. Pourmal, *Int. J. Chem. Kinet.* **1974**, *6*, 383-394.
36. C.-M. Yang, B. Zibrowius, F. Schüth, *Chem. Commun.* **2003**, 1772-1773.
37. C.-T. Tsai, Y.-C. Pan, C.-C. Ting, S. Vetrivel, A. S. T. Chiang, G. T. K. Fey, H.-M. Kao, *Chem. Commun.* **2009**, 5018-5020.
38. S. Ganji, P. Bukya, Z.-W. Liu, K. S. R. Rao, D. R. Burri, *New J. Chem.* **2019**, *43*, 11871-11875.
39. K. A. K. Lott, M. C. R. Symons, *J. Chem. Soc.* **1960**, 973-976.

Supporting Information for Chapter 4

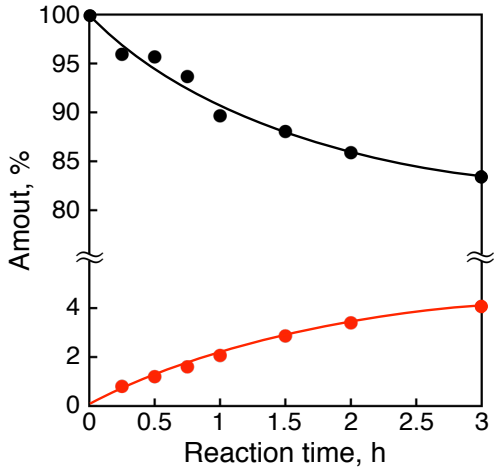

Figure 4-S1. Time courses of the amounts of H_2O_2 remained (black) and the oxidation products generated (red).

Table 4-S1. Activity comparison of peroxides as re-oxidant in cyclohexane oxidation catalyzed by OsO_4.

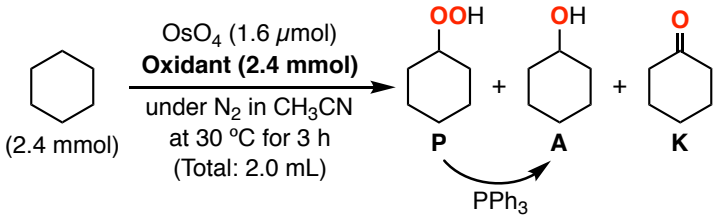

Oxidant	Product, mM (μmol)[a]		Alcohol selctivity (**A**/**K**)
	A	**K**	
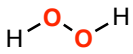	45.6 (91.2)	1.6 (3.2)	29
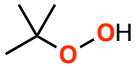	trace	trace	—
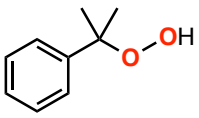	trace	trace	—

[a] Oxidation products were determined by GC-FID.

General Conclusion

In this thesis, the author describes his studies on controlling of oxidation reactivity of an osmium complex supported by an N4-tetradentate ligand and osmium tetroxide (OsO_4) coordinated by an anionic external ligand. In particular, the author focuses his attention on supporting ligand effects on the structure and reactivity of the reactive intermediates of alkene *cis*-dihydroxylation and *cis*-aminohydroxylation reactions and on the effects of valent and structural changes of OsO_4 on its oxidation reactivity in the presence of the anionic ligands. Moreover, the author develops an efficient OsO_4-catalyzed alkane oxidation system using mild H_2O_2 oxidant. The results and findings in this work are summarized as follows.

In Chapter 1, the author has demonstrated that an osmium(III) complex derived from OsO_4 and an N4-tetradentate ligand catalyzes selective *cis*-dihydroxylation and *cis*-aminohydroxylation of alkenes. The reactive intermediates in these reactions are successfully isolated and the ligand effects are explored in detail.

In Chapter 2, halide-adducts of OsO_4 have been synthesized and their structures have been determined by X-ray crystallographic analysis. These adducts have been found to show higher oxidation reactivity in alcohol oxidation compared to OsO_4 itself. Enhancement of the reactivity of OsO_4 is discussed based on the results of kinetic analysis and DFT calculations.

In Chapter 3, reactivity of the carboxylate adducts of OsO_4 toward C(sp^3)–H bond activation has been investigated. Based on the kinetic and computational studies, the author proposes a new mechanism where an oxido group in the axial position in the adduct works as a hydrogen atom abstractor and another oxido group in the equatorial position works an oxygen source in the oxidation of the substrates.

Finally, in Chapter 4, oxidation of cyclohexane with H_2O_2 catalyzed by OsO_4 has been examined. The corresponding alcohol was selectively obtained after the PPh_3 treatment. Enhancement of the catalytic activity of OsO_4 by adding the anionic ligands has also been demonstrated. This strategy has been adopted to the development of heterogeneous catalysts. Combining OsO_4 and carboxylate containing mesoporous silica provided efficient catalysts for the catalytic alkane oxidation.

These new findings described in this thesis add new insights into the chemistry of OsO_4 and greatly contribute to the development of efficient catalytic oxidation reactions using OsO_4.

List of Publications

1. Oxido-Hydroxido- and Oxido-Aminato-Osmium(V) Complexes with a Cyclohexanediamine-Based Tetradentate Ligand as Active Oxidants for Dihydroxylation and Aminohydroxylation of Alkenes
   Tomohiro Fujimoto, Hideki Sugimoto, Kenichiro Kai, Kazuki Maeda, and Shinobu Itoh.
   Eur. J. Inorg. Chem., **2019**, 2891-2898.

2. Halide-Adducts of OsO_4. Structure and Reactivity in Alcohol-Oxidation
   Tomohiro Fujimoto, Yuka Hirata, Hideki Sugimoto, Mayuko Miyanishi, Yoshihito Shiota, Kazunari Yoshizawa, and Shinobu Itoh
   Bull. Chem. Soc. Jpn., **2022**, *95*, 64-72.

3. C(sp^3)–H bond activation by the carboxylate-adduct of osmium tetroxide (OsO_4)
   Tomohiro Fujimoto, Yuka Hirata, Hideki Sugimoto, Mayuko Miyanishi, Yoshihito Shiota, Kazunari Yoshizawa, and Shinobu Itoh
   Dalton Trans., **2022**, *51*, 1123-1130.

4. Alkane Oxidation with H_2O_2 Catalyzed by OsO_4-carboxylate Adduct and Its Application to Heterogeneous Catalyst
   Tomohiro Fujimoto, Yuta Ueda, Hideki Sugimoto, Jun Nakazawa, Shiro Hikichi, and Shinobu Itoh
   Chem. Lett., in press (doi:10.1246/cl.210751).

Acknowledgement

The studies presented in this thesis have been carried out under the guidance of Professor Shinobu Itoh at Osaka University during 2016–2022.

The author would like to express his gratitude to Professor Shinobu Itoh for kind guidance, invaluable suggestions, and encouragement throughout his study.

His gratitude also goes to Associate Professor Hideki Sugimoto and Dr. Yuma Morimoto for their excellent suggestions and continuous encouragement throughout his study.

The author goes to special thanks to Professor Kazunari Yoshizawa and Associate Professor Yoshihito Shiota for their cooperation on DFT calculation in Chapter 2 and 3.

The author is also deeply grateful to Professor Shiro Hikichi and Associate Professor Jun Nakazawa for their cooperation on mesoporous silica (SBA-15) in Chapter 4.

Similarly, the author deeply appreciates Mr. Yuta Ueda for his considerable cooperation on the experiments in Chapter 4.

The author thanks all techniques in Analytical Division, Graduate School of Engineering, Osaka University for NMR, Mass Spectroscopy, and Elemental Analysis.

Special thanks to all the members of Bio-Functional Chemistry (BFC) laboratory for their help, valuable suggestions, useful discussions, and friendship.

The author acknowledges financial support from Japan Society for the Promotion of Science (JSPS Research Fellowships for Young Scientists).

Finally, the author acknowledges continuous encouragement and support given by his friends and family, Naoko Fujimoto, Hiroko Fujimoto, and Daichi Fujimoto.

Osaka, Japan
January, 2022

Tomohiro Fujimoto 

Department of Material and Life Science
Division of Advanced Science and Biotechnology
Graduate School of Engineering
Osaka University